Measurement of the Angular Distribution of the Electron from $W \rightarrow e + \nu$ decay, in $p\bar{p}$ at $\sqrt{s} = 1.8$ TeV, as Function of P_T^W

MEMORIA presentada en la Facultad de Ciencias de la Universidad de Zaragoza para optar al Grado de Doctor en Ciencias Fisicas por el licenciado

Manuel I. Martin Ramos

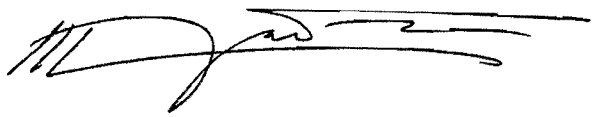

Fermi National Laboratory
Batavia, Illinois 60510, USA

7 de Octubre de 1996

Dr. Bruno GOBBI, Professor at the Department of Physics and Astronomy of Northwestern University in Evanston, Illinois 60201, U.S.A.

CERTIFICA

Que la presente Memoria " Measurement of the Angular Distribution of the Electron from $\mathbf{W \rightarrow e + \nu}$ decay, in $\mathbf{p\bar{p}}$ at $\mathbf{\sqrt{s} = 1.8}$ TeV, as Function of $\mathbf{P_T^W}$ " ha sido realizada en el grupo " DØ Collaboration" en el Laboratorio Nacional Fermilab bajo mi direccion, y que autorizo su presentacion para que sea defendida como Tesis Doctoral.

Firmado: Bruno GOBBI

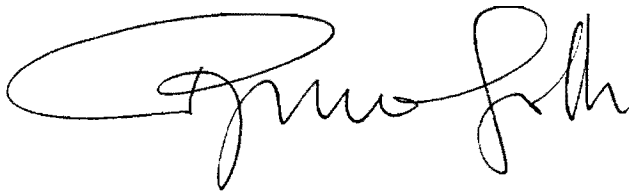

en Evanston, Illinois 60201, U.S.A.

Junio, 1996

To:

Emilia

Ann

Ester

ACKNOWLEDGEMENTS

It is customary to acknowledge the persons who and the institutions that, in one way or another, contributed to the work presented as a thesis. In this vein, my first thanks go to my parents, both teachers, who raised me to believe that knowledge is one's most important asset.

I want to give special thanks to a professor from my junior high school years: Sr. Marin. 'El Saco', as we called him, was able to transfer to me his love for Nature, Science and teaching. He was like a magnetic field that anchored the compass of my life.

I must thank Fermilab and its management for providing me with the unique opportunity to be a part of the DØ family and for allowing me to pursue my dream: to be counted among the members of the international club of physicists. In particular, I am indebted to Marvin Johnson, my supervisor, for his patience. Thanks also to all the people in DØ, a fantastic bunch who make me feel welcome. Many individuals from the DØ collaboration deserve special thanks, among them Darien Wood, who suggested the subject of this dissertation, Marcel Demarteau, Jaehoon Yu, Azriel Goldschmidt and Marc Paterno for the many discussions we had about my work and physics in general.

Many thanks to the people from Northwestern University (Evanston, Il.). Through four years they provided me with the means to carry out my work. Dave Buchholz and Heidi Schellman, both professors at NU, were kind enough to treat me more as an equal than a student. Thanks to my fellow students at NU who made me feel as young as they are, especially Yi-Cheng Liu (a PhD now), Tacy Joffe-Minor and Tracy Taylor-Thomas who helped more than they know.

Special thanks to Srinivasan Rajagopalan who showed me how to work with the Monte Carlo and to modify it to the requirements of this project. He not only gave me advice, but in many instances helped to solve software problems when I found myself entangled in them.

I must thank not only people from the present, but also to those people who one quarter of a century ago influenced me and, in one way or another, are responsible for what I am and do today. L. Garrido, my Quantum Mechanics professor, who encouraged me to go for a PhD and who showed his confidence in my abilities by putting me in charge of the best electronics laboratory of any university in Spain at the time. Thank you. Thanks also to Javier Alcoverro, Jose Maria Bañeres, Cary Borras, Nuria Bibiloni and Ester Casellas. Our many hours of study and discussions about physics, history, philosophy, religion, etc. molded my character and strengthened my love for knowledge. Ester and Jose Maria specially impacted my life in more ways that they will ever know.

Some additional words of thanks to my two advisors: Luis Joaquin Boya and Bruno Gobbi. I am lucky to have two excellent teachers to show me the way. Bruno has been my advisor and friend here at Fermilab. A professor

at Northwestern University, he has made it possible for me to be part of that excellent institution of higher learning. In doing so, he made it possible for me to rekindle a dream that was interrupted 25 years ago. A truly fantastic person whom I admire for his kindness, comprehension and impossible-to-match capacity for work. He showed me how to think as an experimentalist. Luis Joaquin was my advisor in 1967, and after 25 years of being out of touch did not hesitate to resume the relationship and be my advisor again. A teacher, a mentor and above all a friend, Luis Joaquin showed me that math is the beautiful garment in which nature shows itself to the physicist. Without his encouragement I am not sure I would have been able to finish. His lucid explanations of the most obscure areas of modern thought about the physical world created a bridge between what I had learned 25 years ago and what I need today.

Finally, I thank all who helped in my long periods of frustration, particularly my wife Ann. She deserves very special thanks, for not only did she tolerate my many 'cave' days, but she has contributed directly to this dissertation by being my editor.

Contents

List of Figures

List of Tables

Chapter 0

Introduction

.... Fables of the gods did not crush him, nor the lightning flash and the growling menace of the sky. Rather, they quickened his manhood, so that he, first of all men, longed to smash the constraining locks of nature's doors.

On the Nature of the Universe

Titus Lucretius Carus

In 1983, when the discovery of the W [1], [2] and Z [3], [4] bosons were reported, the physics community felt that one crucial aspect of the Standard Model was confirmed. Since then, the study of the production and decay of the W and Z bosons has been a fertile camp in which to test the validity of the Standard Model and theories beyond. In the late eighties, with the results of UA1 [8] and UA2 [9], the spin-1 nature of the W boson and its agreement with

the V-A theory were well established. Measuring the angular distribution of the charged lepton from $W^{\pm} \rightarrow e^{\pm} + \nu$ showed that it follows, within measurement errors, the predicted

$$\frac{dN}{d(\cos\theta)}\}_{W^{\pm}} \propto (1 \pm \cos\theta)^2 \ , \tag{0.1}$$

where θ is the angle between the emerging charge lepton and the antiproton direction. This prediction is for the case where the W production is described in the lowest order $[\mathcal{O}(\alpha'_f)]$ by the Drell-Yan process $q\bar{q} \rightarrow W$ when the W produced has very low Pt. Under these conditions the W emerges fully polarized in the axis of the of the $p\bar{p}$ and thus, equation 0.1 is valid.

When the boson created from a $p\bar{p}$ collision emerges with appreciable transverse momentum, the decay process is not fully described solely by the V-A coupling. Rather, application of perturbative QCD provides a fuller view of the interaction process. Using leading order $[\mathcal{O}(\alpha_f)]$, the angular distribution described above has the complex expression

$$\frac{dN}{d(\cos\theta)}\}_{W^{\pm}} \propto (1 + \cos\theta^2) + \frac{1}{2}A_0(1 - 3\cos\theta^2) + A_1 \sin 2\theta \cos\phi + \frac{1}{2}A_2 \sin\theta^2 \cos 2\phi + A_3 \sin\theta \cos\phi + A_4 \cos\theta \ . \tag{0.2}$$

Analytical calculations of the parameters involved in the above expression were presented by several people as early as 1981 [5],[6]. A complete

calculation of the next - to - leading - order for both W and Z bosons was published in 1992 [11]. The expressions for the angular distributions of the charged lepton from the W , or the l^- from the Z boson, leptonic decay are presented here:

$$\frac{d\sigma}{dP_T^2\ dy\ d(\cos\hat{\theta})} \propto 1 + \alpha_1 \cos\hat{\theta} + \alpha_2(\cos\hat{\theta})^2 \qquad (0.3)$$

and

$$\frac{d\sigma}{dP_T^2\ dy\ d\phi} \propto 1 + \beta_1 \cos\phi + \beta_2 \cos 2\phi \qquad (0.4)$$

where $\hat{\theta}$ and ϕ are the angles formed by the charged lepton with the direction of the antiproton and the x-axis in a preferential frame of reference. This special frame of reference, where the boson is at rest, is the Collins-Soper frame.

The predicted values for α_2 , as function of the transverse momentum of the W boson, are shown in Fig. 0.1 on page 6.

0.1 Goals

Scanning the extensive literature dealing with the properties of the W and Z bosons it is clear that, besides the measurements confirming the weak-

interactions theory, no specific work related to the angular distributions of the emerging particles from the leptonic decay of the boson has been done. In a hadron-hadron collision bosons are generated with a wide transverse momentum spectrum. High P_T^B can only be achieved if radiative parton effects are taken into account. This source of the P_T^B makes the study of these processes an excellent independent way to look at the QCD theories. The Tevatron at Fermilab, with 1.8 TeV at the $p\bar{p}$ center of mass, is an ideal source for these bosons with high transverse momentum.

Ideally, a precise measurement of α_1, α_2, β_1, β_2 is what we would like to achieve. Realistically, in this work, a measurement of α_2 for the case of the W boson is all that can be done. The reasons that the scope of the work must be limited to α_2 , other than the obvious ones of time and resources, are basically two:

- ◇ The lack of means to detect the charge of the lepton makes it impossible to measure α_1.
- ◇ Very reduced statistics make the study of the W decay difficult and the study of the Z decay not worthwhile. Keep in mind that the number of Zs generated in the Tevatron is one order of magnitude less than the Ws.

With these constraints in mind, the aims of the present work are:

- to obtain experimentally the values of α_2 , as function of the transverse momentum of the W, that appear in the expression 0.3 on page 3.

- to compare the values obtained with the theoretical predictions.

The value of α_2 can be extracted from the folded (where no distinction is made between $\hat{\theta}$ and $\pi - \hat{\theta}$) $\cos\hat{\theta}$ distribution. This permits the measurement to be independent of the charge of the W generated, as long as the possible asymmetry of $W^+ W^-$ is minor in relation to the effects under study.

Even though this is a very limited measurement, it is not without merit. The experimental value of α_2 could raise an early flag regarding the validity of the QCD parton model if the experimental measurements are in disagreement with the predicted values. This is most important, considering that similar measurements for the case $\gamma^* \rightarrow e^+ + e^-$ present an apparent disagreement with QCD. Conversely, it could provide a better understanding of the weak interactions and of the parton model, specifically at the low 'x' level. In any case, it will be the first time that the experimental determination of α_2 , as function of the transverse momentum of the W boson and for

P_T^W , is made.

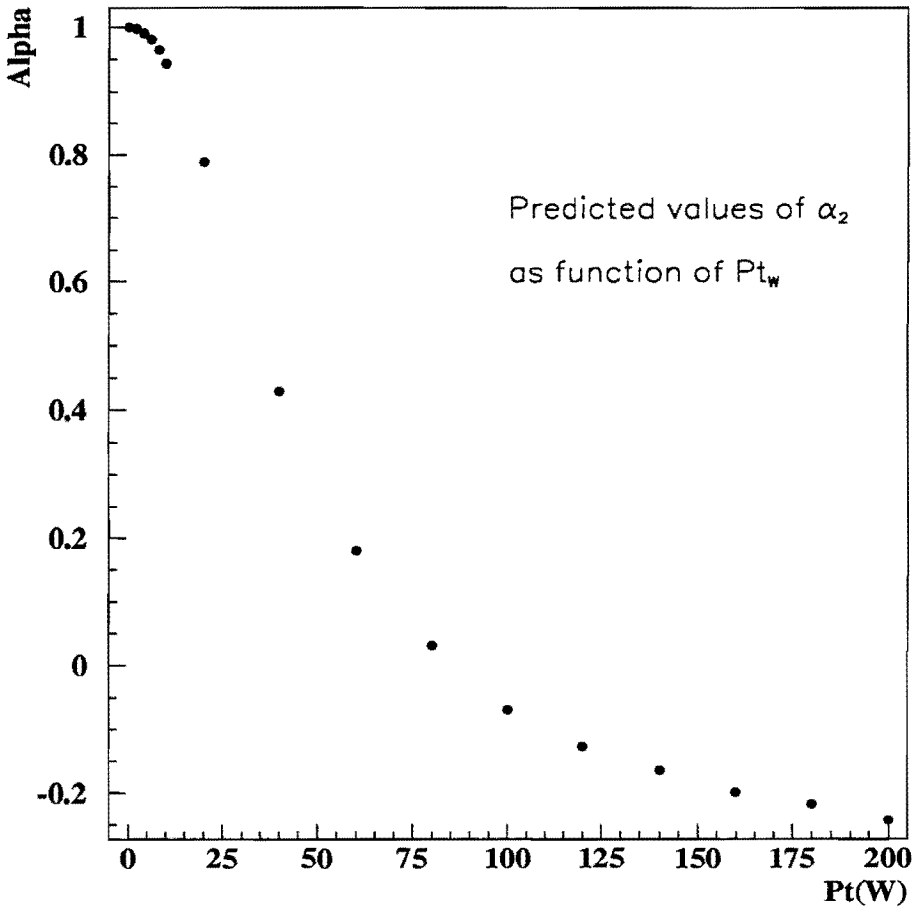

Figure 0.1: Predicted values of α_2

0.2 How to and why not

The measurements will be made using the transverse mass of the W instead of the $\cos\hat{\theta}$ distribution in the rest frame of the W. The justification for this choice will be presented in Chapter 6.

The reason the value of α_1 is not measured is simple: the DØ detector lacks magnetic field in its tracking system, making it impossible to distinguish between W^+ and W^- or to separate e^+ from e^-. The value of α_2, on the other hand, can be obtained from the folded distribution of $\frac{d\sigma}{dP_T^2\ dy\ d(\cos\hat{\theta})}$; thus, it is not necessary to know the sign of the particles involved. The set of parameters (β_i) could, in principle, be measured also. The reason not to do so here is a lack of statistics. The measurement of β_1 is of particular interest because it could give some insights into the gluon distribution functions. The value of β_2 is constrained by the vector-gluon theory to be

$$\beta_2 \approx \frac{1 - \alpha_2}{2(\alpha_2 - 3)} \tag{0.5}$$

even for large values of P_T^W and NLO calculations. It will be interesting to see, with more statistics than are presently available, if there are discrepancies between theory and experiment [7].

These measurements are of great importance for the understanding of the

world of particle physics.

0.3 Thesis organization

This thesis consists of four major divisions, each dealing with closely related themes: a)Physics Background, b) Description of the Hardware and General Software Tools, c) Description of the Analysis and Specific Tools, and d) Results and Conclusions. Each division is comprised of one or more chapters and each chapter is divided into sections and subsections. A more detailed description of the thesis' organization follows.

■ **Physics Background**

- This division has only one chapter, although to some extent, this introduction is part of it. The chapter opens with a brief justification for the matter chosen. It continues with a short history of modern physics, with emphasis on gauge theories. The last two sections are dedicated to the presentation of the production and decay of the gauge bosons in the Tevatron environment. Theoretical predictions of pertinent parameters are also shown.

■ **Hardware and General Software**

- The second chapter presents a description of the DØ detector. Its main sections correspond to the three partitions of the detector per se plus a short description of the trigger system. The bulk of the chapter is taken up by the Central Detector and the Calorimeter. These two parts of the global apparatus are the ones that play a major role in this analysis.

- Chapter three deals with general algorithms implemented in the General Software and used, one way or another, by all the members of the DØ collaboration. Again, only those which are pertinent to the work of this thesis are described in detail.

■ **Analysis and Specific Tools**

- This, the most extensive division, presents the analysis carried out in detail. It starts in chapter four recalling the theoretical predictions that this work addresses. The goal of this thesis is reiterated as the measurement of α_2 from the distribution folded distribution of $\cos\hat{\theta}^*$ in a particular frame of reference where the W is at rest. Noting that the numerical calculations done by the

theorists are performed in a special frame of reference, the Collins-Soper (CS) frame, a detailed study of such frame is made. As part of the understanding of the CS frame, a cautionary flag is raised: potential errors introduced in the analysis of some phenomena when the analysis is performed in the CS frame. The rest of the chapter is dedicated to understanding the importance of such errors.

- Chapter five is dedicated to the study of a different way of extracting the parameter α_2 ; a way that, fortunately, does not pay a heavy toll in unwanted sources of errors as the classical solution. The alternative method should avoid the need to boost the event to the CS. The rest of the chapter shows how the transverse mass distribution of the W meets the requirements and is sensitive to the value of α_2 . Errors and sensitivity studies of M_T^W fill the end of the chapter. This part of the chapter shows that it is imperative to have good control over the backgrounds and their sources.

- Aware that the problem is quite delicate, a search for the appropriate analytical tool was done. The sixth chapter describes the tool of choice and the rules to follow in its usage. In the same

chapter, a first set of constraints (cuts) to be imposed on the data is defined.

- The cuts defined in the previous chapter are now used to do an exhaustive study of the types of backgrounds encountered. Chapter 7 starts with the identification of the backgrounds, followed by the calculation of their relative influence in the analysis. The amount of distortion in the signal that a particular background creates depends on two things: a) the percentage of background corrupting the signal, and b) the shape of the background. Both determinations are carried out in this part of the thesis.

■ Results and Conclusions

- Chapter eight shows the calculations performed to extract the value of α_2 and the results of these calculations.
- Finally, the last chapter (chapter 9) is dedicated to the interpretation of the results obtained as well as to suggestions for further work.

Over all, the unfolding of the information presented in this thesis is aimed not only at providing a good understanding of the data and the way it is analyzed, but also at justifying the process followed.

Chapter 1

The Physics

On the other hand, the discovery of a final theory may have effects far beyond the borders of science. The minds of many people today are afflicted with various irrational misconceptions, ranging from relatively harmless superstitions like astrology to ideologies of the most vicious sort. The fact that the fundamental laws of nature remain obscure makes it that much easier for people to hope that some day their own favorite irrationalities will find a respectable place within the structure of science.

"Dreams of a final theory" S. Weinberg

No se contenta el ingenio con sola la verdad, como el juicio, sino que aspira a la hermosura. Poco fuera en la arquitectura asegurar firmeza, si no atendiera al ornato.

"Agudeza y Arte de Ingenio" Baltasar Gracian

1.1 Physics motivation

To properly validate the Standard Model, precise measurements of the free parameters introduced by the model are required. Furthermore, in order to have a complete picture of the phenomena involved in interactions, a good knowledge of the parton distribution within the composite particles is also needed. The production and decay of gauge bosons in hadron collisions is an excellent source of information. The determination of the masses of the $W^{\pm}$ and Z, as well as their production rates, have provided confirmation of some aspects of the theory, but more information is needed. Detailed study of the decay of the gauge bosons through the lepton channels will give us insight into lepton-hadron correlations and, in particular, will provide information about the parton structure functions including the gluons. The angular distribution of the bosons in the c.m. frame provides information about the polarization state of the bosons. Study of the angular distribution of the decay products of the bosons gives more detailed information about the parton distribution function than is otherwise possible through deep inelastic scattering experiments or through the measurement of production rates alone. At the lowest order ($O(\alpha_s^0)$ in perturbative QCD) the W production is described by the Drell-Yan process $q + \bar{q} \rightarrow W$. In this case the angular distribution of the charged lepton, resulting from the leptonic decay of the W, is given by the well known expression:

$$\frac{d\sigma}{d\cos\theta} \simeq valencequarks \otimes (1 + \cos\theta)^2 + seaquarks \otimes (1 + \cos\theta)^2 , \tag{1.1}$$

where θ is the angle between the resulting charged lepton (antilepton) and the proton (antiproton) in the rest frame of the W. This distribution can be parameterized as

$$\frac{d\sigma}{d\cos\theta} \simeq K\,(1 \pm \cos\theta)^2. \tag{1.2}$$

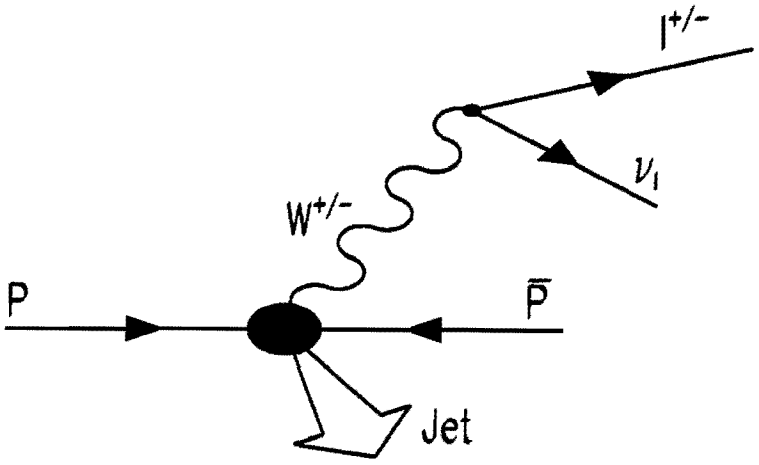

Figure 1.1: **Schematic diagram to show the production of W and its further decay through the lepton channel.**

The UA1 collaboration [10] measured this distribution and found it to be in good agreement with the expression 1.2 and with a mean value of $\cos\theta$

consistent with the standard model predictions ($< \cos\theta > = 0.43 \pm 0.07$ measured versus $< \cos\theta >= .5$ predicted) [10], [8]. But these measurements were independent of the transverse momentum of the W and only for small P_T^W.

No effort, to the best of my knowledge, has been made to extend the measurements to moderate values of P_T^W, or to correlate the $\cos\theta$ distributions with the P_T^W. These measurements are crucial because, even for moderate P_T^W, the expression 1.2 will not hold, as shown by E. Mirkes [11].

E. Mirkes calculates the angular distribution of the charge lepton for the inclusive process

$$p + \bar{p} \rightarrow W^{\pm} + X \rightarrow l^{\pm} + \nu_l + X \,, \tag{1.3}$$

as represented schematically in Figure 1.1, in a specific frame of reference showing that

$$\frac{d\sigma}{dP_T^2\ dy\ d\cos\theta} = K_\theta(1 + \alpha_1 \cos\theta + \alpha_2 \cos^2\theta) \tag{1.4}$$

and

$$\frac{d\sigma}{dP_T^2\ dy\ d\phi} = K_\phi(1 + \beta_1 \cos\phi + \beta_2 \cos 2\phi + \beta_3 \sin\phi + \beta_4 \sin 2\phi) \,, \tag{1.5}$$

where the coefficients $\{\alpha_1,\ \alpha_2\}$ and $\{\beta_1,\ \beta_2,\ \beta_3,\ \beta_4,\}$ carry the necessary information to calculate six out of nine helicity cross-sections σ^α for the $W^{\pm}$ boson, and y is the rapidity. Specifically, Mirkes predicts that α_2 is a monotonic decreasing function of P_T^W, and that $\beta_i \neq 0$ even for moderate

transverse W-momentum. It is important to measure these parameters in order to have a better understanding of the lepton-hadron correlation effects in the Standard Model. The aim of the present work is to measure one of these parameters, namely α_2 from expression 1.4, as precisely as possible.

1.2 Gauge Theories and the Standard Model

Since Maxwell's success in unifying the electrical and magnetic forces in a single theory, it has been the dream of all physicists to find a way to unify the forces of nature and to reduce the number of 'elementary' particles. As early as 1921 Herman Weyl [12] tried to do just that by looking for a common denominator between electromagnetism and gravitation. Although his efforts failed, his terminology 'gauge symmetries' survived. The idea that interactions are governed by symmetry principles became one of the most productive insights of modern physics. Noether's theorem tells us that there exists a conserved quantity associated with a continuous symmetry . The evolution of the gauge theories is intimately related to the discovery of 'new' particles and interactions. In the late 1920's and early 1930's Dirac, Heisenberg and Pauli [13] , among others, were successful in incorporating the concepts of special relativity and quantum mechanics with the framework of Maxwell and, in so doing, provided the first theory of quantum electrodynamics. This first attempt had, unfortunately, one major flaw: it converged only when calculated to the lowest order term in perturbation theory. In the late 1940's Feynman, Schwinger and Tomonaga showed how to get around this problem by introducing the concept of renormalization [14][15][16]. QED

(Quantum ElectroDynamics) became the most successful theory ever devised to describe the physical world. The Lagrangian for a charged particle of mass m in QED can be written as

$$\mathcal{L}_{QED} = \underbrace{i\bar{\psi}\gamma^{\mu}\partial_{\mu}\psi - m\bar{\psi}\psi}_{\mathcal{L}(FREE)} + \underbrace{e\bar{\psi}\gamma^{\mu}\mathcal{A}_{\mu}\psi}_{\mathcal{L}(INTERACTION)} - \underbrace{\frac{1}{4}\mathcal{F}_{\mu\lambda}\mathcal{F}^{\mu\lambda}}_{\mathcal{L}(PHOTON\ KINET.)} . \quad (1.6)$$

This Lagrangian is obtained by simply applying the '*natural*' condition that the *equations* describing the electromagnetic phenomena are independent of local changes in phase. The propagator (*photon*) must be massless as expected for a field that has infinite range. The gauge transformations used belong to the U(1) group.

The fantastic success achieved by the $\mathcal{L}_{QED}$ suggested the use of gauge invariances to formalize other symmetries. In 1954 Yang and Mills [17] applied the same concept to the isospin conservation in strong interactions. The isospin is described by an internal symmetry group SU(2). The infinitesimal local gauge transformation is represented by

$$\psi(x) \rightarrow [1 - ig\vec{\alpha}(x).\mathbf{T}]\psi(x) \quad (1.7)$$

and the new derivative is defined as

$$\mathcal{D}_{\mu} \equiv \mathbf{I}\partial_{\mu} + ig\mathbf{W}_{\mu}.\mathbf{T} , \quad (1.8)$$

where $\vec{\alpha}(x) \subset iso - space$, $\mathbf{T}$ is the isospin operator and $\mathbf{W}_{\mu}$ is the gauge field. Without details the Yang-Mills Lagrangian can be written as

$$\mathcal{L}_{YANG-MILLS} = \mathcal{L}(FREE) - \underbrace{g\bar{\psi}\gamma^{\mu}\mathbf{W}_{\mu}\psi}_{\mathcal{L}(INTERACTION)} - \underbrace{\frac{1}{4}\mathcal{F}_{\mu\lambda}\mathcal{F}^{\mu\lambda}}_{\mathcal{L}KINETICS} . \quad (1.9)$$

The SU(2) was unsatisfactory for various reasons. In particular, this model predicts that the propagators W^+, W^- and W^0 must be massless, which implies that the interactions mediated by them should have infinite range. This is in contradiction with the strong forces that are known to be of very short range and, thus, should be mediated by heavy particles. Even though the Yang-Mills model fails to explain the strong interactions, it makes predictions with important physical consequences. The required introduction of the strength tensor $\mathcal{F}_{\mu\lambda}$ imparts the model with the ability to produce three and four vertices of self-interacting propagators. At the same

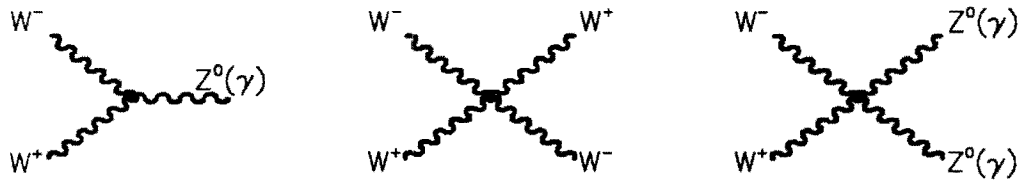

Figure 1.2: **Examples of vertices with 3 and 4 propagators.**

time great advances in technology and experimental techniques resulted in an explosion of 'new' particles and resonances. The spectrum of 'fundamental' particles and resonances became as crowded as the atomic line spectra and as difficult to classify as the excited atomic levels prior to the introduction of

quantum mechanics. The experiments also provide a picture of nature where two forces other than the gravitational and the electromagnetic are at play. These two forces act at the subatomic level. The *strong* force is responsible for holding the nucleus (and all the new spectrum of particles) together. The *weak* force governs the decay of some particles. The panoramic view seemed helpless until, in the mid 1960's, Gell-Mann [18] and Zweig [19] (working independently) advanced the idea that all the strongly interacting particles (hadrons) were made of elementary particles with fractional charge.

The search for a formalism that explains the known conserved quantities such as isospin, as well as the known or assumed elementary particles and forces, continued with redoubled interest during the same period. In 1961 Goldstone [20] showed that the Lagrangian for two scalar fields ψ_1 and ψ_2 and an effective potential defined as

$$V(\psi) = \frac{1}{2}\mu^2(\psi_1^2 + \psi_2^2) + \frac{1}{4}|\lambda|(\psi_1^2 + \psi_2^2)^2 \qquad (1.10)$$

spontaneously breaks the symmetry of SO(2) under a global phase invariance for $\mu^2 < 0$. This break in the symmetry gives life to two particles, one of them with mass!. Later Higgs [21] showed that when local invariant gauge theories are invoked, the unwanted massless Goldstone's bosons disappear and the gauge bosons, that act as propagators of the interactions, acquire mass. The Higgs mechanism finally provided a way to develop gauge models in which interactions can be mediated by massive particles as in the case of weak interactions.

In the late 1960's Glashow, Weinberg and Salam [22] took advantage of the Higgs mechanism to provide a unified model for weak and electromagnetic

Type	Symbol	Charge	Weak-isospin	Color	Mass (MeV)	Discovery
Leptons	e	-1	-1/2	—	.511	1897
(Spin 1/2)	ν_e	0	1/2	—	$< 15. \times 10^{-6}$	1953
	μ	-1	-1/2	—	105.7	1936
	ν_μ	0	1/2	—	$< .17$	1962
	τ	-1	-1/2	—	1777	1975
	ν_τ	0	1/2	—	< 35	1978
Quarks	d	-1/3	-1/2	R,G,B	5 ≈15	1964
(Spin 1/2)	u	2/3	1/2	R,G,B	2 ≈8	1964
	s	-1/3	-1/2	R,G,B	100 ≈300	1964
	c	2/3	1/2	R,G,B	1300 ≈1700	1974
	b	-1/3	-1/2	R,G,B	4700 ≈5300	1977
	t	2/3	1/2	R,G,B	≈ 175000	1995
Gauge	γ	0	—	—	0	1905
Bosons	W^+	1	—	—	80.22	1983
(Spin 1)	W^-	-1	—	—	80.22	1983
	Z	0	—	—	91.173	1983
	8 gluons	0	—	R,G,B	0	1977
Higg's (S=0)	H^0	0	—	—	? ?	! ? ! ?

Table 1.1: **Fundamental particles in the Minimal Standard Model.**

interactions. The model is based on the combination (product) of two group transformations: the $SU(2)_L$, which has as generator the *weak-isospin* , and the $U(1)_Y$ with the *weak-hypercharge* as generator. The Lagrangian for the theory can be written as

$$\mathcal{L}_{QED} = \mathcal{L}_{LEPTONS} + \mathcal{L}_{GAUGE} + \mathcal{L}_{SCALAR} + \mathcal{L}_{YUKAWA} \quad , \tag{1.11}$$

where the particles involved are the electron doublet

$$L_e = \begin{pmatrix} \nu_e \\ e \end{pmatrix}_L \tag{1.12}$$

and the quark doublets

$$L_q = \begin{pmatrix} u \\ d_\Theta \end{pmatrix}_L \quad , \tag{1.13}$$

with

$$d_\Phi = d\cos\Theta_C + s\sin\Theta_C \quad . \tag{1.14}$$

However, the theory needed a final refinement. Although internally self-consistent and powerful (it predicts the existence of weak neutral-current interactions), its problem was that neutral-current interactions will induce a *flavor* change. The confirmation of the existence of the neutral-current can be considered a plus for the theory, but the flavor-change is a minus, particularly when experimental limits have been placed on such interactions. This problem was solved in an elegant manner by Glashow, Iliopoulos and

Maiani [23] in their article published in 1970. Their solution was to introduce a fourth quark as a weak-isospin partner of the s_Θ, the *charmed* quark. It can be easily generalized to the case of several quark families and their counterpart lepton families. Today the accepted theory is to have three fermion families, twelve gauge bosons, four forces and, at least one Higgs' boson.

Type	Parameter	Experimental Value
Charge	e	1
Masses (MeV)		
Lepton	e, μ, τ	.511, 105.9, 1784
Quarks	d,u,s,c,b,t	10, 5, 200, 1500, 5000, 175000
Bosons	$W^{\pm}$,Z,H	80.22, 91.173, ???
Matrix[a]	$\alpha_1, \alpha_2, \alpha_3, \alpha_4$	
E scale[b]	Λ_{QCD}	
CP inv.[c]	Θ_{QCD}	

[a] The Cabbido-Kobayashi-Maskawa mixing matrix.

[b] Describes the way in which the strong force varies with energy scale.

[c] Relates to how well the strong force respects CP invariance.

Table 1.2: **Parameters required by the Standard Model.**

Once the weak and electromagnetic interactions are understood by the proper application of gauge invariances, it is logical to try to explain the strong interactions by an extension of the same process. As early as the mid 1960's Nambu suggested the development of a gauge theory based on color symmetry [24]; by the early 1970's Gell-Mann [25] had developed an almost complete picture of the strong interactions. In this theory the 'quarks' interacted by the mediation of 'gluons', gluons being the quanta of a gauge

field: the 'color' field. The group is the SU(3), and the gauge is non-Abelian. In the theory both quarks and gluons carry 'color' and gluons,which are massless, can interact with each other. Gell-Mann gave the name of Quantum ChromoDynamics (QCD) to this theory. The Lagrangian for QCD can be written as

$$\mathcal{L}_{QCD} = \bar{q}(i\gamma_\mu \mathcal{D}^\mu - m_q)q - \frac{1}{4}\mathcal{G}_a^{\mu\nu}(\mathcal{G}_a)_{\mu\nu} , \tag{1.15}$$

where the spinor for the color triplet is

$$q = \begin{pmatrix} q_R \\ q_G \\ q_B \end{pmatrix}_{color} , \tag{1.16}$$

the special covariant derivative is defined as

$$\mathcal{D}_\mu = \partial_\mu + ig\mathbf{B}_\mu , \tag{1.17}$$

and $\mathcal{G}^{\mu\nu}$ is the gluon field-strength tensor.

When it was first proposed QCD was received with skepticism because, as understood, it failed to explain why free quarks were not seen. Within one year t' Hooft and others gave a possible explanation by showing that non - Abelian gauges have the property of *asymptotic freedom* . QCD is a good theory for the strong interactions and its predictions are in good agreement with the experiments, but its prediction power is reduced by the complexity of the calculations. Nevertheless, QCD and QED combined form the best description of elementary particles and forces devised so far. This combination is the 'Standard Model'. It is important to mention that QCD

and QED strengthen each other; QCD provides the means for cancellation of the anomalies of QED (fermion loop diagrams that will render QED non-renormalizable).

The major strength of the Standard Model resides in its ability to provide an internally consistent theory, a theory that is in agreement with the experiments. In particular, all observations related to the behavior of the strong, weak and electromagnetic forces comply with the predictions of the theory. The description of these forces is done in terms of particle fields resulting from the imposition of local gauge invariants. The theory requires *only* the measurement of nineteen independent parameters, a list of which is shown in Table 1.2 with some of the assigned values from experimental data.

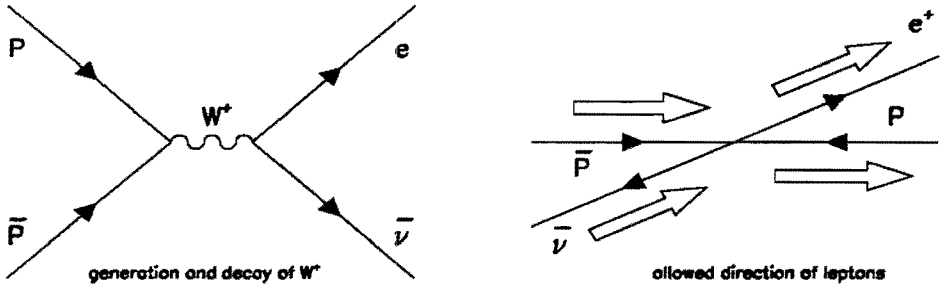

Figure 1.3: **Diagram for $q + \bar{q}$ $(u + \bar{d}) \rightarrow W^+ \rightarrow e^+ + \nu_e$ and allowed direction of the leptons and helicities.**

1.3 Hadronic $W \rightarrow l^{\pm} + \nu_l$ production

The generation of Ws with very low transverse momentum is described by the quark-antiquark annihilation process

$$q + \bar{q} \rightarrow W \ . \tag{1.18}$$

In this case the $W^{\pm}$ will emerge fully polarized with its spin aligned with the direction of the parent antiquark. This is a direct result of the V - A theory of charged current generation as well as the fact that the parent particles can only be left-handed fermions or right-handed antifermions. Furthermore, in the process represented by equ. 1.18, the only sources for transverse momentum for the W are the transverse momenta of the parent quarks. These transverse momenta can only be imparted by radiation effects. In this case, the angular distribution of the charged lepton can be expressed as

$$\frac{d\,\hat{\sigma}}{d\,\cos\hat{\theta}}(q\bar{q} \rightarrow l^{\pm} + \nu_l) \ \propto \ (1 \pm cos\hat{\theta})^2 \tag{1.19}$$

in the center of mass. This well known formula is presented in all text books. As implied above, this expression is a direct result of helicity conservation in collinear scattering. The UA1 collaboration at the CERN $p\bar{p}$ collider measured the $cos\hat{\theta}$ distribution, obtaining a good agreement with expression 1.19 and providing strong evidence that the W boson has helicity -1 as predicted by theory. In the cases where the emerging W has more than negligible transverse momentum, things are quite a bit more complex. We need to include in the calculations the effect of the radiated gluons and quarks which are responsible for the transverse momentum of the W. Considering only leading order processes, the following parton interactions

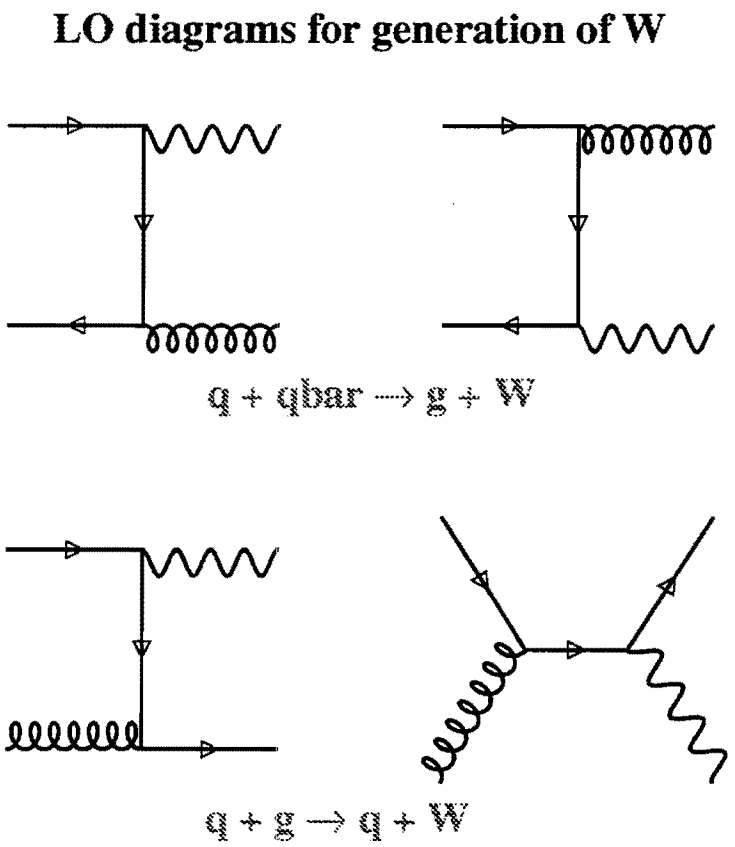

Figure 1.4: **Diagrams of leading order.**

$$\begin{aligned} q + \bar{q} &\rightarrow W + g\,, \\ q + g &\rightarrow W + q\,, \\ \bar{q} + g &\rightarrow W + \bar{q}\,, \end{aligned} \tag{1.20}$$

will impart transverse momentum to the generated W. The diagrams for these interactions are shown in figure 1.4.

There are many electroweak diagrams of NLO processes where the parton

interactions will result in a W plus jets. Figure 1.5 illustrates a small sample of interactions of the type

$$\begin{aligned} q + \bar{q} &\rightarrow W + g + g\,, \\ q + g &\rightarrow W + q + g\,, \\ \bar{q} + g &\rightarrow W + \bar{q} + g\,, \end{aligned} \tag{1.21}$$

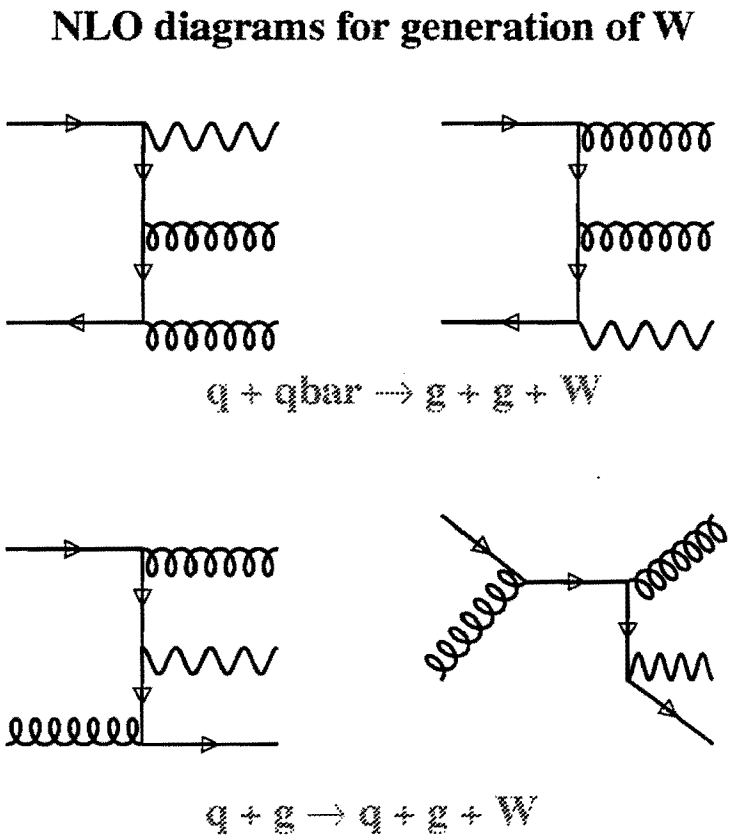

Figure 1.5: **Diagrams of near to leading order.**

1.4 Angular distribution of the leptons from bosons decay.

To calculate the distribution of the leptons resulting from the decay of a gauge boson $\mathcal{B}$ we need to calculate the complete production and decay distributions. The hadronic cross-section can be written as

$$\frac{d\,\hat{\sigma}^{ab}}{d\,q_T^2\;dy\;d\,\Omega} = \sum_{cd}\int\int dx_1 dx_2 \mathcal{F}_c^a(x_1)\mathcal{F}_d^b(x_2) \times \frac{s\;d\,\hat{\sigma}_{cd}}{dt\;du\;d\,\Omega}(x_1P_1,\; x_2P_2,\; \alpha_s(\mu^2)) \quad (1.22)$$

where $a,\ b \in q\ \bar{q}\ g$, $\mathcal{F}_c^a(x_i)$ is the probability density of parton a to have a momentum $x_i \times P$, $d\,\hat{\sigma}_{cd}$ is the parton cross-section for each of the expressions in 1.20, and s, t, u are the Mandelstam variables in the c.m. for the subprocess $(a, b \rightarrow l^{\pm}, \nu)$.

This expression can be rewritten in a form where the angular dependence, $d\,\Omega$, appears explicitly. To achieve this we write the correlations between hadrons and leptons as the tensorial product of the hadronic tensor $\mathcal{H}^{\mu\nu}$ and the leptonic tensor $\mathcal{L}_{\mu\nu}$. With the use of nine helicity cross-sections $\mathcal{H}_{ab}$ defined as

$$\mathcal{H}_{ab} = \varepsilon_a^* \mathcal{H}^{ab} \varepsilon_b \quad (1.23)$$

with

$$\begin{cases} (ab \in [+,\ -,\ ,0]) \\ \varepsilon_b = \frac{1}{\sqrt{1+|b|}}(b,\ -|b|i, 1-|b|,\ 0) \end{cases}$$

where ε_b, $b \in [+, -, ,0]$ represent the polarization vectors for the boson $\mathcal{B}$ in a given frame of reference. Thus the expression that gives the angular distribution of the lepton in a frame where the gauge boson is at rest has the form

$$\frac{d\sigma}{dq_T^2\ dy\ dcos\theta^*\ d\phi^*} = \frac{3}{16\pi}\sum_{\lambda=1}^{9} g_\lambda(\theta^*, \phi^*)\ \frac{d\sigma^\lambda}{dq_T^2\ dy}. \tag{1.24}$$

The product of the coefficients $g_\lambda(\theta^*, \phi^*)$ and the helicity cross-sections σ^λ carry all the information about the angular distributions of the emerging leptons in a given frame of reference. The rest frame of the B to be used is the Collins-Soper [26] frame. For a definition of the Collins-Soper frame, as well as a calculation of the transformation parameters see §4.

The following table shows what type of information is related to the different σ^λ.

From equation 1.24 we obtain the angular distributions for ϕ and $cos\theta^*$. By integrating respect ϕ and the rapidity y we have

$$\frac{d\sigma}{d(P_T^{\mathcal{B}})^2 d\cos\theta^*} = K_\theta(1 + \alpha_1(P_T^{\mathcal{B}})\cos\theta^* + \alpha_2(P_T^{\mathcal{B}})\cos\theta^{*2}) \tag{1.25}$$

and integrating over $\cos\theta^*$ and y

$$\begin{aligned}\frac{d\sigma}{d(P_T^{\mathcal{B}})^2 d\phi} &= K_\phi(1 + \beta_1(P_T^{\mathcal{B}})\cos\phi^* + \beta_2(P_T^{\mathcal{B}})\cos 2\phi^* \\ &\quad + \beta_3(P_T^{\mathcal{B}})\sin\phi^* + \beta_4(P_T^{\mathcal{B}})\sin 2\phi^*),\end{aligned} \tag{1.26}$$

where the dependence of the coefficients α_i, β_i from the transverse momentum of the gauge boson $\mathcal{B}$ is shown explicitly. These coefficients are related to

Element n	Symbol σ^{λ}	Coefficient $g_{\lambda}(\theta^*, \phi^*)$	Parity function	Boson polarization	Polarization matrix
1	σ^{U+L}	$1+cos^2\theta^*$	conserving	Unpolarized	(0 0)+(+ +)+(- -)
2	σ^{L}	$1-3cos^2\theta^*$	conserving	Polarized	(0 0)
3	σ^{T}	$2sin^2\theta^* \cos 2\phi^*$	conserving	Polarized	(+ -)+(- +)
4	σ^{I}	$2\sqrt{2}\sin 2\theta^* \cos\phi^*$	conserving	Polarized	(+ 0)+(0 +)-(- 0)-(0 -)
5	σ^{P}	$2\cos\theta^*$	violating	Polarized	(+ +)-(- -)
6	σ^{A}	$4\sqrt{2}\sin\theta^*\cos\phi^*$	violating	Polarized	(+ 0)+(0 +)+(- 0)+(0 -)
7	σ^{7}	$2sin^2\theta^* \sin 2\phi^*$	violating	Polarized	-(+ -)+(- +)
8	σ^{8}	$2\sqrt{2}\sin 2\theta^* \sin\phi^*$	violating	Polarized	(0 +)-(+ 0)+(0 -)-(- 0)
9	σ^{9}	$4\sqrt{2}\sin\theta^*\sin\phi^*$	conserving	Polarized	(0 +)-(+ 0)-(0 -)+(- 0)

Table 1.3: **Information related to σ^{λ}**

(After E. Mirkes)

the standard angular coefficients [26] $A_i \in (0,..,7)$ defined as

$$A_i = k_i \times \frac{d\sigma^{i+2}}{d\sigma^1} \qquad i \in (0,\ 1,\ 2,\ 3,\ 4,\ 5,\ 6,\ 7)$$
$$k_i \in (2,\ 2\sqrt{2},\ 4,\ 4\sqrt{2},\ 2,\ 2,\ 2\sqrt{2},\ 4\sqrt{2}) \quad (1.27)$$

by the expressions

$$A_0 = \frac{2(1-\alpha_2)}{3+\alpha_2} \quad A_2 = 2\beta_2 \quad A_3 = \frac{16\beta_1}{3\pi}$$
$$A_4 = \frac{4\alpha_1}{3+\alpha_2} \quad A_5 = 2\beta_4 \quad A_7 = \frac{16\beta_1}{3\pi}\ . \quad (1.28)$$

The above expressions provide the means to obtain six of the eight angular coefficients by studying the angular distributions defined in 1.25 and 1.26.

Figures 1.6 on the following page and 1.7 on page 33 show how the parameters A_0 and α_i, β_i vary with the P_T of the boson. Although this

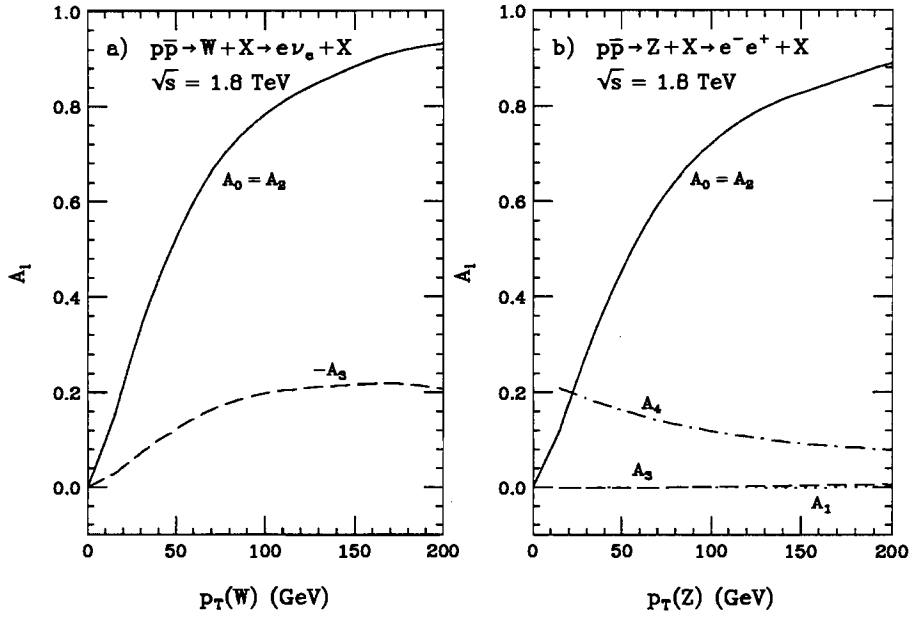

Figure 1

Figure 1.6: **Changes in A_i as function of P_T^B**

The figure on the left corresponds to the W-boson, the figure on the right to the Z-boson.

work is concerned only with the W-boson, the parameters for the Z-boson are also portrayed for completeness and comparison. Studying the graphs corresponding to the case of the W, it seems plausible to detect the changes in α_2 but not very likely to detect changes in the β_i values with the present statistics.

Both figures are presented here by permission of E. Mirkes.

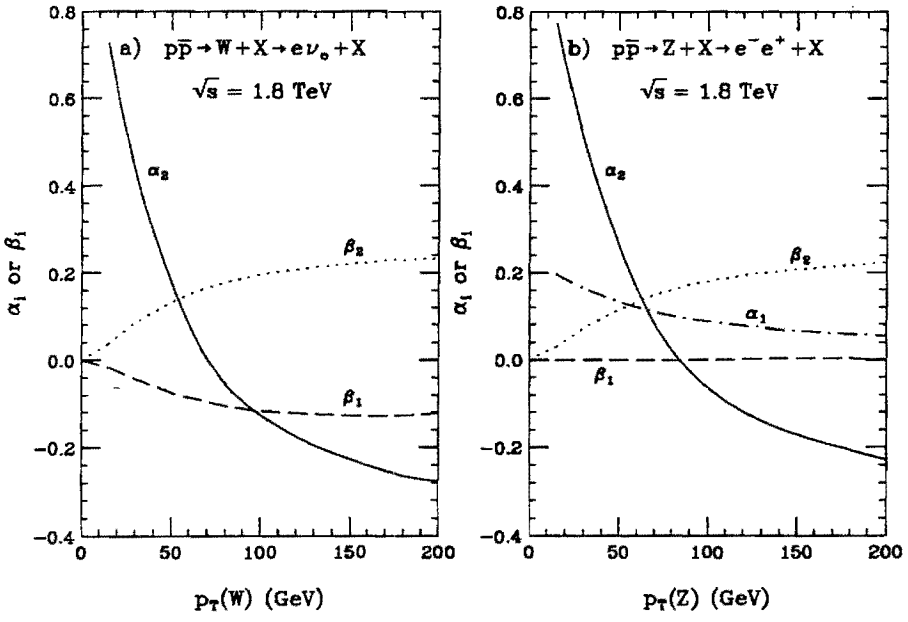

Figure 2

Figure 1.7: **Changes in α_i and β_i as function of P_T^B**

Chapter 2

The DØ Detector

Give me a fulcrum and I will move the Earth.

Archimedes

2.1 General

The DØ detector is one of the two collider detectors located at Fermilab. It was designed as a general purpose collider detector to study proton-antiproton collisions at $\sqrt{s} = 2$ TeV in the Tevatron Collider. The conceptual design report [28] was prepared in 1984. The design efforts culminated in the construction of a detector [27] capable of precision measurements of the W and Z bosons which provide good tests of the Standard Electroweak Model, particularly on states with high P_T [29],[30],[31],[32]. The detector was commissioned in 1991 and started taking data in 1992 . An isometric cut-away view of the detector is shown in Figure 2.1 where the nested shell structure of the system is clearly visible. The detector consists of several ma-

jor subsystems; i.e. the central detector, the calorimeter, the muon detector, associated electronics and support systems.

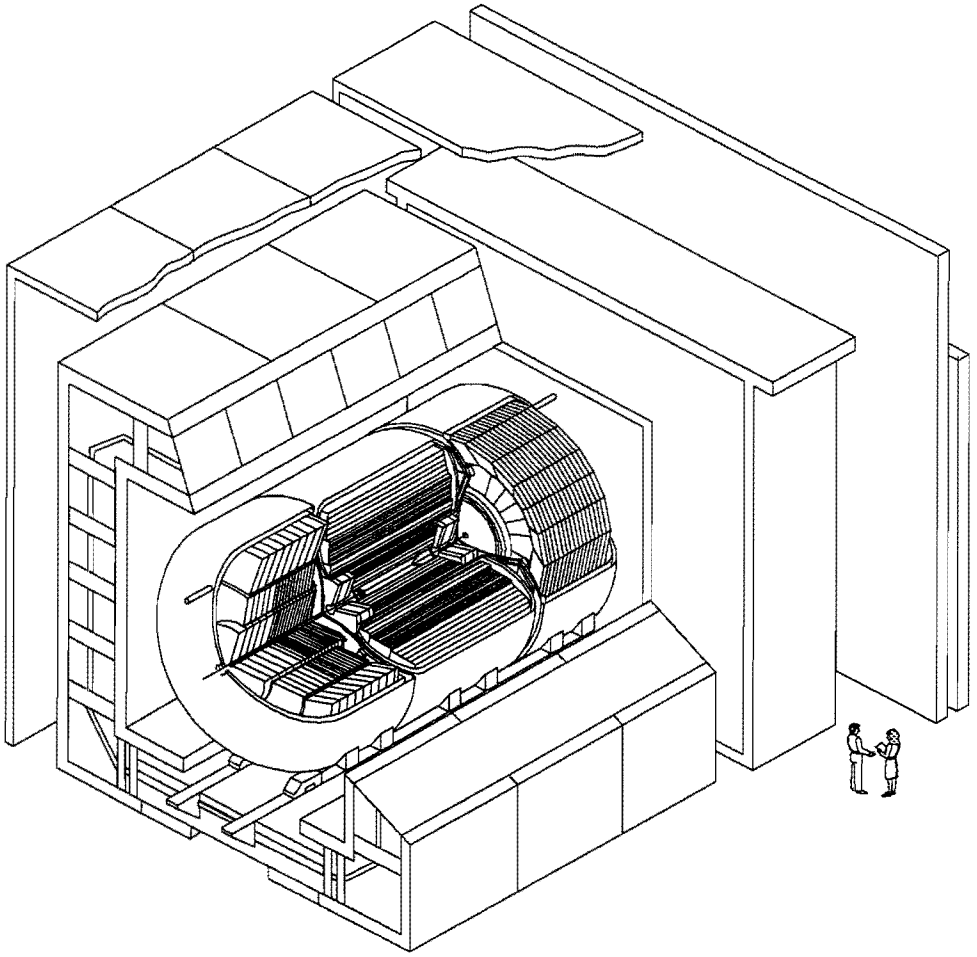

Figure 2.1: **Isometric cutaway view of the DØ detector.**

For the purpose of this report we will use the same conventions used throughout the DØ colaboration [27], mainly:

- A right-handed coordinated system where the z-axis is along the move-

ment of the proton and the y -axis is in the vertical direction going upward.

- The azimuthal angle is represented by Φ, the polar angle represented by Θ.
- The r -coordinate gives the distance to the beam axis.
- $\eta \equiv -\ln(\tan(\Theta/2))$ is the *pseudo-rapidity* and approximates the true rapidity for finite angles in the limit $(m/E) \rightarrow 0$.

2.2 The Central Detector

The Central Detector (CD), shown in Fig.2.2, is comprised of four detectors. They are: the Vertex Drift Chamber (VTX), the Transition Radiation Detector (TRD) , the Central Drift Chamber (CDC), and the two Forward Drift Chambers (FDC). The first three are cylindrical tubes confined inside the boundaries of the central region of the calorimeter. The central axis of these cylinders coincide with the axis of the beam. The FDCs, located at each end, are perpendicular to the beams and extend the coverage of the tracking system to $\Theta \approx 5^0$. The absence of magnetic field within the volume of the CD influenced considerably the design of the tracking detectors to provide good track resolution and good ionization energy measurements.

Although the total number of channels in the CD is relatively small (6080 channels with about 4200 wires), the effective detector resolution is excellent (on the order of $300\mu m$ in the x y plane and 1 mm in the z coordinate). These resolutions are very important for our study because identification of

charged particles relies on the identification of the energy deposited in the calorimeter (electrons), or the signals generated in the muon detector, and the matching of the calorimeter clusters, or muon chamber tracks, and the CD tracks. Furthermore, a good spatial resolution of the interaction vertex is necessary for proper momentum calculations.

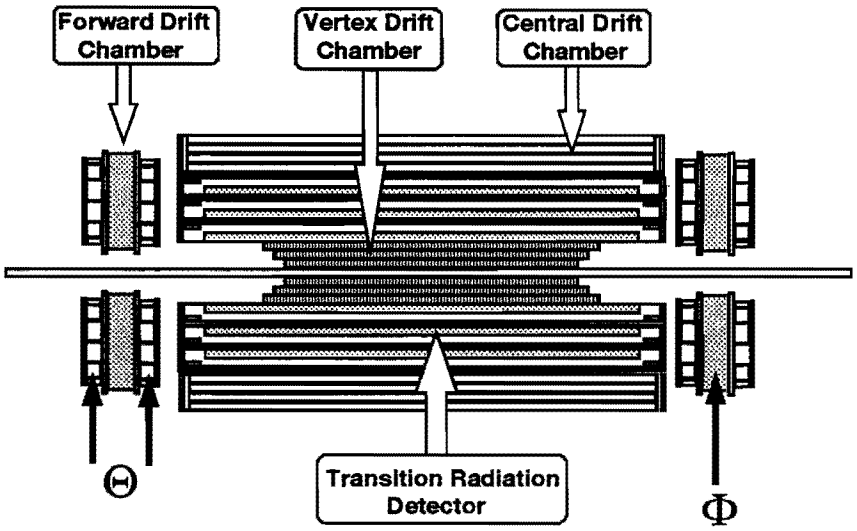

Figure 2.2: **Cross section of the tracking system in DØ.**

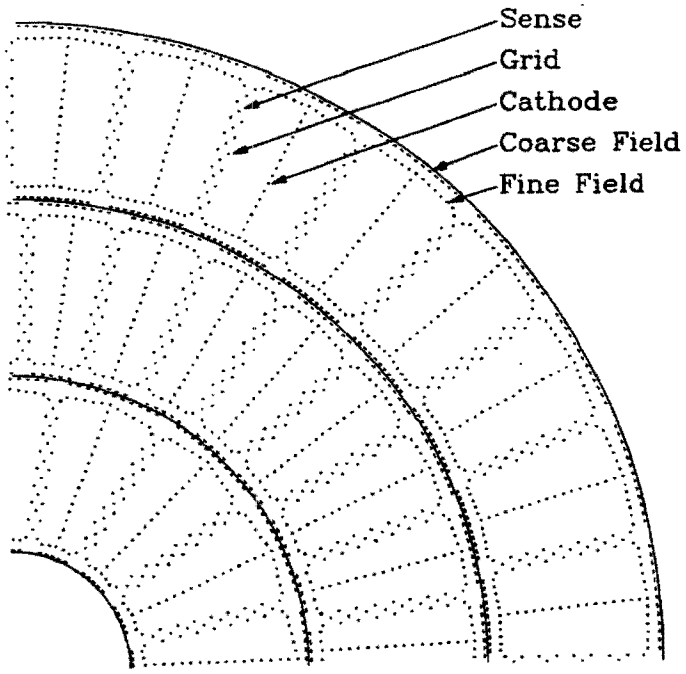

Figure 2.3: The VTX detector.

Cross section showing the position of the wires.

2.2.1 The Vertex Detector (VTX)

The closest detector to the interaction point is the VTX [33] . It is a cylindrical tube with an inner radius of 3.7 cm and an outer radius of 16.2 cm surrounding the berillium beam pipe. Constructed as three mechanically independent concentric layers, the VTX consists of 80cells, 16 cells in the inner layer and 32 cells in each of the remaining layers. Fig. 2.3 shows a cut of the VTX along a plane perpendicular to the z -axis. Looking at the picture, several features of the VTX are apparent. Each cell has a set of aluminum strips on the surfaces of the supporting carbon-fiber tubes and a set of cathode wires to shape the electrical field. The cathode wires and the grounded

grid-wires shape the electrostatic field with great precision. The sense wires, staggered $\pm$ 100 μm, provide measurements of r - ϕ coordinates and of the z coordinate. The last value is obtained by charge division; we read at both ends the charge deposited in the sense wires and use the expression

$$z = L * (k + 7) * \frac{A_0 - A^1}{A_0 + A^1} \quad , \tag{2.1}$$

where A_i are the signals at each end of the wire, L is the length of the wire and k is a charge division scale factor defined as

$$k = 1 + \frac{2 * \text{ Amplifier impedance}}{\text{Wire impedance}} \quad . \tag{2.2}$$

The chamber is operated at atmospheric pressure with a mixture of CO_2 and C_2H_4.

Table 2.1 gives some of the specification parameters of the VTX detector.

Dimensions		**Gas**	
Inner radius	R_{in} = 3.7 cm	Composition	CO_2 95%, C_2H_4 5%
Outer radius	R_{out} = 16.2 cm	Gain	40,000
Length	Inner layer L_{l1} = 97cm	**Characteristics**	
	Center layer L_{l2} = 107cm	Drift Field	$\approx$ 1kV/cm
	Outer layer L_{l3} = 117cm	Drift Velocity	$\approx$ 7.3μm/nsec
Sense Wires		Max. Drift	1.6 cm
Location	8 per cell; 640 total	Resolution	$r\Phi \approx 60\mu$m
Voltage	+ 2.5 kV		$z \approx$1.5 cm

Table 2.1: **Selected VTX parameters.**

2.2.2 The Transition Radiation Detector (TRD)

The lack of magnetic field in the central region of the DØ detector creates a problem insofar as it becomes difficult to separate real electrons from a background of fake electrons. To alleviate this problem the DØ experiment uses a TRD to discriminate between electrons and background. The capability of a TRD to distinguish between electrons (minimum ionizing particles) and hadrons (strongly interacting particles) is based on the transition radiation effect [34]. A highly relativistic ($\gamma = \frac{E}{m} \gtrapprox 1000$) charged particle will radiate photons in the few KeV regions when it crosses the boundary of two media of dissimilar dielectric constants. The radiated energy can be made proportional to γ . In our analysis it is important to be able to discriminate between electrons and background. The TRD [27] is located between the VTX and the CDC. It consists of three modules as shown in Fig. 2.2 , each module having a radiator and a γ detector chamber, as seen in Fig. 2.4 on the next page. The radiator units are made of 393 foils of propylene 18 μm thick separated by 150 μm gaps filled with nitrogen. This choice of radiator generates transition radiation photons with an energy spectrum that peaks at 8 KeV. The detector chamber is mounted just after the radiator and is a two stage time expansion radial drift chamber. The gas mixture used in the detector is Xe, CH_4 and C_2H_6 . To avoid contamination of the detector gas from the nitrogen used in the radiator a narrow channel (2 mm), defined by two 23 μm thick foils of mylar, is located between radiator and detector chambers. The outer mylar film has a metallization of aluminum that acts as a high voltage cathode in the detector part of the module. Dried CO_2 flows through this channel. Finally, each module has a helical set of cathode

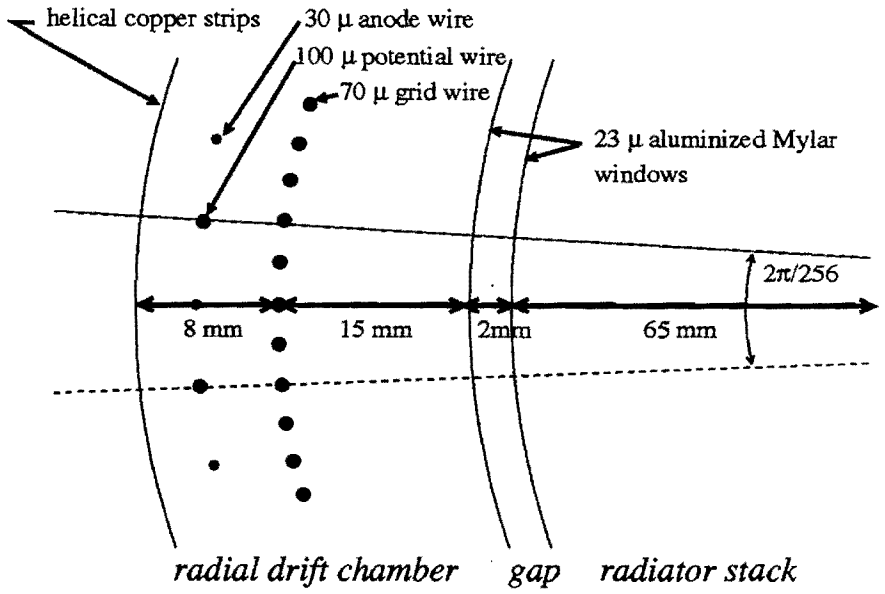

Figure 2.4: **Cut view of one chamber of the TRD.**

The relative positions of the elements in one of the three chambers is shown.

strips with pitch angles between 24^0 and 47^0 .

The TRD shows a $\frac{e}{\pi}$ rejection factor of $\approx$ 40 and retains 90% of the electrons.

2.2.3 The Central Drift Chamber (CDC)

The CDC provides tracking for charged particles in the region of $|\eta| \leq 1$. Mechanically the CDC is a cylindrical tube with an inner radii of 49.5 cm, an outer radii of 74.5 cm, and a length of 184 cm. An end-view of a sector of the CDC is represented in Fig. 2.5 on page 44 which shows the four concentric layers of chambers that comprise the detector. Each layer has 32 identical cells and each cell has seven sense wires and two delay lines. The sense wires

are read at one end while the delay lines are read at both ends.

Dimensions		**Gas**	
Inner radius	$R_{in} = 49.5$ cm	Composition	Ar 93 %, CO_2 3%, C_2H_4 4%
Outer radius	$R_{out} = 74.5$ cm	Gain	$G_{inner} = 20K.G_{outer} = 60K$
Length	All layers 180 cm	**Characteristics**	
# of layers	4	Drift Field	$\approx$ .62kV/cm
# of sectors	32	Drift Velocity	$\approx 34\mu$m/nsec
Wires		Max. Drift	7cm
Sense wires	7 per cell; 896 tot.	Resolution	$r\Phi \approx 180\mu$m
Delay lines	2 per cell; 256 tot.		$z \approx$3 mm

Table 2.2: **Selected CDC parameters.**

Information regarding Φ is provided by the sense wires by measuring the time of arrival of the signal to the readout system. This type of information carries an ambiguity; ie., it is not possible to distinguish between signals generated by particles passing to the 'right' or to the 'left' of the plane defined by the sense wires within a cell. To remove this ambiguity at the cell level, the sense wires are not located in the same Φ plane, but are staggered by $\pm 200\mu m$.

This arrangement, which breaks the geometrical symmetry, provides information regarding the side of the Φ plane through which the particle passed. The delay lines are embedded in the inner and outer walls of the cells and read at both ends. When a signal is created in the nearest sense line, an induced pulse is generated in the delay line. This signal will propagate to both ends of the delay line. Information relating to the position in z is retrieved by measuring the time differential between the arrival of the pulse

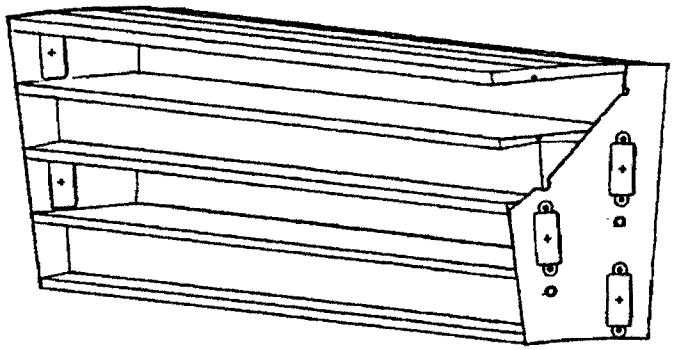

Figure 2.5: **Mechanical structure of the CDC .**

to one end of the delay line and the other [35]. Assuming a delay line with an electrical length L, and a propagation velocity V, a pulse generated at position 'Z' from the center of the delay line will have times of arrival to the left and right of T_L and T_R. From

$$\left.\begin{aligned} T_L &= \frac{\frac{L}{2}+Z}{V} \\ T_R &= \frac{\frac{L}{2}-Z}{V} \end{aligned}\right\} \tag{2.3}$$

the position Z referenced to the center of the delay line, is obtained as

$$Z = \frac{T_L - T_R}{2\,V} \quad . \tag{2.4}$$

Tracks generated by charge particles that pass through the CDC can be reconstructed with a resolution of $180\mu m$ in x, y and 3.5 mm in z.

The gas used in the CDC is a mixture of 93% Ar, 4% CH_4, 3% CO_2 at atmospheric pressure with traces (.05%) of water added. Some of the design parameters for the CDC are shown in Table 2.2.

2.2.4 The Forward Drift Chamber (FDC).

One advantage of the DØ detector is the great coverage at high η . The Forward Drift Chambers were designed to have good [36],[37] tracking of charged particles that emerge from the interaction point with Θ as low as 5^0. Located at either end of the Central Tracking Detector (comprised of the VTX, TRD and CDC), and just in front of the end calorimeters, each FDC consists of three modules as shown in Fig. 2.6 , essentially a Φ chamber sandwiched between two Θ chambers.

Parameters	**Φ modules**	**Θ modules**
Inner Radius	11 cm	11 cm
Outer Radius	61.3 cm	62 cm
Z-extent	113 - 127 cm	104.8 - 111.2 cm 128.8 - 135.2 cm
Sectors	36	4 quadrants of 6 layers
Sense Wires	8 per cell, 288 tot.	8 per cell, 384 tot.
Delay Lines	–	1 per cell, 48 tot.
Sense Wires Voltage	1.55 kV	1.66 kV
Gas	Ar 93 %, CO_2 3%, C_2H_4 4%	
Gas Gain	36,000	Inner G = 24 K Outer G = 53 K
Drift Field	1 kV/cm	1 kV/cm
Drift Velocity	37 μm/ns	40 μm/ns
Max. Drift Distance	5.0 cm	5.0 cm
Resolution (Drift)	$\approx$ 200μm	$\approx$ 300μm

Table 2.3: **Selected FDC Parameters.**

2.2.4.1 The Φ Module.

The Φ module is a single chamber divided into 36 sectors, each sector covering a span of 10^0 in Φ. Each sector has 16 sense wires strung radially and staggered along a plane of constant Φ. The staggering of the wires by $\pm 200 \mu m$ permits us to resolve ambiguities. The gross electrical field shaping required by the operation of the chamber is provided by 25 μm aluminum strips etched into the cell walls. The fine field shaping is provided by single guard wires strung between each pair of sense wires.

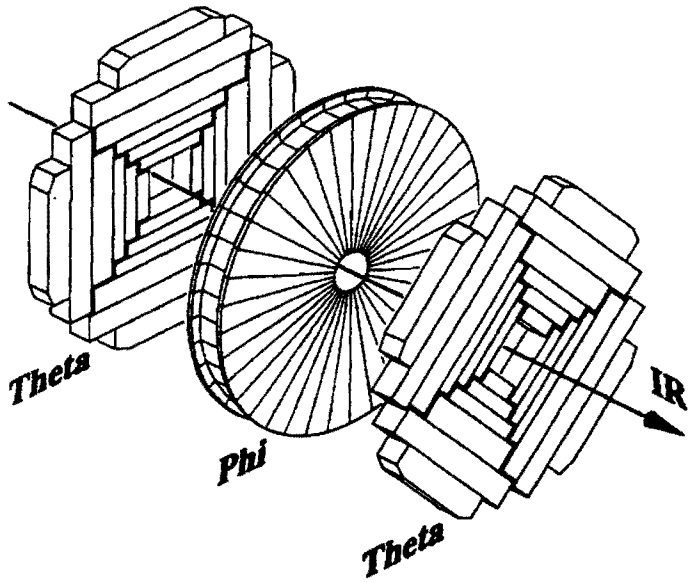

Figure 2.6: **Forward Drift Chamber at DØ.**

An exploded isometric view.

2.2.4.2 The Θ Modules.

There are four Θ modules, each built with four interlocking quadrants as shown in Fig. 2.6 . Each quadrant, in turn, consists of six rectangular cells,

each containing eight sense wires and a delay line. Both the sense wires as well as the delay lines are strung perpendicular to a Φ plane bisecting the cell and staggered by $\pm 200 \mu m$ along a plane parallel to the z-axis of the DØ detector. This construction permits us to measure the position of the tracks along the Φ plane bisecting the cell. The delay lines work on the same principle of the delay lines of the CDC.

The gross shaping of the electrostatic field within the cell is generated by Cu traces etched in both the top and bottom walls of the cell. The fine shaping of the field is obtained by two guard wires positioned between each pair of sense wires.

The FDC detector uses the same gas mixture as the CDC to which a trace amount of H_2O has been added. A partial list of the design parameters of the FDC is presented in Table 2.3

2.3 The Calorimeter System

The field of experimental high-energy physics concerns itself with the identification and characterization of particles. Because the DØ detector does not have a central magnetic field, and therefore, cannot make momentum measurements, the burden of making precise energy measurements falls solely on the calorimeter. This, coupled with the fact that particle identification (including muons) depends on calorimetry, makes the calorimeter the essential part of DØ . It is obvious that an excellent calorimeter is needed in order for DØ to be a superior detector.

2.3.1 High-energy Physics Calorimetry

Calorimetry, a term borrowed from experimental thermodynamics, is the science of precise energy measurements. In high-energy physics these measurements are accomplished by absorbing the particles in a massive medium and measuring the radiated energy of the generated 'shower'.

Ideally, the calorimeter is able to completely absorb the initial particle and to perfectly contain the ensuing shower. Any deficiency in either task will result in an underestimation of the energy of the incident particle. Other tasks required of the calorimeter in DØ are to localize in space the original particle and its trajectory and to differentiate between types of particles. These requirements, as well as size constraints and practical issues, strongly suggest the use of a *sampling calorimeter* versus a *total absorption calorimeter* . This choice also offers the possibility of obtaining as fine as possible segmentation into transverse and longitudinal cells.

In a sampling calorimeter the *cells* are typically constructed as sandwiches of dense (short radiation length) inert material and light (long radiation length) active material. As a particle passes through the dense material (the absorber) most of its energy is lost creating a *shower* that will liberate photons and other charged particles with only a *fraction* of the lost energy by the original particle in the absorber. The active part of the detector can measure this *fraction* of the original energy normally known as a *sampling fraction* . The sampling fraction in the DØ calorimeter is defined as

$$SF = t_{Ar}\frac{dE}{dx_{AR}}/(t_{Ar}\frac{dE}{dx_{AR}} + t_{G10}\frac{dE}{dx_{G10}} + t_{Absorber}\frac{dE}{dx_{Absorber}}) \quad , \tag{2.5}$$

where dE/dx is the mean energy lost by a minimum ionizing particle.

$t_{material}$ is the thickness of material that the particle passes through. The active material used in DØ is argon. Different types of absorbing materials are used and G10 is used in the electronic boards.

Two types of showers are detected, and their energy measured, in a calorimeter: electromagnetic showers and hadronic showers. The literature normally refers to *electromagnetic* showers as showers generated by electrons and photons. Electrons and photons with energies above a critical energy ϵ (dependent on the absorbing material), passing through matter, will create a cascade (shower) of photons, electrons and positrons by bremsstrahlung and pair production that will carry a large fraction of the initial energy of the particle. This process continues until the energy of the particles fall below the critical value ϵ. The physics of the electromagnetic showers is well understood and is described fully by quantum electrodynamics (QED). As long as the energy E of the particle is above ϵ the energy loss is governed by the expression [C. Fabjan Experi. tech in Hi e Ph]

$$(\Delta E) = -E(\frac{\Delta x}{X_0}) \tag{2.6}$$

where X_0 is the radiation length of the material and Δx is the length of the trajectory of the particle through the same material. When the energy of the particle falls below the critical energy ϵ the loss of energy is proportional to ϵ. The longitudinal development of the shower is (see 2.6) then defined by the radiation length of the absorber. The lateral development, on the other hand, is due to multiple scattering. The combination of these two effects

results in showers that are relatively 'narrow'.

Type of process	Characteristics	Affects E resolution by:
Hadron production	Multiplicity $\approx A^{0.1} \ln s$	$\frac{\pi^0}{\pi^\mp}$
	Elasticity $\approx \frac{1}{2}$	Binding E loss
Nuclear deexcitation	Evaporation E $\approx 10\%$	Binding E loss
	Binding E $\approx 10\%$	Slow n not detected
	Fast neutrons $\approx 40\%$	Poor sampling
	Fast protons $\approx 40\%$	Poor sampling
Other decays ($\pi's, \mu$, etc.)	.....	Losses

Table 2.4: **Phenomena in Hadronic Showers .**

W.W.M. Allison and P.R.S. Wright [34]

Hadronic showers are generated by the interaction of hadrons with the materials in the calorimeter. The processes by which a hadronic shower is created and propagated are far more complex than the relatively simple processes governing an electromagnetic shower. We do not have a good analytical model for hadronic showers even though the elementary processes involved have been studied in detail. Table 2.4 presents the most important phenomena involved in a hadronic shower; the table is based on data presented by Fabjan and Amaldi. Because the hadrons are heavy particles the energy lost by bremsstrahlung is minimal and the primary cause of energy loss is due to inelastic collisions with the nuclei of the absorber. About half of the energy is lost in this way. A good fraction of the energy is used in breaking-up or exiting the nucleus of the constituents of the absorber and only a fraction of this energy will be detected.

A very important role of the calorimeter is its ability to distinguish be-

tween electrons, photons and hadrons. Calorimeters rely on the fact that the cross section for inelastic nuclear collisions is smaller than the cross section for electromagnetic showers; as a result, hadronic showers will be larger (both longitudinally and laterally) than electromagnetic showers. This difference in shower size is used to identify the type of particle as it passes through the calorimeter.

A problem common to calorimeters is the fact that hadronic particles, and particularly jets [34], deposit a large fraction of their energy in electromagnetic showers and that this fraction has large fluctuations. Furthermore, an electromagnetic and a hadronic particle of the same energy will generate different signals in the calorimeter. This is mainly a result of the fact that a large fraction of the hadronic energy is expended in breaking up the atomic nuclei: approximately 40% of the available hadronic energy is unaccounted for. The response of a calorimeter improves if the measured energies are scaled so that the response to an electron and a hadron of equal energy is the same. The relationship between electromagnetic and hadronic energies is given by

$$\frac{e}{h} = \frac{r_{electromagnetic}}{\alpha + \beta\, r_{neutrons}} \tag{2.7}$$

where $r_{electromagnetic}$ and $r_{neutrons}$ are the responses of the calorimeter to electrons and neutrons respectively, and α and β are constants to be determined.

Several other factors can affect the over all response of a calorimeter. In general the energy resolution of a calorimeter is parameterized as

$$\frac{\sigma_E}{E} = \sqrt{C^2 + (\frac{S}{\sqrt{E}})^2 + (\frac{N}{E})^2} \ . \tag{2.8}$$

C, S, and N are constants related to calibration errors, sampling fluctuations, and noise respectively. The values of these constants in DØ are presented in Table 2.5 .

TYPE	C	S $\sqrt{GeV}$	N GeV
Electromagnetic			
Central	0.003 ± 0.004	0.162 ± 0.011	0.140
Ends	0.003 ± 0.002	0.157 ± 0.005	0.29 ± 0.03
Hadronic			
Central			
Ends			
for electrons	0.010 ± 0.004	0.233 ± 0.010	1.22
for pions	0.047 ± 0.005	0.439 ± 0.042	1.28

Table 2.5: **Resolution Parameters for the DØ Calorimeter.**

The DØ collaboration chose liquid argon as the active medium for the simplicity of calibration, because there is no radiation degradation, the flexibility provided for segmentation (see Fig. 2.7 on the next page), and the unity gain provided by the medium. The complications introduced by the need for relatively massive containment structures and cryogenic systems are a low price to pay for the above mentioned advantages.

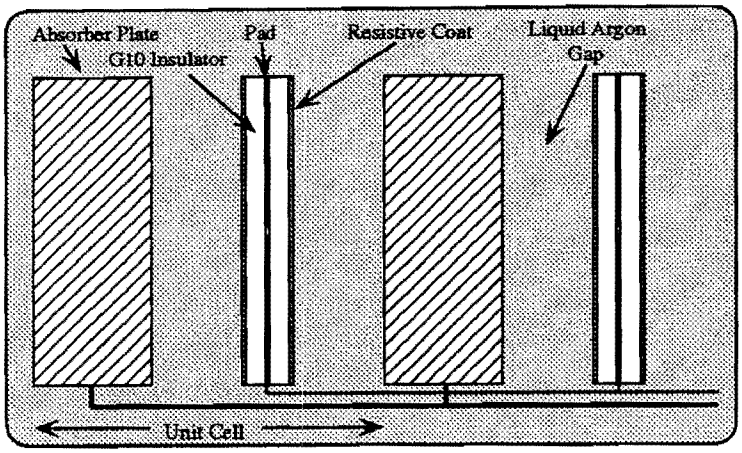

Figure 2.7: **Representation of 2 calorimeter cells.**

Conceptual cutoff view of 2 cells in the DØ Calorimeter.

2.3.2 DØ Calorimeter Implementation.

The dimensional constraints and the need to have access to the central detectors forced a segmentation of the calorimeter in three independent structures as shown in Fig. 2.8. The central calorimeter (CC) covers the region up to $|\eta| \approx 1$ while the pair of end calorimeters (ECN and ECS) extend the total coverage to $|\eta| \approx 4$. The choice of a boundary between the CC and the end calorimeters roughly perpendicular to the z-axis gives minimum degradation in the measurement of the transverse energy ($\not\!\!E_T$). The need for maximum shower containment and good particle identification directed the design efforts. As a result of all these constrains and requirements, all three sections of the calorimeter was built using three types of modules:

- EM Electromagnetic modules using thin (3 mm in the CC and 4 mm in the ECs) pure depleted uranium plates as absorber.

- **FH** Fine Hadronic modules using thick (6 mm) plates of an alloy of 98.3% uranium and 1.7% niobium.

- **CH** Coarse Hadronic modules using thick (46.5 mm) plates. Copper in the CC and stainless steel in the ECs.

A representation of a typical module is in Fig. 2.7 on the preceding page. The signal boards consist of two G-10 sheets. Both sheets have a surface coated with a carbon loaded epoxy creating an area with a resistivity of $\approx 40 M\Omega/\Box$. One sheet has a pattern milled into the copper of one surface. The other sheet has one naked surface. The electrical field is obtained by grounding the absorber plate and connecting the resistive surface of the signal boards to a high voltage of +2.0 kV. Finally, the modules are arranged in a *pseudo-projective* pattern defined here as a distribution of cells in space such that the *center* of cells pertaining to the same *tower* are located along rays projecting from the center of the detector, and where the cell walls are parallel or perpendicular to the absorber plates [38].

2.3.2.1 Central Calorimeter (CC).

The CC consists of three cylindrical shells with their central axis coinciding with the axis of the beam. The inner shell has 32 Electromagnetic modules, the middle contains 16 Fine Hadronic modules, and the outer shell has 16 Coarse Hadronic modules. The segmentation for the CC is $\Delta\eta \times \Delta\Phi = 0.1 \times 0.1$ except for the third layer of the electromagnetic modules where the segmentation is $\Delta\eta \times \Delta\Phi = 0.05 \times 0.05$. The Table 2.6 provides more specific information about the CC .

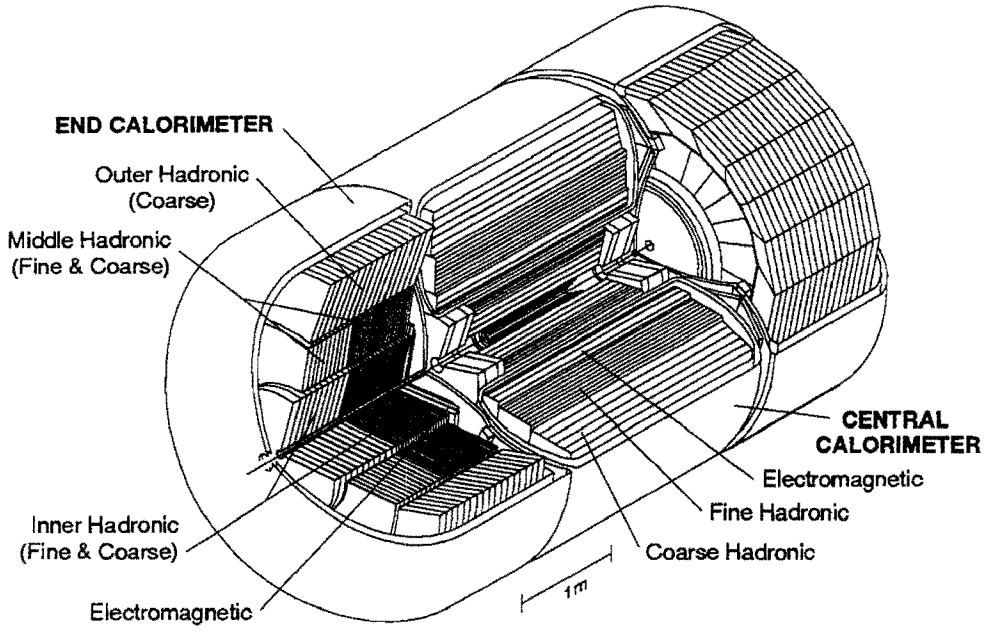

Figure 2.8: **Calorimeter and Tracking systems.**

An isometric cutaway view.

2.3.2.2 End Calorimeters (EC).

Two calorimeters, one at each end of the CC, are used to extend the coverage from $|\eta| \approx 1.1$ to $|\eta| \approx 4.5$. This provides DØ calorimetry with one of the best η coverages to date. The EC are made of four modules as shown in Fig. 2.8 : the Electromagnetic module (EM), the inner hadronic module (IH), the middle hadronic module (MH), and the outer hadronic module (OH). The EM has the aspect of a pancake; it consists of four readout sections with an inner radius of 5.7 cm and outer radii going from 84 cm to 104 cm. This

Parameters	Module		
	EM	FH	CH
Number of modules	32	16	16
Absorber	U	98% U 2% Nb	Cu
Absorber Thickness (mm)	3	6	46.5
Total radiation lengths (X_0)	20.5	96.0	32.9
Total interaction lengths (λ)	0.76	3.2	3.2
Sampling fraction (%)	11.79	6.79	1.45
Number of readout layers	4	3	1
Cells per layer	2,2,7,10	21,16,13	9
Number of channels	10,368	3456	768

Table 2.6: **Central Calorimeter Parameters.**

module has a total of 7,488 channels.

The IH modules are cylindrical with an inner radius of 3.92 cm and an outer radius of 86.4 cm. All hadronic modules have four fine hadronic sections and a single coarse hadronic section.

2.3.2.3 Massless gaps and the ICD

Between the CC and the EC's there are gaps covering the region $0.8 \leq |\eta| \geq 1.4$. This region contains primary uninstrumented material whose profile, along a particle path, changes greatly. The energy lost in this region, by a particle going through it, is not detected. To obtain a correction for the losses in the region two types of detectors are instrumented: the intercryostat detector (ICD) and the massless gap detector (MGD). One ICD is mounted on the front surface of each EC and the MGD are installed inside the CC

Parameters	Module					
	EM	IFH	ICH	MFH	MCH	OH
Number of modules/cryostat	1	1	1	16	16	16
Absorber	U	UN^a	SS^b	UN	SS	SS
Absorber Thickness (mm)	4	6	6	6	46.5	46.5
Total radiation lengths (X_0)	20.5	121.8	32.8	115.5	37.9	65.1
Total interaction lengths (λ)	0.95	4.9	3.6	4.0	4.1	7.0
Sampling fraction (%)	11.79	5.7	1.5	6.7	1.6	1.6
Number of readout layers	4	4	1	4	1	3
Cells per layer	2,2,6,8	16	14	15	12	8
Number of channels	7488	4288	928	1472	384 + 64	896 + 64

Table 2.7: **End Calorimeter Parameters.**

and EC's.

Parameters	CC MGD	EC MGD	ICD
Number of modules/cryostat	16	16	64
Number of channels	320	384	384

Table 2.8: **Parameters for the Massless Gap and Inter Cryostat Detectors.**

The ICD is an array of 384 $0.1\Delta\eta \times 0.1\Delta\phi$ scintillator tiles so located as to match the pseudo projective structure of the calorimeter cells. The generated light is measured by phototubes. The response, across the surface of a tile, is uniform within 10%. The response to a minimum ionizing particle is on the order of 20 photo-electrons.

The MGD modules are single calorimeter cells consisting only of two

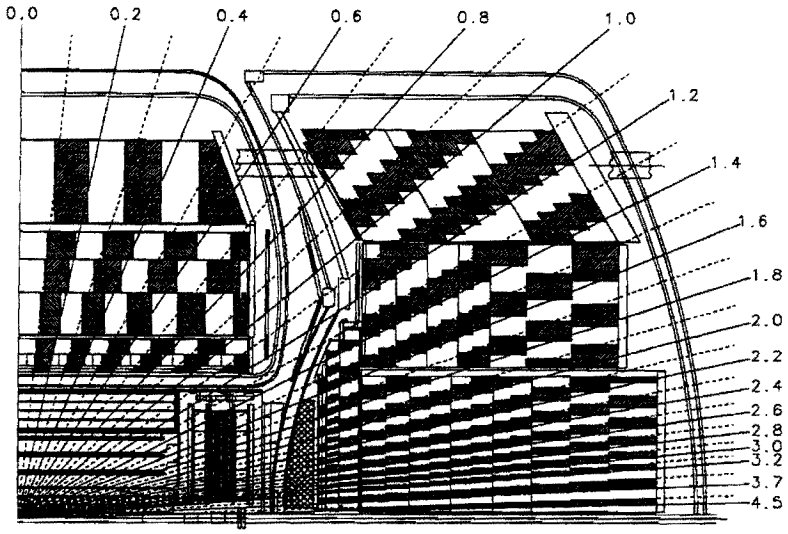

Figure 2.9: **Partial cut view of the DØ detector.**

signal boards surrounded by liquid argon without absorber plates. The segmentation of the MGD is the same as the rest of the calorimeter.

These features of the calorimeter can be seen in Fig. 2.9. As mentioned, the coverage of the DØ calorimeter is excellent. The Central Tracking and the FDC are also shown in the picture.

2.4 The muon system

Muons are ionizing particles with relative high mass ($\approx 106 MeV$) and with a mean life of $\approx 2.2 \mu s$ that interact weakly with matter. Their mean life is large enough that they appear as stable particles to the detector. In addition, their high mass decreases the chances for them to lose any appreciable fraction of energy by bremsstrahlung. As a result, the chances of detection by the

calorimeter are minimal and the measurement of their energy needs to be made by measuring their momentum.

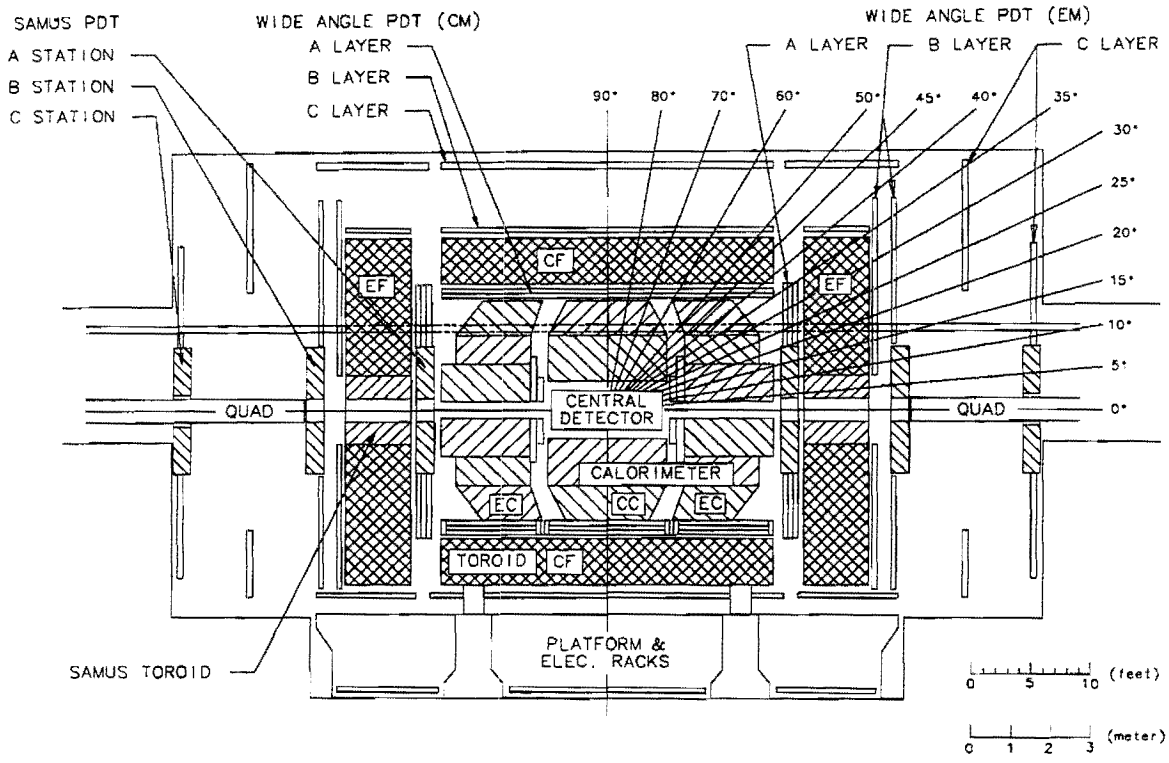

Figure 2.10: **Cut view of the DØ detector showing the Muon System.**

The muon detector system in DØ has five independent solid-iron toroidal magnets surrounded by proportional drift chambers and is partitioned in a wide angle system (WAMUS) and a small angle system (SAMUS). See Fig. 2.10 for a side view of the muon system and its relation to the rest of the DØ detector. The geometry of the magnets and their position in space forces the bending of the trajectories of the muons in a $r - z$ plane. The magnetic field has a field strength of approximately 2 T, but because of the shape of

the toroids, it varies across their square cross-section; this requires a careful mapping of the field to be able to make proper momentum measurements. The trajectory of the muon is defined by information before and after the muon passes through the magnetic field. Before entering the toroid, the trajectory is defined by the interaction point (vertex), tracking and the first layer of the muon chamber. After the toroid, two muon chambers, separated by 1 to 3 meters, provide information of the trajectory after the muon has been deflected by the magnetic field. The direction before and after the bending and the strength of the field, in absence of multiple scattering, are all the parameters needed to calculate the momentum of the muon. The multiple scattering suffered by the muon as it passes through the calorimeter and the toroids limits the relative momentum resolution to $\geq 20\%$.

Figure 2.11 on the next page shows the quantity of material, in interaction length, that the muon encounters, whereas table 2.9 gives a synthesis of the design parameters of the muon system.

Parameters	
Magnetic field strength	2 T
Precision in bend plane	.9 mm
Precision in non-bend plane	$\approx$ 1 cm
$\delta p/p$ [a]	18%

[a] *Multiple scattering limit assuming perfect% chamber resolution.*

Table 2.9: **Design parameters of the DØ muon system.**

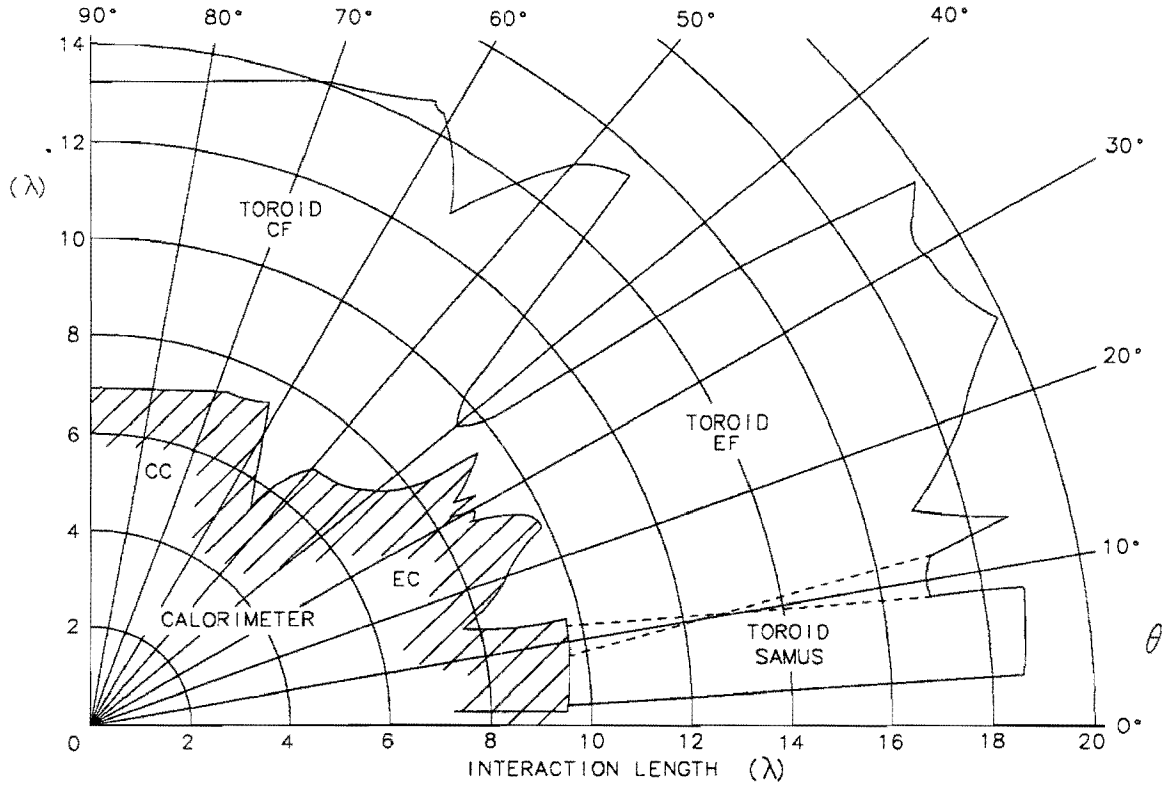

Figure 2.11: Material in the DØ detector.

Material encounter by a muon measured in interaction lengths.

2.5 The trigger system

The DØ detector sees a $p\bar{p}$ crossing approximately every $3.56\mu s$ given a crossing rate of $\approx 281KHz$. At the typical luminosity during run 1A this translates into an event rate of $\approx 350KHz$ [39]. Of these events only a relatively small number correspond to events of interest to the DØ collaboration. The way to discharge events of no interest while keeping those that pass some criteria is to use a series of filters or "triggers".

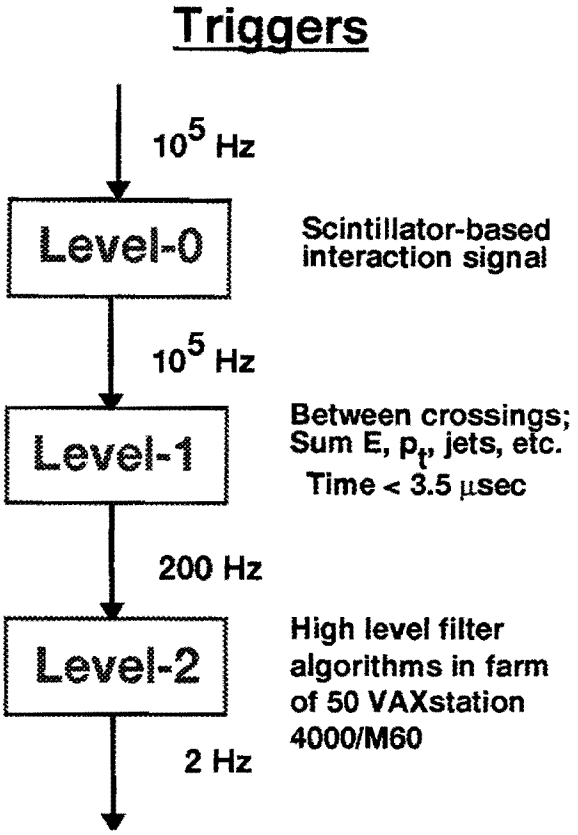

Figure 2.12: **Hardware Triggers' Chart.**

The effect of the triggers is to drastically decrease the total number of events that are "passed" to the next level in the data aquisition system with very few losses of interesting events. The use of triggers reduces the event rate to $\approx 2\ Hz$. The trigger system consists of four filters or trigger levels. The first three are hardware filters whose outputs are presented to an $AND\backslash OR$ logical network: the "*Trigger Framework*". The final filter, named "*Level 2*", is implemented in software. A schematic representation of the different

triggers and their relationships is presented in Fig. 2.13 on the following page.

2.5.1 Level 0

The first trigger detects the presence of hard interactions. This is accomplished by two sets of scintillator tiles mounted on the surface of each EC and located very near to the beam pipe. When "simultaneous" activity is detected by the two sets Level 0 "triggers" generating a signal indicating that a collision has taken place. Simultaneous activity here implies that signals generated by the two sets of scintillator tiles occurred within a narrow time window. The time separation between the arrival of the signals generated in one set of scintillators versus the other allows for a fast estimation of the position in z of the interaction point. Within $800ns$ of the collision the position of the interaction point is known with resolution of $15cm$. A much better resolution will be achieved during the reconstruction process of the event, at which time the interaction point will be calculated with a resolution of $3.5cm$.

2.5.2 Level 1

The Level 1 trigger consists of two distinct hardware filters. The filter related to the calorimeter provides a rough estimation of the energy deposited in the calorimeter fragmented into "trigger towers" formed by the cells in a region of $\Delta\eta \times \Delta\phi = 0.2 \times 0.2$ and up to four levels of energy. This information is available $800ns$ after an interaction occurs. The filter related to the muon detector provides only information saying that a muon has been detected and "coarse" indication of where the muon has been located.

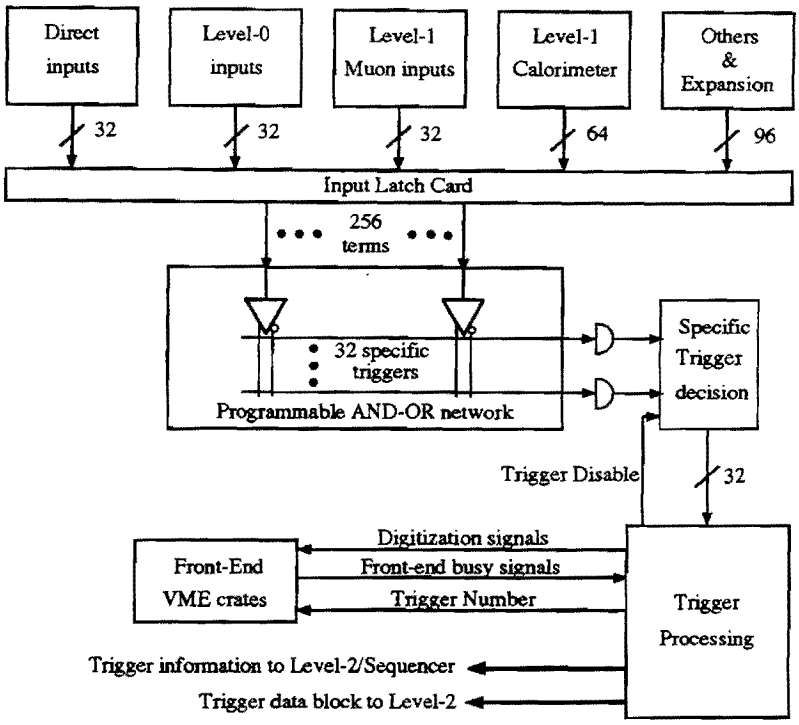

Figure 2.13: **The Trigger Framework.**

2.5.3 Trigger Framework

The Trigger Framework is a network of AND OR logical functions implemented with fast logical devices. Its function is to present the software trigger (Level 2) with compact information regarding the possible "physics" content of the event that passed the previous filters. The Trigger Framework is itself a hardware filter. The digital information generated by the Level 0 and Level 1 triggers is part of the input to the Trigger Framework. Input to the Trigger Framework include: calorimeter energy and muon candidates

from the Level 1 trigger, z position of the interaction point from Level 0, timing signals from the Master Clock System, busy signals from the rest of the electronic system, etc. This information is "compared" to a set of predefined conditions to generate up to 32 possible specific "physics" triggers. The Trigger Framework generates the Trigger Number that will be used by the system to organize and time-stamp the data. If at least one of the predefined conditions is met, the Trigger Framework will instruct the Data Aquisition System to proceed with the digitization of data for that specific event and will make available the appropriate information to the Level 2 trigger. The response of the Trigger Framework must be generated within $2.2\mu s$ to allow enough time for the electronic system to respond prior to the arrival of signals generated by the next interaction (recall that interactions take place every $3.56\mu s$.

2.5.4 Level 2

Once the analog data, generated by the different elements of the DØ detector, is digitized it is transferred to a set of 48 Microvax© 4000/60 computers known as *the farm* . The event encoded in the digitized data is partially reconstructed through code driven by the requirements of the physics of interest. The reconstruction is aimed at finding specific particles (electrons, muons, photons, hadronic jets, etc) and providing better calculation of the point of interaction (vertex), the $\not\!\!E_T$, etc. This information is then processed through some algorithms (filters) to determine if the data meet some predefined requirements. If at least one of the filters is fulfilled the data describing the total event is sent to the DØ Host computer and written to tape for de-

tailed processing later on. The maximum rate of information that the Level 2 can take is $200Hz$ and the maximum output rate is on the order of $2Hz$.

Chapter 3

Particle Identification and Reconstruction

The chief importance of knowledge by description is that it enables us to pass beyond the limits of our private experience. [...

..] . Inview of the very narrow range of our immediate experience, this result is vital, and until it is understood, much of our knowledge must remain mysterious and therefore doubtful.

"The Problems of Philosophy" Bertrand Russell

No todo lo que reluce es oro.

"Refranero Español"

The study of the angular distribution of the electron in the process

$$W \rightarrow e + \nu \tag{3.1}$$

requires the proper identification of electrons. Because the data used for this study corresponds to the data accumulated during the first run of the DØ detector the algorithms used to identify and characterize the particles in the events are those sanctioned by the DØ collaboration. In the following sections I present the identification procedures used for our analysis.

3.1 Reconstruction

The first task presented to any person whose goal is to analyze the data obtained in DØ, or in any other detector, is to convert or interpret the electronic data (raw data) representing energies and spatial information into particle information (physics data). This interpretation is called *reconstruction* and is carried out by a software package called DØ RECO. DØ RECO will identify and tag, for further processing, electrons, muons, photons, taus and jets. To each identified particle pertinent spatial and kinematic information is attached. The first pass of DØ RECO gave a loose set of particle parameters. More precise identification and parameterization of the particles involved in an event is part of the analysis and left to the individual physicist. The parameters attached to a particle by DØ RECO are : interaction vertex, total energy E_{total}, transverse energy E_t, missing transverse energy $\not\!\!E_T$, identification tag, and tracking information among others.

DØ RECO is a complex program consisting of thousands of lines of code created by the efforts of hundreds of physicists. Its complexity and size preclude the possibility of providing a good description here. In the following sections I will treat those elements in the reconstruction and identification

of particles that are pertinent to the present study. Of special interest to the work presented here are the electron reconstruction and the $\not\!\!E_t$ measurement. Reconstruction and identification will be presented together because, although in principle different, they support each other. My goal is to provide a concise and clear view of a complex system of analysis tools.

3.2 Interaction Vertex

To accurately calculate the kinematics of an event it is of vital importance to properly identify the point of interaction of the particles of such event. As an example let us consider the case of the transverse energy (E_t) and the longitudinal energy (E_z) of a particle identified by a cluster of cells in the calorimeter. If E_{total} is the sum of the energy of all the cells in the cluster then

$$\left.\begin{aligned} E_t &= E_{total} \times \sin\phi \\ E_z &= E_{total} \times \cos\phi \end{aligned}\right\} \tag{3.2}$$

where ϕ is the angle formed by the center of the cluster of cells in the calorimeter containing the E_{total} with the z axis of the detector. A simple calculation shows that the error made in the determination of the E_t could be important particularly when the object with energy E is in a plane near to the interaction vertex. Let us assume that the real vertex is at a point $P(\Delta z, 0)$ in a system of coordinates with origin in the assumed vertex, axis Oz along the z axis of DØ and axis Ot perpendicular to Oz and containing the center of the cluster defining the object. The error made in the determination of E_t is

$$\Delta E_t \;=\; E_t^* \times \frac{\Delta z}{z \;-\; \Delta z} \quad , \tag{3.3}$$

where E_t^* is the calculated E_t with the erroneous vertex. This can become unreasonably large for small values of z, as in the case of particles with high P_t and low longitudinal momentum.

The vertex position is obtained from information given by the VTX, CDC and FDC drift chambers of the Central Detector. The procedure consists of the following steps:

- ☐ Convert the hits information (raw data from the chambers) to tracks in the (r , ϕ) plane.
- ☐ Create tracks in the (r , z) plane using the information obtained in the previous step.
- ☐ Find the intersection of the tracks with the $z - axis$ of DØ.
- ☐ Separate the intersection points into clusters. Each cluster will define a vertex.
- ☐ Find the vertex corresponding to a cluster of intersection points by a Gaussian fit of the points in the cluster. The center of the Gaussian gives the vertex (z_{vtx}) position and the deviation of the fit is a measure of the uncertainty of the vertex position. Two vertexes are considered well defined when their separation is 7cm or greater. The resolution of the vertex position along the z axis is better than 1cm and could be as good as 0.65cm, depending on the number of tracks associated with the vertex.

- □ Obtain, if necessary, a new (x_{vtx} , y_{vtx}) position of the vertex by a Gaussian fit of the distances in x and y of the tracks associated with the obtained vertex by the preceding step. Otherwise, the (x_{vtx} , y_{vtx}) is assumed to be the one obtained at the beginning of a store for all the events in the same store.

A more detailed study of the error contributions of the vertex uncertainties to the E_t calculations is given by M. Settles and J. Linnemann [40].

3.3 Jets.

Any particle passing through the calorimeter will deposit part of its energy in the calorimeter leaving a *pattern signature* of energized cells. The identification of a particle (see 2.2.1) is reached by comparing the *pattern* left in the calorimeter with the expected patterns of different particles. The response of the Central Detector and of the Muon Detector helps to make the proper decision. There is, thus, nothing intrinsically different in the response of the calorimeter between an electron and a photon or a jet. The study of the shape of the cluster of energized cells within the calorimeter is what allows us to identify the nature of the particle responsible for the observed *pattern* . In all cases the first step in identification consists of defining which energized cells can be considered as pertaining to a particle o jet. This first step is then common to single particles as well as jets. For the remainder of this chapter the term jet will apply to hadronic jets as well as to any other types of particles unless otherwise stated.

The DØ collaboration uses two algorithms to create sets of related ener-

gized cells: the *cone* algorithm and the *nearest neighbor* algorithm.

3.3.1 The cone algorithm.

Experience tells us that the showers generated by particles interacting inside the calorimeter are confined in a cone with its vertex in the interaction point or in the intersection point of the trajectory of the particle and the calorimeter proper. This cone is defined in the (η , ϕ) space of the detector. These cones are reconstructed following three procedures, each consisting of several steps. The procedures are called : pre-clustering, clustering and jet merging.

3.3.1.1 Pre-clustering

1) Create an ordered list in E_t of the towers in the calorimeter with E_t greater than a given threshold, normally greater than 1 GeV. These towers are typically 0.1×0.1 in η , ϕ .

2) Start with the tower with the highest E_t. Define it as the *tower-seed* and its coordinates in (η , ϕ) as (η_{seed} , ϕ_{seed}). Create a precluster of cells containing all cells within a *pyramid* whose base, defined in the (η , ϕ) space, is $\eta = \eta_{seed} \pm .3$ and $\phi = \phi_{seed} \pm .3$. The axis of the pyramid is defined by the *tower-seed* . Any tower included in the precluster is eliminated from the ordered list of towers. This reduces the number of towers to be considered as possible seeds for a jet.

3) Repeat the # 2 until the ordered list of towers is exhausted. As a result of these steps, an ordered list of pre-clusters has emerged.

3.3.1.2 Clustering

1) Start with the precluster with the highest E_t and assign to it as preliminary jet-axis the one (η_{seed} , ϕ_{seed}) of the tower used to generate the precluster. Include all cells within a cone of radius

$$\Delta R = \sqrt{\Delta\eta^2 + \Delta\phi^2} \leq R_{cone} \tag{3.4}$$

in a new cluster and find the new jet-axis as the weighted centroid of the cone.

2)

Calculate the distance

$$\mathcal{D}^{\eta,\phi}_{j1,j2} = \sqrt{(\eta_{j1} - \eta_{j2})^2 + (\phi_{j1} - \phi_{j2})^2} \tag{3.5}$$

in η , ϕ space between the new and previous jet-axis. If this distance is greater than 0.001 repeat the process using the new jet-axis as the (η_{seed} , ϕ_{seed}). This iteration process continues until $\mathcal{D}^{\eta,\phi}_{j1,j2} \leq 0.001$ or the number of iterations reaches a predefined limit. Although Monte Carlo studies show that three or four iterations are sufficient to reach stability, there exists the possibility of finding an unstable situation where two or more apparent jet-axis are found. The limitation imposed in the number of iterations allowed takes care of these situations.

3)

Repeat the previous steps until the ordered list of pre-clusters is exhausted. If the total energy of a cluster generated by the previous procedures is above a threshold of 8 GeV, this cluster is considered a jet and becomes part of an ordered list of jets.

The list of jets generated by the previous procedures is exhaustive in the sense that all cells of the calorimeter are associated with **at least** one jet.

3.3.1.3 Jet Merging

In principle, each cell in the calorimeter with an energy above the 1 GeV threshold either belongs to a single jet, in which case its total energy contributes to the energy of the jet, or is shared by more than one jet, in which case its energy should be also shared by them. In the way the cells are assigned to jets, by the previous procedures, it is very possible for some jets to share several cells. If nothing is done at this point a cell can be counted more than once when the energy of one event (as the sum of the energies of all jets in the event) is calculated. To avoid these problems the ordered list of jets is processed through the Jet Merging algorithm.

Starting with the second jet in the ordered list the following procedures are followed:

1)

If the distance $D^{\eta,\phi}_{j1,j2}$, between the axis of the jet being tested and the previous one in the list is less than 0.001, the new jet is dropped from the list. This could happen due to roundoff errors.

2)

If $D^{\eta,\phi}_{j1,j2} > 0.001$ and there are cells shared by the two jets, then a merging fraction MS is calculated. The merging fraction is defined as

$$MS = \frac{\sum E^{common}_{t,i}}{E^{min}_{t}} \tag{3.6}$$

with E_t^{common} as the transverse energy of cell shared by both jets, and E_t^{min} the minimum of the transverse energies of the two jets.

3)

If $MS > 0.5$, the two jets are merged and all cells from both original jets are assigned to it.

If $MS \leq 0.5$, the cells shared by both jets are reassigned to only one jet, the one whose axis is closer to the cell in the (η , ϕ) space.

4)

A new jet-axis is recalculated for the new jets taking in to consideration all the cells assigned to the jet by the previous procedure.

3.3.2 The Nearest Neighbor Algorithm.

For the identification and characterization of electrons DØ normally uses a very simple but powerful algorithm, namely the *Nearest Neighbor* algorithm. This algorithm consists of the following steps:

1)

Create an ordered list in E_t of the EM towers in the calorimeter. All EM towers with an energy above a predefined threshold, normally 1 GeV, are listed.

2)

Start with the EM tower of higher energy. Create a cluster of towers by attaching to the original tower any tower from the ordered list that is *touching* it and delete those towers from the original list.

3)

Include in the cluster any tower from the ordered list that is *touching* any tower belonging to the cluster and delete those towers from the original list.

4)

Repeat the previous step until no more towers adjacent to the cluster are found or until the number of towers included in the cluster reaches a predefined number.

Both algorithms described here will identify jets within the DØ detector. Further work is needed to properly identify the particle(s) creating the jet. Discriminating algorithms exist to identify electrons and photons as the source of the jet. Work is in progress to be able to separate jets produced by quarks from these generated by gluons.

For the work presented here the proper identification of electrons is crucial.

3.4 Missing Transverse Energy ($\not\!\!E_t$).

When neutrinos are generated in an interaction process the kinematics of the event become difficult to analyze. Neutrinos interact very weakly with matter and, as a result, almost 100% of the time they will escape the detector without depositing any energy. A case in point is the process that is the subject of our study

$$q + \bar{q} \rightarrow W \rightarrow e + \nu_e \quad . \tag{3.7}$$

The neutrino that appears in the final state will have an energy that is not directly measurable. On the other hand, if we knew the kinematics of the initial state $(q + \bar{q})$ then, by conservation laws, we could infer the energy and momentum of ν_e. Although the longitudinal momenta of the initial partons is not known, the transverse momentum of the initial state is almost zero. This permits us to write

$$\sum_{allparticles} E_x^{total} = 0 \tag{3.8}$$

$$\sum_{allparticles} E_y^{total} = 0 \tag{3.9}$$

and, recalling the expression 3.2

$$\sum_{i=1}^{n} E_{t,i}^{CAL} \times \cos\phi_i + \not{E}_x = 0 \tag{3.10}$$

$$\sum_{i=1}^{n} E_{t,i}^{CAL} \times \sin\phi_i + \not{E}_y = 0 \tag{3.11}$$

$$\not{E}_t^{CAL} = \sqrt{(\not{E}_x)^2 + (\not{E}_y)^2} \ , \tag{3.12}$$

where $E_{t,i}$ is the transverse energy deposit in cell i of the calorimeter as defined in 3.2.

The $\not{E}_t^{CAL}$ just defined is called the Calorimeter Missing Transverse Energy. The *true* $\not{E}_t$ of the event is obtained after the energy of jets has been corrected and the expected energy deposit in the calorimeter by any muon is taken into account.

Studies done by M. Paterno [42] [43] show that the resolution of the calorimeter missing E_t can be parameterized as

$$\sigma(\not{E}_t^{CAL}) = a + b \times S_t + c \times S_t^2 \tag{3.13}$$

where

$$a = 1.89 \pm 0.05\ GeV \quad (3.14)$$

$$b = (6.7 \pm 0.7) \times 10^{-3} \quad (3.15)$$

$$c = (9.9 \pm 2.1) \times 10^{-6}\ GeV^{-1} \quad . \quad (3.16)$$

Figure 3.1 on the next page shows a recontructed event on the XY plane using RECO. The outer ring corresponds to the calorimeter and it displays the hadronic and electromagnetic energies measured by the detector as well as the calculated $\not\!\!E_T$. The other rings correspond to the TRD (4), the CDC (3) and the VTX. The reconstructed tracks are shown as solid lines and points represent particle detection by the TRD and VTX. The rectangles represent energy deposited with the height of the rectangle proportional to the energy measured.

3.5 Electrons

In the case of electrons (taus), it is expected that the *pattern* created by the *shower* emanating from them will be relatively narrow and almost totally contained within the EM of the calorimeter. The algorithms used to identify jets generated by electrons in DØ make use of these expectations.

3.5.1 Electron candidates

A first look at the characteristics of a jet, based on the expected signature for an electron, determines whether the jet can be an electron. The following

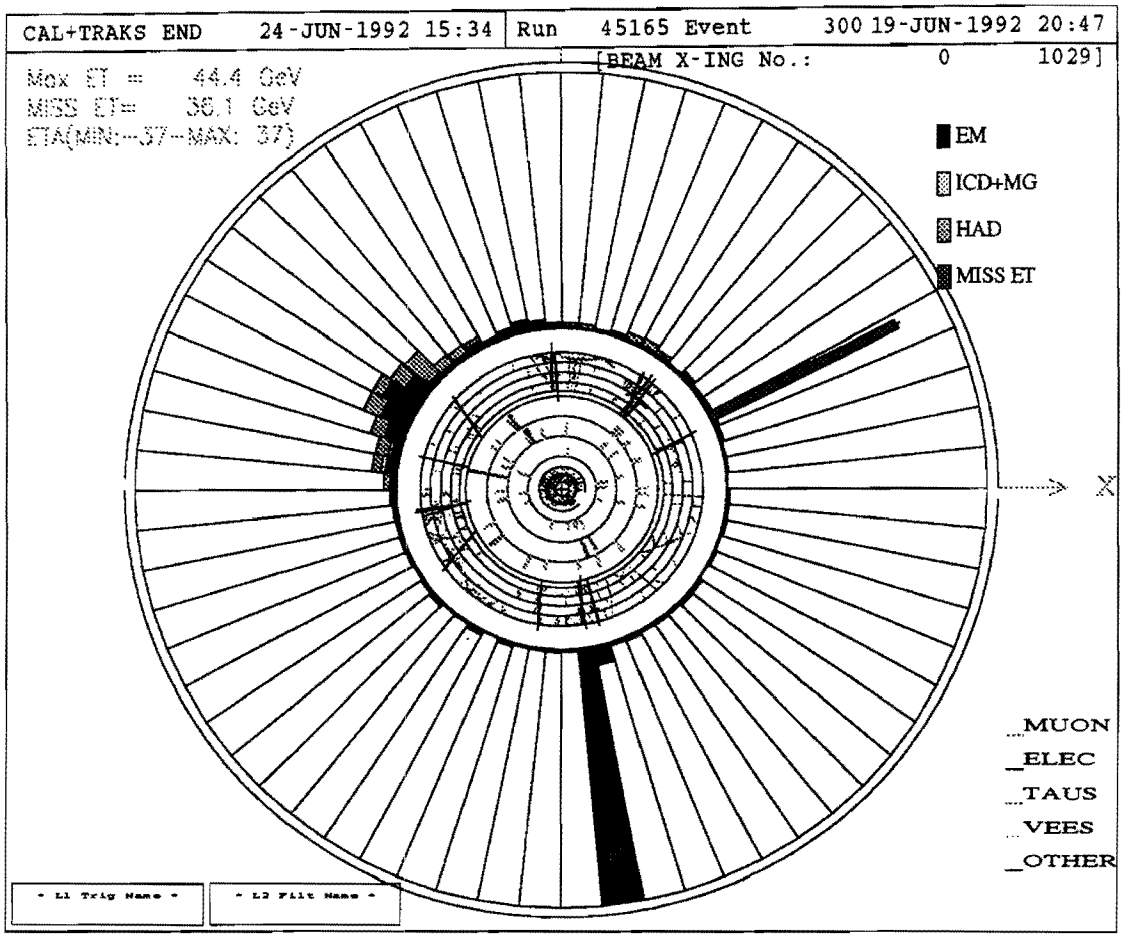

Figure 3.1: Typical W event.

Proyection on the XY plane of a reconstructed event.

are the conditions imposed over a jet to identify it as a possible electron candidate:

- The Electro-Magnetic energy fraction ($\mathcal{F}_{EM}$) of the jet must be at least 90%. $\mathcal{F}_{EM}$ is defined as

$$\mathcal{F}_{EM} = \frac{100 \times \sum_i^n E_{EM}^{Total}}{\sum_i^n E_{EM}^{Total} + \sum_j^m E_{HADR}^{Total}} \tag{3.17}$$

  where the indices i and j run through all the cells of the electromagnetic and hadronic sections of the calorimeter contained in the cluster that defines the jet. This requirement is an application of the assumption that a shower generated by an electron will be almost totally contained within the EM section of the calorimeter.

  Studies done in the testing of the calorimeter in a controlled situation show that this simple requirement is 99% efficient in detecting electrons whose energies range from 10 to 150 GeV.

- The energy deposited outside the central tower, the one used as the seed for the cluster, should not exceed 60% of the total energy of the jet. This is a direct application of the assumption that the showers generated by electrons are *narrow* .

- There must be at least one track in the Central Detector matching the cluster in the calorimeter. A matching track is defined as a track contained in a pyramid whose axis corresponds to the axis of the jet under consideration, whose apex is in the interaction vertex, and whose base, defined in (ϕ, η), is a square of 0.1 $\times$ 0.1 radians. This condition reflects the fact that an electron is an ionizing particle and, therefore, will generate a signature in the VTX, CDC or FDC. This feature is of importance in distinguishing between electrons and photons.

3.5.2 Electron selection

Not all the jets that meet the above conditions are electrons. Several conditions can lead to the misidentification of other particles as electrons. For example, a pion can give signatures very similar to the signature of an electron. As a result, other more restrictive conditions need to be imposed before an electron candidate is declared a *true* electron. The parameters used for these more restrictive conditions are: *cluster shape, cluster isolation, tracking significance* and $\frac{dE}{dx}$.

- Cluster shape

  A closer study of the expected shapes of the energy clusters developed in the calorimeter by different types of particles provides a good method for their identification. We said earlier that a pion could leave a signature very similar to the signature pertaining to an electron. Nevertheless, the way that the shower is generated for each type of particle is expected to be different. In the case of the pion the shower should develop earlier and provide a little fatter profile of the energy cluster. Also, an electron, even a very energetic one, should not deposit any commensurable energy in the hadronic calorimeter beyond the first layer. These facts are used in a technique to generate a likelihood parameter that defines how close the pattern of the energy cluster, created by a particle passing through the calorimeter, is to the predicted signature of an electron. Using calorimeter test data [44] [45] and Monte Carlo studies, a 41x41 covariant matrix is defined as follows:

$$\mathcal{M}_{i,j} = \frac{1}{N}\sum_{n=1}^{N}(x_i^n - \langle x_i \rangle)(x_j^n - \langle x_j \rangle) , \qquad (3.18)$$

where x_i^n is the value of observable i for electron n and $\langle x_i \rangle$ is the mean value of observable i for the sample of N electrons used. Its inverse $\mathcal{H} = \mathcal{M}^{-1}$ is the so-called $\mathcal{H} - matrix$ used in the calculation of a likelihood parameter defined as:

$$\chi^2 = \sum_{i,j} (x_i^k - \langle x_i \rangle) \mathcal{H}^{i,j} (x_j^k - \langle x_j \rangle). \tag{3.19}$$

Optimum cuts for the identification of electrons were obtained using test beam data. Figure 3.2 on page 84 shows how the distributions of χ^2 for electrons (non hatched distribution) and pions (hatched distribution) are well separated. The dots in the figure correspond to the distribution of electrons from the W boson decay and show here as reference. The χ^2 cut will be, by its definition, dependent on the fluctuations of the electromagnetic showers. The separation between electrons and pions is better in the central region of the calorimeter (where the fluctuations are small) than in the EC where a greater cut-off value must be used to accommodate greater fluctuations.

- Cluster isolation

A restrictive application of the concept of *narrow* energy distribution in clusters generated by electrons/photons versus a more diffused distribution of the energy in a cluster generated by a hadronic shower provides a good tool to identify electron-like particles. If we consider two cones of radii $\Delta R_{outside}$ and ΔR_{inside} in $\eta - \phi$ space with their central axis coinciding with the axis of the cluster (as previously defined) and their vertex in the event vertex, then the parameter

$$ISO = \frac{E^{total}(\Delta R_{outside}) - E^{EM}(\Delta R_{inside})}{E^{EM}(\Delta R_{inside})} , \tag{3.20}$$

gives a good measure of how concentrated the energy of the cluster is around the axis of the cluster. This parameter ISO is also a measure of how isolated an electron-like particle is from other particles, hence its name ISOlation Fraction.

- Tracking significance

  Under ideal circumstances, and in the absence of multiple scattering, a line drawn from the interaction point to the center of mass of a cluster (ie. the cluster axis) should coincide with one, and only one, track from the VTX and CDC or FDC detectors. In practice, ambiguities in the tracking system, inaccuracies in the determination of the center of mass of a cluster in the calorimeter, and multiple scattering make this one-to-one correlation almost impossible. Instead of trying to identify one single trajectory from the tracking system with a cluster in the calorimeter, what is done is to define a cylindrical volume in space whose axis coincides with the axis of the cluster under consideration and with a small radii. Then, any track defined in the central tracking system and contained in this cylinder is associated with the energy cluster in the calorimeter. For a fixed radii of the cylinder it is expected that the number of tracks associated with a cluster will be relatively small when the cluster corresponds to an electron/photon. The number of tracks inside the above defined cylinder TRK is called tracking significance.

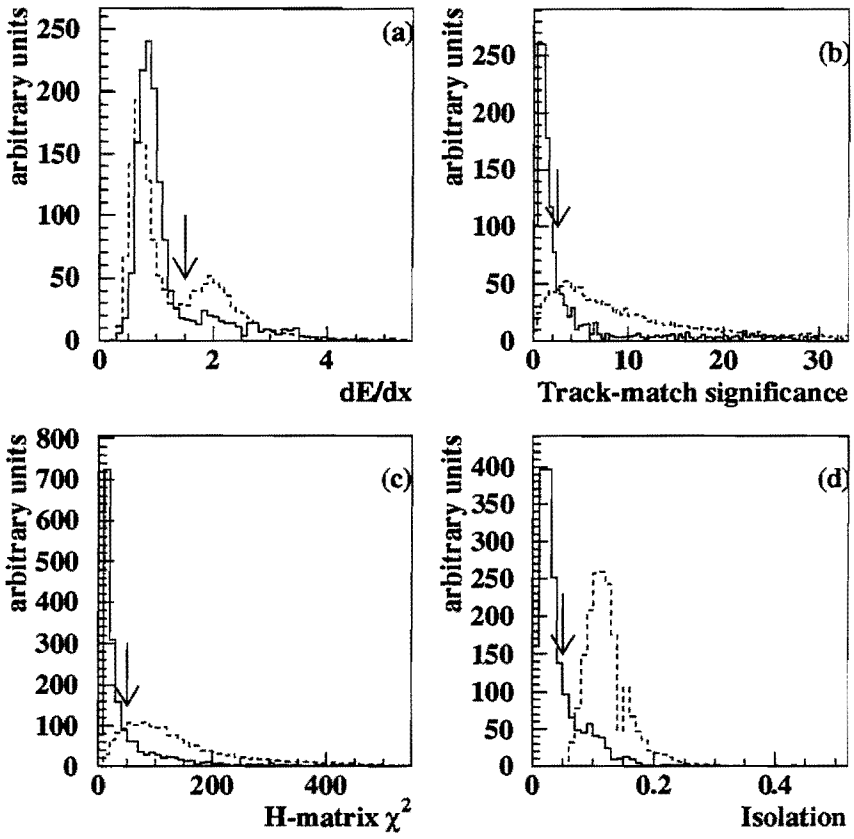

Figure 3.2: **Electron selection parameters.**

- dE/dx

  As mentioned above, the DØ detector does not have a central magnetic field. The absence of this field creates some ambiguities in the identification of particles. In particular, the detector is unable to distinguish between positive and negative particles or to separate pairs of charged particle-antiparticle. Also, it is difficult to make a clear distinction between photons and electrons. The TRD is designed to distinguish

minimal ionizing particles (ie. electrons, muons) from others (ie. photons converting in pairs e^+ e^-). Furthermore, the ionization per unit length (dE/dx) in the CDC and FDC drifting chambers can de used for the same purpose. Figure 3.2 shows the distribution of dE/dx (broken line) for tracks found in the CDC for particles identified by the hardware trigger as possible electrons. The first peak, at the value of dE/dx of one, is identified mainly with electrons whether the peak around dE/dx equal to 2 is mostly due to $\gamma \rightarrow e^+ e^-$. The efficiency of a cut (continous line) based on the dE/dx is not very good; only about 85% of true electrons pass this cut with a reduction in background of a factor of 2. The TRD information does not provide any better signal/background efficiency.

Chapter 4

Framing the Problem

If you would have a thing shrink,

You must first stretch it;

If you would have a thing weakened,

You must first strengthen it;

If you would have a thing laid aside,

You must first set it up;

If you would take from a thing,

You must first give to it.

"Tao Te Ching"

Lao Tzu

"En el ejercíto - decía - no se dan conferencias sobre el fusil; cada soldado debe desmontar y volver a montar su arma, sirviéndose de las mismas palabras que el instructor. Depués de veinte ejercicios, el soldado sabe lo que es un fusil y tiene un vocabulario para decir lo que sabe. De la

misma manera, no se aprende a pensar escuchando a un hombre que piensa bien. Lo que es necesario es desmontar sus propios argumentos y después volver a montarlos, hasta que el tema y el vocabulario formen parte de uno mismo."

"Destinos ejemplares. (Alain)"

André Maurois

4.1 A Blue Print

The theoretical background for this study has been presented in chapter 1 and a description of the instrumentation and general software tools used have been described in subsequent chapters. Now it seems pertinent to "frame" the work at hand. This implies showing the link between the theory and the experiment, and laying out the process by which the available data will be analyzed. In this vein the present chapter will present the theoretical predictions on which this work is based, followed by a feasibility study regarding the possibility of detecting and measuring the parameters of the theory and finally, a selection of the method that will be used to analyze the data at hand. A brief justification of the selected method will complete this chapter. Subsequent chapters will deal with the selection and analysis of data. The last chapter will present the results as well as propose suggestions for further analysis.

P_T^W	A_0	$A_4/2$	P_T^W	A_0	$A_4/2$
2.0	$9.4947597E-04$		80.0	0.6386524	0.4373227
4.0	$4.1198605E-03$		100.0	0.7298066	0.3866610
6.0	$9.6914293E-03$		120.0	0.7849026	0.3504058
8.0	$1.7797949E-02$		140.0	0.8220285	0.3213906
10.0	$2.8418804E-02$	0.7589031	160.0	0.8571729	0.2997898
20.0	0.1113208	0.7125124	180.0	0.8750306	0.2792248
40.0	0.3333014	0.6055024	200.0	0.9018641	0.2638432
60.0	0.5152015	0.5080132			

Table 4.1: **Values of A_0 and A_4 as function of P_T^W .**
Courtesy of E. Mirkes (private communication).

4.2 Theoretical Predictions

As presented in the first chapter, Mirkes has shown that the proper description of the angular distribution of the charged lepton(s), when represented in a particular frame of reference, resulting from the leptonic decay of the W(Z) boson, follows the expression:

$$\frac{d\sigma}{dP_T^2\ dy\ d\cos\theta} = K_\theta(1 + \alpha_1 \cos\theta + \alpha_2 \cos^2\theta) \qquad (4.1)$$

and

$$\frac{d\sigma}{dP_T^2\ dy\ d\phi} = K_\phi(1 + \beta_1 \cos\phi + \beta_2 \cos 2\phi + \beta_3 \sin\phi + \beta_4 \sin 2\phi) \ , \qquad (4.2)$$

where the meaning of the coefficients $\{\alpha_1,\ \alpha_2\}$ and $\{\beta_1,\ \beta_2,\ \beta_3,\ \beta_4,\}$ was defined in the first chapter of this work. E. Mirkes also calculated the angular

coefficients $A_i \; \forall i \in (1,..,7)$. Of these, A_0 and A_4 are reproduced in table 4.1 on the preceding page. From A_0 and A_4 the coefficients in 4.1 and 4.2 on the same page are easy to obtain using the expressions

$$\begin{array}{lllllll} A_0 & = & \frac{2(1-\alpha_2)}{3+\alpha_2} & A_2 & = & 2\,\beta_2 & A_3 & = & \frac{16\,\beta_1}{3\pi} \\ A_4 & = & \frac{4\alpha_1}{3+\alpha_2} & A_5 & = & 2\,\beta_4 & A_7 & = & \frac{16\,\beta_1}{3\pi} \end{array} \tag{4.3}$$

and solving for α_1 and α_2. Their values are presented in table 4.2. Note that the corresponding values for the case of $P_T^W = 0$ are included. It is important to recall that when the $P_T^W = 0$, no QCD effects are present and, as a result, for these special cases, the phenomenology corresponds to *weak interactions* only. Although both α_1 and α_2 have been calculated, only α_2 is

P_T^W	α_1	α_2	P_T^W	α_1	α_2
0.0	**2.0**	**1.0**	60.0	0.807991	0.180666
2.0	$\approx$ 2.	0.9981020	80.0	0.662949	0.0318507
4.0	$\approx$ 1.9	0.9917777	100.0	0.566576	−0.0693895
6.0	$\approx$ 1.8	0.9807112	120.0	0.503293	−0.1273680
8.0	$\approx$ 1.6	0.9647180	140.0	0.455546	−0.1651600
10.0	1.49654	0.9439590	160.0	0.41970	−0.2000292
20.0	1.34989	0.7890970	180.0	0.388483	−0.2174210
40.0	1.03802	0.428618	200.0	0.363688	−0.243151

Table 4.2: **Calculated values for α_1 and α_2.**

of interest for this analysis (the reason for this statement will be presented later). Fig. 4.1 on the facing page shows the values of α_2 superimposed with a polynomial on P_T^W. The agreement between the calculated values and the

polynomial(s) is excellent. Thus, a good functional description for α_2 is

$$\alpha_2 \cong 1 + P_2 q^2 + P_3 q^3 + \ldots \tag{4.4}$$

where $q \equiv P_T^W$. A major goal of the analysis presented here is to deter-

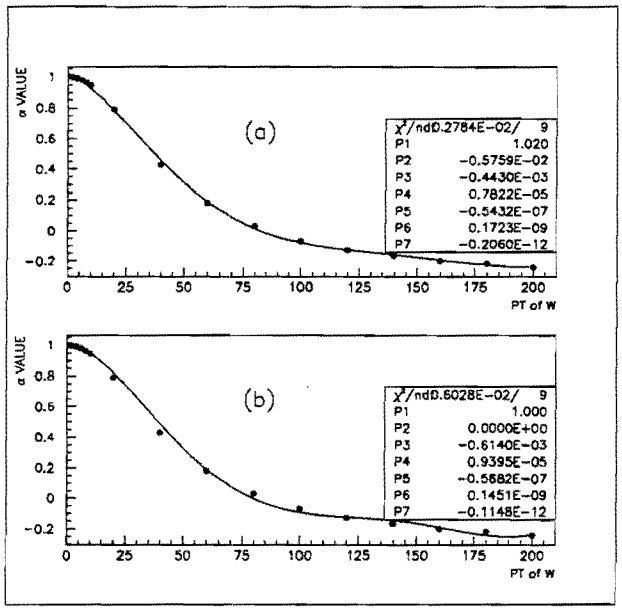

Figure 4.1: **Fitting of α_2 to a polynomial in P_T^W.**

a) Without extra constraints,

b) Forcing the polynomial to pass through (1,0)and be tangent to the horizontal axis for $P_T^W = 0$.

mine if the data at hand is consistent either with 4.1 on page 89 or with $\frac{d\sigma}{dP_T^2\ dy\ d\cos\theta} = K_\theta(1 \pm \alpha_2 \cos\theta)^2$.

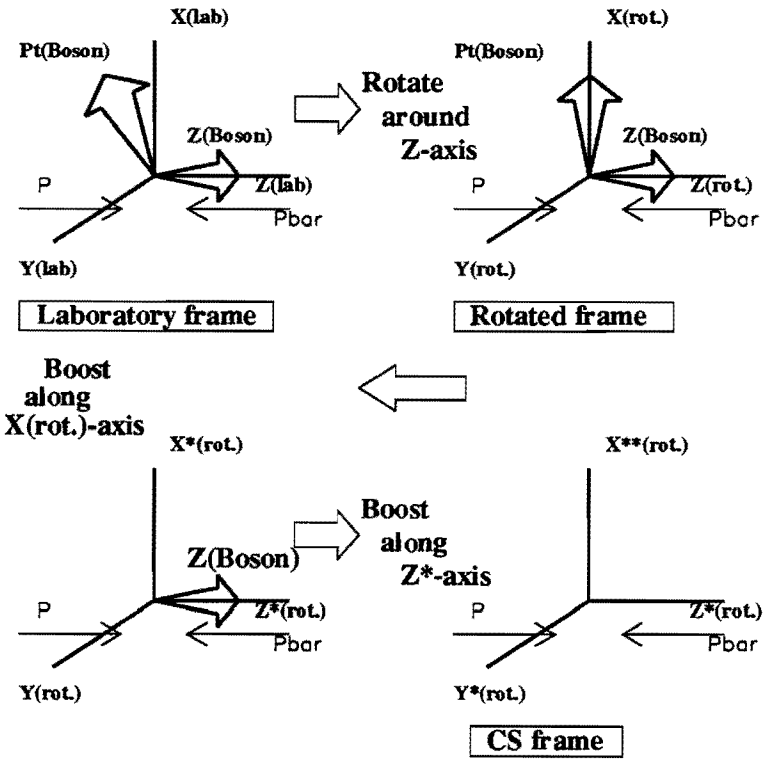

Figure 4.2: **The Collins-Soper frame in relation to the Laboratory frame.**

4.3 The Frame of Reference

E. Mirkes's work (see [11]) uses the Collins-Soper frame [26] as the frame of reference to calculate the effects of the QCD interactions with the W decay.

The choice of this frame of reference is, by no means, arbitrary. The process,

$$W \rightarrow l + \nu \tag{4.5}$$

as produced in $p\bar{p}$ collisions, cannot be kinematically constrained because of inherent errors in the measurement of the longitudinal component of the neutrino's momentum. There is, however, a frame of reference in which these calculations can be performed using only measured values of the transverse momentum of the charged lepton and neutrino. This frame of reference is the Collins-Soper frame (CS frame), and has been used to calculate the angular distribution of the charged leptons in the process 1.3 at next-to-leading-order (NLO) .

It is important to have a good understanding of what the CS frame really is. Although used often in theoretical studies, seldom is it used in experimental work, and then only in a very peremptory manner. As part of this study it was necessary to become familiar with this frame of reference. The following paragraphs are intended to provide a good description of it.

The CS frame is a '**rest frame**' for the boson. It is chosen so that the z-axis bisects the angle formed by the momentum of the proton and the minus-momentum of the antiproton. In general the proton and antiproton beams are not exactly collinear; in the case of DØ this angle was of the order of 200 $\mu - radians$ in run 1-A (run 1992-1993). The x-axis is in a plane perpendicular to the z-axis and parallel to the transverse momentum of the W as shown in Fig. 4.2 on the facing page. With this choice of axis we make a Lorentz transformation to the rest frame of the W boson.

4.3.1 From Laboratory frame to CS frame.

Let us assume that the momenta of the charged lepton and neutrino in the laboratory frame of reference are

$$l_{lab} = [\, ll_x \,,\, ll_y \,,\, ll_z \,,\, ll_e \,] \tag{4.6}$$

$$\nu_{lab} = [\, l\nu_x \,,\, l\nu_y \,,\, l\nu_z \,,\, l\nu_e \,]. \tag{4.7}$$

The momentum of the W in this frame is then

$$w_{lab} = [lw_x, lw_y, lw_z, lw_e] \tag{4.8}$$

or

$$w_{lab} = [\, ll_x + l\nu_x \,,\, ll_y + l\nu_y \,,\, ll_z + l\nu_z \,,\, ll_e + l\nu_e \,]. \tag{4.9}$$

To go from the laboratory frame to the CS frame we take the following steps:

A) *Rotation*

Go to an intermediate frame in which the transverse momentum of the W has only the x component. This is accomplished by a rotation around the z-axis by an angle α

$$\alpha = cos^{-1} \left(\frac{lw_x}{\sqrt{lw_x^2 + lw_y^2}} \right). \tag{4.10}$$

The momenta in the rotated frame are

$$w_{rotated} = [\, w_x \,,\, 0 \,,\, w_z \,,\, w_e \,] \tag{4.11}$$

$$l_{rotated} = [\, l_x \,,\, l_y \,,\, l_z \,,\, l_e \,] \tag{4.12}$$

$$\nu_{rotated} = [\, \nu_x \,,\, -l_y \,,\, \nu_z \,,\, \nu_e \,]. \tag{4.13}$$

In matrix form the rotation is written as

$$\vec{\mathbf{a}}_r = \begin{bmatrix} \frac{W_x}{P_T^W} & \frac{W_y}{P_T^W} & 0 & 0 \\ -\frac{W_y}{P_T^W} & \frac{W_x}{P_T^W} & 0 & 0 \\ 0 & 0 & 1 & 0 \\ 0 & 0 & 0 & i \end{bmatrix} \times \vec{\mathbf{a}}_l \tag{4.14}$$

$$\vec{\mathbf{a}}_r = \Big[\mathcal{R}\Big] \times \vec{\mathbf{a}}_l \tag{4.15}$$

B) *Lorentz boost*

We want a frame of reference where the W is at rest and the z-axis bisects the angle formed by the momentum of the proton and the minus-momentum of the antiproton. To reach this frame we do a boost in the z direction first followed by a boost in the x direction. The momenta of the W and the charged lepton after the first boost are

$$w_{z-boosted} = [\, w_x \,,\, 0 \,,\, 0 \,,\, \sqrt{w_e^2 - w_z^2}\,] \tag{4.16}$$

$$l_{z-boosted} = [\, l_x \,,\, l_y \,,\, \frac{l_z w_e - l_e w_z}{\sqrt{w_e^2 - w_z^2}} \,,\, \frac{l_e w_e - l_z w_z}{\sqrt{w_e^2 - w_z^2}}\,] \tag{4.17}$$

and after the boost in the x direction we finally have the W at rest. The momenta of the W and the charged lepton in this frame of reference are

$$w_{CS} = [\, 0 \,,\, 0 \,,\, 0 \,,\, w_{CS}^e\,] \tag{4.18}$$

$$= [\, 0 \,,\, 0 \,,\, 0 \,,\, \sqrt{w_e^2 - w_x^2 - w_z^2}\,] \tag{4.19}$$

$$l_{CS} = [\, l_{CS}^x \,,\, l_{CS}^y \,,\, l_{CS}^z \,,\, l_{CS}^e\,] \tag{4.20}$$

$$= [\, \frac{l_x w_e^2 - l_e w_e w_x - l_x w_z^2 + l_z w_x w_z}{M_w \sqrt{w_e^2 - w_z^2}} \,,\, l_y \,,\, \frac{l_z w_e - l_e w_z}{\sqrt{w_e^2 - w_z^2}} \,,\, \frac{l_e w_e - l_x w_x - l_z w_z}{M_w}] \tag{4.21}$$

where we have the momenta expressed as a function of the momenta in the rotated frame and the mass of the W. The W's mass is represented by

$$M_w = \sqrt{w_e^2 - w_x^2 - w_z^2}\,. \tag{4.22}$$

In matrix form it is written

$$\vec{\mathbf{a}}_{\mathrm{CS}} = \left[\mathcal{L}\right] \times \vec{\mathbf{a}}_{\mathrm{r}} \tag{4.23}$$

$$\vec{\mathbf{a}}_{\mathrm{CS}} = \left[\mathcal{L}\right] \times \left[\mathcal{R}\right] \times \vec{\mathbf{a}}_{\mathrm{l}} \tag{4.24}$$

4.3.2 Show independence from longitudinal momentum.

The expressions given in the previous section do not make clear the independence of the charged lepton momentum in the CS frame from the longitudinal momentum of the neutrino in the rotated or laboratory frame. To show this independence in a clear form it is necessary to rewrite the momentum of the charged lepton in a way that only the transversal momenta of the charged lepton and neutrino appear in explicit form.

Let us take the x component of the momentum of the charged lepton as given in 4.21

$$l^x_{CS} = \frac{l_x w_e^2 - l_e w_e w_x - l_z w_z^2 + l_z w_x w_z}{M_w \sqrt{w_e^2 - w_z^2}} \,. \tag{4.25}$$

Written in this form it shows a direct dependence between l_z, and of ν_z through w_z and w_e. The denominator can be written as

$$M_w \sqrt{w_e^2 - w_z^2} = M_w \sqrt{M_w^2 + (P_t^w)^2} \,. \tag{4.26}$$

The algebra involved in rewriting the numerator is slightly more complex. We have

$$l_x w_e^2 - l_e w_e w_x - l_x w_z^2 + l_z w_x w_z \;=\; l_x(w_e^2 - w_x^2 - w_z^2) + l_x w_x^2 - l_e w_e w_x + l_z w_x w_z \tag{4.27}$$

and using 4.22 and 4.9

$$= M_w^2 l_x + w_x(l_x w_x + l_y w_y + l_z w_z - l_e w_e)\ . \tag{4.28}$$

Again, substituting $\vec{w} = \vec{l} + \vec{\nu}$, we write

$$= M_w^2 l_x + (l_x + \nu_x)(l_x(l_x + \nu_x) + l_y(l_y + \nu_y) + l_z(l_z + \nu_z) - l_e(l_e + \nu_e))\ , \tag{4.29}$$

carrying out the multiplication and collecting terms in an appropriate manner

$$= M_w^2 l_x + (l_x + \nu_x)(l_x^2 + l_y^2 + l_z^2 - l_e^2) + (l_x + \nu_x)(l_x\nu_x + l_y\nu_y + l_z\nu_z - l_e\nu_e). \tag{4.30}$$

Making proper substitutions,

$$= M_w^2 l_x + (l_x + \nu_x)M_e^2 - (l_x + \nu_x)\frac{M_w^2}{2} \;=\; M_w^2 l_x - (l_x + \nu_x)\frac{M_w^2}{2} \tag{4.31}$$

and using 4.25 and 4.26 we obtain the expression for the x component of the momentum of the charged lepton in the CS frame in a way where the only dependence of the longitudinal momentum of the neutrino appears through the mass of the boson M_w^2

$$l_{CS}^x = \frac{M_w(l_x - \nu_x)}{2\sqrt{M_w^2 + (P_t^w)^2}} . \tag{4.32}$$

In a similar way we could arrive at the expression for z component of the charged lepton. Instead of trying to convert the expression found in 4.21 for l_{CS}^z directly, we can use the fact that in any frame of reference where the W is at rest, the expression

$$l_{W\ at\ rest}^e = \nu_{W\ at\ rest}^e = \frac{M_w}{2} \tag{4.33}$$

holds. It follows that

$$(l_{CS}^x)^2 + (l_{CS}^y)^2 + (l_{CS}^z)^2 = \frac{M_w^2}{4} . \tag{4.34}$$

From this last expression we have

$$l_{CS}^z = \pm\sqrt{(.5M_w)^2 - (l_{CS}^x)^2 - (l_{CS}^y)^2} , \tag{4.35}$$

which can be written as function of the mass of the gauge boson (M_w) and the transversal components of the momenta of the charged lepton and the neutrino:

$$l^z_{CS} = \pm\frac{1}{2}\sqrt{M_w^2 - \frac{M_w^2(l_x-\nu_x)^2}{M_w^2+(P_t^w)^2} - (l_y-\nu_y)^2} \tag{4.36}$$

Finally, we can write the expressions for the angular distributions of the charged lepton as:

$$\phi = Tan^{-1}(\frac{2l_y\sqrt{M_w^2+(P_t^w)^2}}{M_w(l_x-\nu_x)}) \tag{4.37}$$

$$cos\theta^* = \frac{l^z_{CS}}{l^e_{CS}} \tag{4.38}$$

or, for the last expression,

$$cos\theta^* = \pm\sqrt{1-\frac{(l^x_{CS})^2+(l^y_{CS})^2}{(.5M_w)^2}} \tag{4.39}$$

or

$$cos\theta^* = \pm\sqrt{1-(\frac{P^{lepton}_{t(CS)}}{.5M_w})^2}. \tag{4.40}$$

A look at 4.32, 4.36, 4.37 and 4.40 shows that these expressions are not "*directly*" dependent on the longitudinal momentum of the charged lepton or

the neutrino. What really happens is that this dependence appears in "*implicit*" form through the assignment of a particular value to the mass of the W boson. Nevertheless, the expressions obtained are in a more manageable form. In particular the expression for $cos\theta^*$ has a single ambiguity for the sign.

4.3.3 Orientation of the CS frame respect to the laboratory frame

The laboratory frame is a rigid spacial-temporal frame common to all events as defined in Chapter 2. The CS frame is a special frame of reference where the W is at rest and whose temporal axis has a unique orientation that is event dependent. It is important to have a good understanding of the orientation of the CS frame in order to understand the physical parameters defined in it. Let us consider unitary vectors representing the momenta of proton and antiproton respectively; in the laboratory frame of reference we have

$$P_{lab} = \frac{1}{\sqrt{2}}[\,0\,,\,0\,,\,1\,,\,i\,]\,, \tag{4.41}$$

and

$$\bar{P}_{lab} = \frac{1}{\sqrt{2}}[\,0\,,\,0\,,\,-1\,,\,i\,]\,. \tag{4.42}$$

And after the transformation, these become

$$
\begin{aligned}
P_{CS} &= \frac{w_e - w_z}{\sqrt{2}\, M_w \sqrt{M_w^2 + (P_t^w)^2}} \times \\
&\quad [\, -P_t^w \,,\, 0 \,,\, M_w \,,\, i\sqrt{M_w^2 + (P_t^w)^2}\,] \,, \\
\bar{P}_{CS} &= \frac{w_e + w_z}{\sqrt{2}\, M_w \sqrt{M_w^2 + (P_t^w)^2}} \times \\
&\quad [\, -P_t^w \,,\, 0 \,,\, -M_w \,,\, i\sqrt{M_w^2 + (P_t^w)^2}\,] \,.
\end{aligned}
$$

These expressions clearly show that the z axis in the Collins-Soper frame bisects the angle formed by the vectors along the movement of the proton and opposite to the movement of the antiproton. The angle formed by the direction of the proton and the z axis in the CS frame is

$$
\hat{\theta} = \arccos\left(\frac{M_w}{\sqrt{M_w^2 + (P_t^w)^2}}\right) \tag{4.43}
$$

In general the proton and antiproton beams are not exactly collinear. It is of interest to see how this non-collinearity will affect the expressions shown above. The non-linearity of the two beams can be taken into account by introducing a small component px in the expressions 4.41 and 4.42 as follows

$$
P^*_{lab} = \frac{1}{\sqrt{2 + px^2}} [\, px \,,\, 0 \,,\, 1 \,,\, i \,] \tag{4.44}
$$

$$
\bar{P}^*_{lab} = \frac{1}{\sqrt{2 + px^2}} [\, px \,,\, 0 \,,\, -1 \,,\, i \,] \tag{4.45}
$$

After boosting to the CS frame we have

$$P^*_{CS} = \frac{w_e - w_z}{\sqrt{2 + px^2}\, M_w \sqrt{M_w^2 + (P_t^w)^2}}$$
$$[\, -P_t^w + px(M_w^2 + (P_t^w)^2),\ 0\ ,\ M_w\ ,\ i\sqrt{M_w^2 + (P_t^w)^2}\,(1 + px\ P_t^w)\,]\ ,$$

$$\bar{P}^*_{CS} = \frac{w_e + w_z}{\sqrt{2 + px^2}\, M_w \sqrt{M_w^2 + (P_t^w)^2}}$$
$$[\, -P_t^w + px(M_w^2 + (P_t^w)^2),\ 0\ ,\ -M_w\ ,\ i\sqrt{M_w^2 + (P_t^w)^2}\,(1 + px\ P_t^w)\,]\ ,$$

showing that the orientation of the CS has not changed.

4.3.4 Errors introduced by not knowing the M_w event by event

Expressions 4.37 on page 100 and 4.40 on page 100 provide a means to obtain the angular distribution of the charged lepton in the process $W \rightarrow l + \nu$ based on measured quantities (l_x, l_y, ν_x *and* ν_y) and on the value of the mass of the W for the event under study. It is obvious that the direct dependency of ϕ and $cos(\theta^*)$ on the longitudinal momentum of the neutrino has been removed, but an indirect dependency is introduced by the use of M_w. To be able to calculate the *'exact'* value of ϕ and $cos(\theta^*)$ it is necessary to know the associated M_w in the event. It seems that we are not better off than before given that to know M_w requires the ability to measure the longitudinal momentum of the charged lepton and the neutrino, precisely what we said we could not do.

We can carry out the calculations by using a fixed value of M_w for all events instead of the correct value for each event. The question is: *What errors do we make using* M_w^{fixed} *?*

Using the following terms:

- ϕ_{real} and $cos\theta^*_{real}$ are the ϕ and $cos\theta^*$ that we could calculate if we were able to measure and use the correct M_w for each event.

- ϕ_{calc} and $cos\theta^*_{calc}$ are the ϕ and $cos\theta^*$ calculated using a fixed value M_w^{fixed} for all events.

then the errors are given by:

- absolute errors in ϕ and $cos\theta^*$

$$ae_\phi = \phi_{calc} - \phi_{real}$$

$$ae_{cos(\theta^*)} = cos\theta^*_{calc} - cos\theta^*_{real}$$

- the relative errors

$$re_\phi = \frac{ae_\phi}{\phi_{real}}$$

$$re_{cos(\theta^*)} = \frac{ae_{cos(\theta^*)}}{cos\theta^*_{real}}$$

The M_w^{fixed} will be the calculated value at DØ.

There is another type of error introduced in the determination of $cos(\theta^*)$. If the real M_W is known, then $M_W > (P^{lepton}_{t(CS)})^2$ and expression 4.40 on page 100 is always real. On the other hand, M_w^{fixed} can be much smaller than the real value of M_W for some events and $M_w^{fixed} > (P^{lepton}_{t(CS)})^2$ does not necessarily hold. Cases wherein that situation arises will give an imaginary

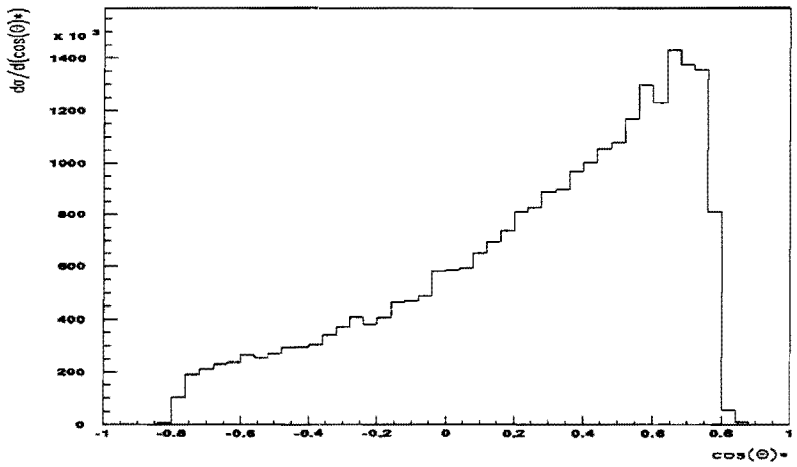

Figure 4.3: **Histogram showing the theoretical distribution** $\frac{d\sigma}{d\cos\theta}$

Theoretical case when no QCD effects are taken intoaccount.

value for $cos(\theta^*)$; i.e., a non-physical solution to equation 4.40 on page 100. The number of events that will give such an erroneous result is not trivial.

It is not easy to provide an analytical solution to the errors defined so far. Instead, a Monte Carlo study will be done.

4.4 Monte Carlo Generation

In order to carry out an unbiased and real study of the effects of the errors described in the previous section it is necessary to simulate the physics of the process $W \rightarrow l + \nu$ and its observables under different conditions. The best way to achieve this is to generate a Monte Carlo (MC) which includes parameters that control the effects under study. The MC used in this work consists of three major software packages:

■ **Event Generator:**

This part is based on code generated at CERN for the UA2 experiment. Several people, in particular D. Wood and H. Rajagopalan, modified it to work with DØ software. At this level the proper parameters defining the $\langle M_W \rangle$ and the $\langle \Gamma_W \rangle$ are introduced as well as parton and P_T^W distributions. The result of this part of the MC is a set of events that fully reproduces the W generation and decay through the lepton channel in a frame of reference where the W is at rest with the sole exception that no weighting for ϕ or $cos(\theta^*)$ has been introduced. The following variables:

$$\begin{aligned} \hat{s}^2 &\equiv M_W \text{ of the event} \\ \vec{l} &\equiv \{l^x_{rest},\ l^y_{rest},\ l^z_{rest},\ l^e_{rest}\} \\ \vec{\nu} &\equiv \{\nu^x_{rest},\ \nu^y_{rest},\ \nu^z_{rest},\ \nu^e_{rest}\} \end{aligned}$$

are made available to the next level

■ **Lorentz Boost:**

At this moment a decision is made to "select" the rest frame of the W. If the W is considered to decay in the CS frame then the events are weighted by:

$$\begin{aligned} Wg &= Wg(\phi) \times Wg(cos(\theta^*)) \\ &= (1 + \beta_1 \cos\phi + \beta_2 \cos 2\phi + \beta_3 \sin\phi + \beta_4 \sin 2\phi) \times \\ &= (1 + s\alpha_1 \cos\theta + \alpha_2 \cos^2\theta) \end{aligned}$$

or simply by

$$\begin{aligned} Wg &= Wg(cos(\theta^*)) \\ &= (1 + s\alpha_2 \cos\theta)^2 \end{aligned}$$

where s provides the proper sign. After the events are correctly weighted they are "boosted" to the laboratory frame of reference, again using the proper transformations. In the case of the CS frame, the transformation is given by

$$\vec{\mathbf{a}}_{\mathbf{lab}} = \left[\mathcal{T}\right]^{-1} \times \left[\mathcal{L}\right]^{-1} \times \vec{\mathbf{a}}_{\mathbf{CS}} \qquad (4.46)$$

where $\left[\mathcal{T}\right]$ and $\left[\mathcal{L}\right]$ correspond to the rotation and the boost described in the §§ "From laboratory frame to CS frame". They are the same as in equation 4.24 on page 97.

- **Response of the DØ Detector:**

  The four-vectors obtained from the previous step contain all the kinematic information of the event in the laboratory frame of reference. They represent what an imaginary spectator, tha does not interact with the event, will see. What a real spectator sees is quite different. The interaction of the event with the detector, the particles generated (or present) in the same interaction and the electronic baseline shifts due to previous interactions all contribute to the distortion of the pure kinematic information. It is necessary to model, the best way possible, all these processes in order to understand the data. In fact, because the neutrino passes through the detector without interacting with it, and the Central Tracking Detector laks a magnetic

Parameter Description	Nominal Value
EM energy resolution sampling	$S_e = 0.13$
constant	$C_e = 0.015$
noise	$N_e = 0.4\ GeV$
HAD energy resolution sampling	$S_H = 0.8$
constant	$C_H = 0.04$
noise	$N_H = 1.5\ GeV$
HAD energy scale	$\beta = .083$
Number of minimum bias events	1
Underlying Event Energy	$E_{UE} = 205\ MeV$
Calorimeter position resolution	$\sigma(z) \approx 0.7\ cm$
angular resolution	$\vartheta = 0.005\ rad$
CDC position resolution	$\sigma(z)_{cdc}\ approx\ 0.7\ cm$
W-width	$\Gamma_W = 2.1\ GeV$
Z-width	$\Gamma_Z = 2.5\ GeV$
Branching ratio (for τ)	BR($\tau \rightarrow e^{\pm}\nu\nu$) = 0.179

Table 4.3: **Fast MC parameters.**
These parameters are for the Central Calorimeter (CC) only.

field, of the nine quantities describing the electron and the neutrino ($\vec{e}^{\pm}$), $\vec{\nu}$ and sign of the charge of e only five are measured directly : e_x, e_y, e_z and the transverse momentum of the recoil of the event against the generated W r_x, r_y . The later, in reality, has two components, the true recoil due to the W plus all other momenta of the spectator quarks, other possible interactions in the same event, etc. By balancing the total transverse energy of the event it is possible to

obtain the P_T^W

$$P_T^W = \not{p}_T + P_T^e + P_T^u \tag{4.47}$$

$$P_T^\nu = \not{p}_T + P_T^u. \tag{4.48}$$

Thus, it is necessary to model correctly not only the response of the detector to one electron, but also the response to non electromagnetic jets as well as the effects due to P_T^u . The modeling of the detector response includes the following aspects [47]:

- **Electron**
  - Electron energy resolution, parameterized as

$$\frac{\sigma_E}{E} = \sqrt{C^2 + (\frac{S}{\sqrt{E_T}})^2 + (\frac{N}{E})^2}\,. \tag{4.49}$$

    This expression is the same as the one presented in chapter 2 §2.2.1 with the difference that the sampling term is function of the transverse energy instead of the total energy.
  - The angular resolution of the electron calculated from the resolution of the position of the electromagnetic cluster in the calorimeter and the position of the center of gravity of the track associated with the electron in the CDC. This modeling, as well as all the others mentioned here, are described in detail in the DØ Note 2929 mentioned above.
  - Recalibration of the energy scale of the electron is also done. This recalibration is necessary because the mass of the boson Z, as measured by DØ, is about 4% less than the LEP/SLC

standard. This recalibration was done using three sets of data: $Z \rightarrow e^+e^-$, J/ψ decays and π^0 decays. The energy scale is parameterized as follows:

$$E_{true} = \frac{1}{\alpha}(E_{measured} - \delta) \ . \qquad (4.50)$$

- Differences in response from module to module in the central calorimeter are also taken into account.

■ **Jets**

- The energy scale used for the P_T^W is different than the one used by the electrons. This is so because the momentum of the measured recoil is made by the sum of the momenta of hadronic jets. A correlation between electromagnetic energy scale and hadronic energy scale can be obtained. This is achieved by a careful comparison of the measurements of the P_T^Z as the sum of the transverse momenta of the two electrons from $Z \rightarrow e^+e^-$, and as direct measurement of the transverse momentum of the recoil. The relationship is a simple linear one

$$E_{hadronic} = \beta E_{electromagnetic} \ . \qquad (4.51)$$

with $\beta \approx .83$. The P_T^W is treated as a single jet.

- Jets are smeared the same way as electrons, using formula 4.49 on the preceding page but with different values for the parameters. All the parameters used by the MC, and their nominal values, are listed in table 4.3 on page 108 and are

the same as the ones used in the calculation of the W-mass [47].

- □ The underlying event is embedded in the data and its contribution to the measured value of the momentum of the recoil, as well as to its resolution, cannot be separated. Furthermore, the underlying event is instant luminosity dependent and the recoil (P_T^W) is not. The way to treat the problem is to include in the Monte Carlo the effects of the underlying event. This is done by adding to the W generated a minimum bias event chosen from a library (the library contains $\approx$ 40,000 events of real data with minimum bias) binned in luminosity. Such binning is done in a way that the events are distributed in luminosity corresponding to the luminosity of the W properly scaled.

The work to smear the momenta of a W-generating event in the Monte Carlo is crucial to be able to compare real data with MC data. The steps taken following the above descriptions, are summarized below.

- ■ A W event is generated by the "*event generator* " providing al four momenta components for the electron, neutrino and W.
- ■ The event is then boosted from the CS frame to the laboratory frame.
- ■ The momenta of the electron and the W are smeared using the appropriate resolution formulae.

- Both momenta are scaled using the corresponding scale factors.

- The P_T^W smeared, generated by the Monte Carlo, became identified with the measured recoil momentum:

$$P_{T,\ MC\ smeared}^{W} \iff P_{T,\ data}^{W} \tag{4.52}$$

$$P_{T,\ MC\ smeared}^{W} = -\ P_T^{Recoil} \tag{4.53}$$

$$= -\ P_T^{Recoil,\ inner} - P_T^{Recoil,\ outer} \tag{4.54}$$

$$P_{T,\ data}^{W} = -P_T^{Recoil,\ outer} - U(\mathcal{L},\ \text{outer}) \tag{4.55}$$

where the *inner* and *outer* refers to the energy of the recoil deposited inside or outside of a cone of predefined parameters and with its axis coincident with the direction of the electron. The term $U(\mathcal{L},\ \text{outer})$ is the *outer* part of the underlying event.

- To the smeared momentum of the electron is added the corresponding inner part of the underlying event. Because the measured momentum of the electron includes the inner part of the recoil it is necessary to correct for it. It is obtained:

$$P_{T,\ MC\ smeared}^{e} + U(\mathcal{L},\ \text{inner}) = \mathrm{P}_{\mathrm{T,\ data}}^{\mathrm{e}} - \mathrm{P}_{\mathrm{T}}^{\mathrm{Recoil,\ inner}} + \mathrm{U_{ZS}} \tag{4.56}$$

where U_{ZS} is a zero suppression corrective term. From the above the measured electron is identified with a corrected MC generated

electron as

$$P^{e}_{T,\ data} = P^{e}_{T,\ MC\ smeared} + U(\mathcal{L},\ \text{inner}) + \mathrm{P_T^{Recoil,\ inner}} - \mathrm{U_{ZS}} \tag{4.57}$$

- Finally, the momentum of the neutrino can be expressed in function of measured and smeared quantities.

$$\begin{aligned} P^{\nu}_{T,data} &= P^{W}_{T,\ data} - P^{e}_{T,\ data} \\ &= -P_T^{Recoil,\ outer} - U(\mathcal{L},\ \text{outer}) - \mathrm{P^{e}_{T,\ MC\ smeared}} + \\ &- U(\mathcal{L},\ \text{inner}) - \mathrm{P_T^{Recoil,\ inner}} + \mathrm{U_{ZS}} \\ &= - P^{e}_{T,\ MC\ smeared} - U(\mathcal{L}) + \mathcal{U}_{ZS} \end{aligned} \tag{4.58}$$

A careful study of the effects of the underlying event in the corrections of the energy of the electron in a W event can be found in [48].

4.5 Monte Carlo Analysis of Errors

Using the Monte Carlo generator described in the previous section it is possible to study the effects of the different errors mentioned in § 1.3.4 as well as the effects of the detector itself. 300,000 MC events were generated. Only studies related to

$$\frac{d\sigma}{d(P^{W}_{T})^2\ dy\ d\cos\theta} = K_\theta(1 + \alpha_1 \cos\theta + \alpha_2 \cos^2\theta) \tag{4.59}$$

will be done.

The histogram of Fig. 4.3 on page 105 shows the theoretical distribution for $\cos\theta^*$ in the CS frame of reference when all four components of the

electron and the neutrino are known. The distributions do not reach ± 1 because the MC has a cut in the minimum values for P_T^W and $\not{P}_T/$ of 20 GeV .

To see the effect of using a fixed value for the mass of the W the events were histogrammed using the proper M_W for each event and using the value of 80.345 GeV as the mass for all the events. The resulting histograms are shown in Figs. 4.3 on page 105 and 4.4 on the facing page. Looking carefully at Figs. (b) and (c) from 4.4 on the next page, it is obvious that many events that have a non-zero value when the proper M_W is used appear inside the bin for $\cos\theta^* = 0$. They are events for which the $P_{t(CS)}^{lepton} \leqq .5M_W^{fixed}$ and, as a result, give an imaginary solution to equation 4.40 on page 100. This implies that there are many real W events that are lost for the purpose of the analysis.

To be precise, many events are also "lost" due to the smearing effects of the detector. This constitutes a second source of errors and one that cannot be avoided. The histograms for the signal before and after smearing are presented in Fig. 4.4 on the next page.

The percentage error for the signal before and after smearing, as function of $\cos\theta^*$, was also calculated. The resulting histograms are shown in Fig. 4.5 on page 117 . The subfigures labeled (a) and (c) are representations of the relative error

$$re_{\cos(\theta^*)} = \frac{\cos(\theta^*)_{Real\ Mw\ smeared} - \cos(\theta^*)_{Real\ Mw\ NO\ smeared}}{\cos(\theta^*)_{Real\ Mw\ NO\ smeared}} \tag{4.60}$$

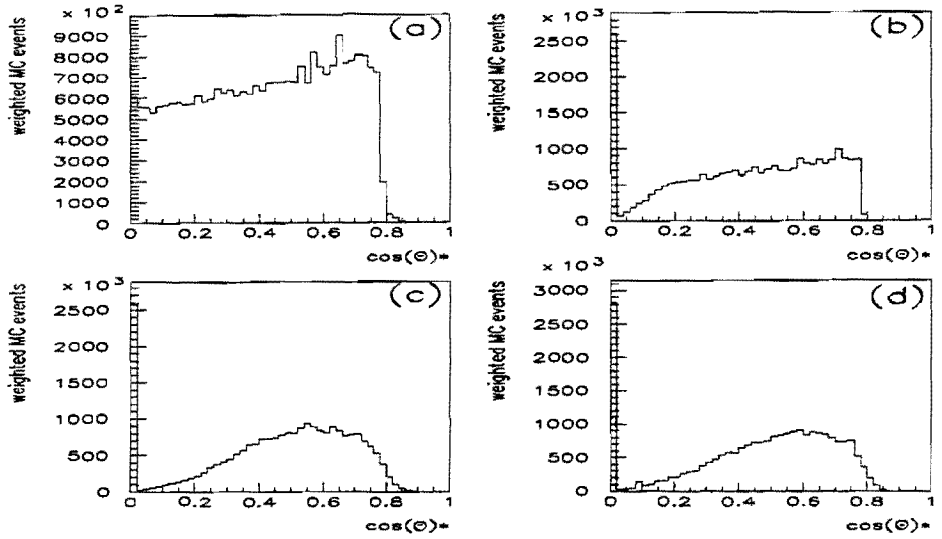

Figure 4.4: **Histograms showing MC generation of** $\frac{d\sigma}{d(\cos\theta^*)}$.
The following cases are shown:

a) the Mw for each event is known and no smearing applied

b) a fix value Mw = 80.345 is used, no smearing applied

c) same as (a) with the smearing effect of the detector applied

d) same as (b) with smearing.

and the subfigures (b) and (d) correspond to the case

$$re_{\cos(\theta^*)} = \frac{\cos(\theta^*)_{Fix\ MW\ smeared} - \cos(\theta^*)_{Real\ Mw\ NO\ smeared}}{\cos(\theta^*)_{Real\ Mw\ NO\ smeared}} \tag{4.61}$$

Subfigures (a) and (b) are two-dimensional histograms, while subfigures (c) and (d) are three-dimensional representations where the z-axis carries the information of the number of events. It is important to note that in all the figures the case for events with a $\cos(\theta^*)$ value below .01 has been

suppressed. This is for two reasons. First, the relative error at $\cos(\theta^*) = 0$ is ∞ . Second, all the imaginary values from expression 4.40 on page 100, as well as valid events with $\cos(\theta^*)$ equal to 0. are "dumped" on the same place, namely

$$\cos(\theta^*) = 0 \ , \ re_{\cos\theta} = -100 \quad .$$

Trying to picture these cases on the histograms will result in a loss of important detail.

Comparing the three-dimensional graphs of fig. 4.5 on the facing page (c) and (d) it is clear that a heavy toll is paid by trying to boost from the laboratory frame of reference to the Collins-Soper frame. Even though the smearing of data introduced by the detector is an important source of error, the major relative errors are introduced by the lack of knowledge about the z component of the $\not{P}_T$and, as a result, the need to choose a fixed value for the mass of the W boson. Furthermore, the interaction between data and detector can be modeled with relative accuracy, while the effect of the fixed W mass is not correlated to the available data, thus, it is impossible to model. With this in mind, it seems advantageous to look for another variable of the data which will allow us to carry out the analysis without the need of imposing any arbitrarily fixed parameter.

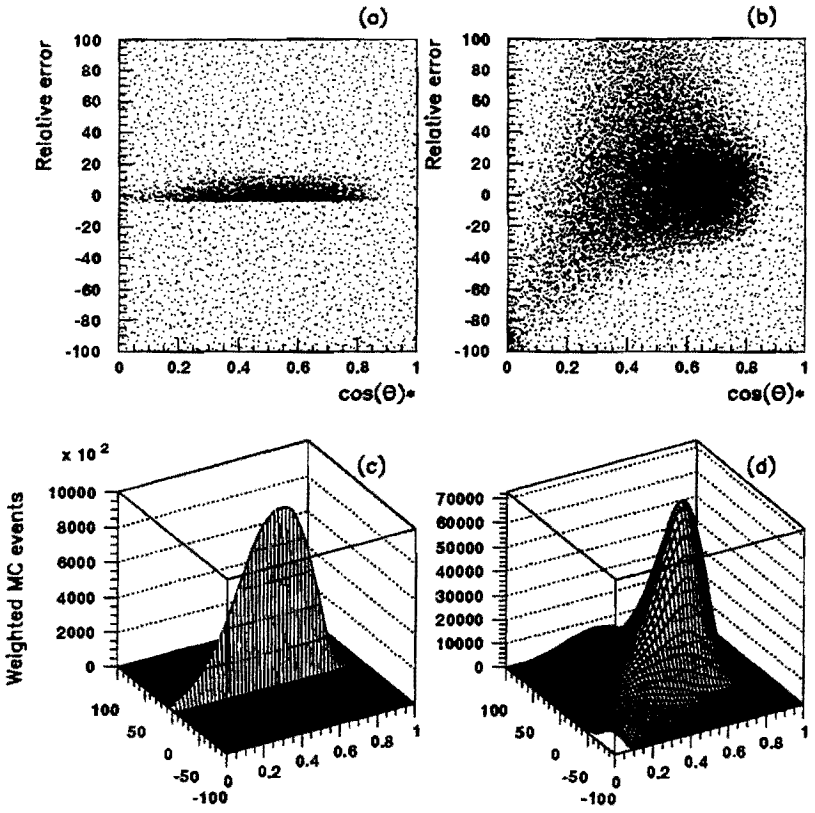

Figure 4.5: **Histograms showing relative errors.**

These errors are introduced by the smearing effect of the detector along ((a) and (c)) and by the usage of a fixed value for Mw and the smearing combined ((b) and (d)).

Chapter 5

Transverse Mass as $\mathcal{F}(\cos\theta^*)$

"So we find that not only such arts as sea-faring ...[ ]..., all were taught gradually by usage, and the active mind's experience as men groped their way forward step by step. So each particular development is brought gradually to the fore by the advance of time, and reason lifts it into the light of day. Men saw one notion after another take shape within their minds until by their arts they scaled the topmost peak. "

On the Nature of the Universe

Titus Lucretius Carus

5.1 Reviewing the Problem

As the previous chapter shows, it is possible to find the correct value of α_2 for the distribution

$$\frac{\partial\sigma}{\partial P_T^2\ \partial y\ \partial\cos\theta} = K_\theta(1 + \alpha_1\cos\theta^* + \alpha_2\cos^2\theta^*) \qquad (5.1)$$

going from the laboratory frame of reference to the Collins-Soper frame. Nevertheless, this approach involves the insertion of an "*arbitrary*" parameter; i.e., the mass of the W. In so doing the analysis is complicated by the introduction of two unwanted factors: a) the loss of valid events from the data, and b) the inherent errors resulting from the usage of a W mass different from it's correct value event by event. Both types of problems could be eliminated, at least in theory, if the present analysis could be done directly in the laboratory frame of reference. To be able to do so it is necessary to use an indirect measurement of α_2 . Several measurable variables of the process

$$p + \bar{p} \rightarrow W + X \qquad (5.2)$$

$$\rightarrow e^{\pm} + \nu_e + X \qquad (5.3)$$

could, in principle, be used. Of all the variables investigated the transverse mass of the boson (Mt^W) is the one selected.

Before the analysis can go any further it is imperative that a measurable dependence of Mt^W on $\cos\theta^*$ can be shown. The following sections are aimed to find if exists such dependency. The relations

$$Mt^W = \mathcal{F}(\cos\theta^*) \qquad (5.4)$$

and, more specifically,

$$\frac{\partial\sigma}{\partial(P_T^W)^2\ \partial Mt^W} = \mathcal{F}\left(\frac{\partial\sigma}{\partial(\mathrm{P_T^W})^2\ \partial\cos\theta^*}\right) \qquad (5.5)$$

and, as a consequence,

$$\frac{\partial\sigma}{\partial(P_T^W)^2\ \partial Mt^W} = \mathcal{F}((\mathrm{P_T^W})^2,\ \alpha_1,\ \alpha_2) \tag{5.6}$$

will be shown to exist using MC and analytical methods.

5.2 Analytical Expression of Mt^W as Function of $\cos\theta^*$

To show that the Transverse Mass distribution of the W-boson is P_T^W dependent and a function of $\cos\hat{\theta}$ it will suffice to be able to write

$$\frac{\partial\sigma}{\partial(P_T^W)^2\ \partial(Mt_W)}$$

explicitly and to make the appropriate changes of variables.

Let us rewrite this expression in the following manner

$$\frac{\partial\sigma}{\partial(P_T^W)^2\ \partial(Mt^W)} = \frac{\partial\sigma}{\partial(P_T^W)^2\ \partial(\cos\hat{\theta})} \times \frac{\partial(\cos\hat{\theta})}{\partial(Mt^W)}\ . \tag{5.7}$$

Recalling the expressions for the electron and neutrino in the Collins-Soper frame

$$e_{CS} = (e_{CS}^x\ ,\ e_{CS}^y\ ,\ e_{CS}^z\ ,\ i\frac{Mw}{2}) \tag{5.8}$$

$$\nu_{CS} = (-e_{CS}^x\ ,\ -e_{CS}^y\ ,\ -e_{CS}^z\ ,\ i\frac{Mw}{2}) \tag{5.9}$$

and rewriting them as functions of ϕ and $\hat{\theta}$, the following is obtained

$$e_{CS} = \frac{Mw}{2} \times (\cos\phi\sin\hat{\theta}\ ,\ \sin\phi\sin\hat{\theta}\ ,\ \cos\hat{\theta}\ ,\ i) \tag{5.10}$$

$$\nu_{CS} = \frac{Mw}{2} \times (-\cos\phi\sin\hat{\theta}\ ,\ -\sin\phi\sin\hat{\theta}\ ,\ -\cos\hat{\theta}\ ,\ i) \tag{5.11}$$

To obtain the Mt^W in the laboratory frame of reference in function of the above expressions for $\vec{e}_{CS}$ and $\vec{\nu}_{CS}$ it is sufficient to boost both leptons along the P_T^W to the rotated laboratory frame. This is so because the transverse mass of the W is invariant through both, a boost along W_z and a rotation around the same axis. The two dimensional vectors defined this way are:

$$\vec{v_e} = \frac{Mw}{2} \times (\frac{P_T^W}{Mw} + \sqrt{1 + (\frac{P_T^W}{Mw})^2}\cos\phi\sin\hat{\theta}\ ,\ \sin\phi\sin\hat{\theta}) \quad (5.12)$$

$$\vec{v_\nu} = \frac{Mw}{2} \times (\frac{P_T^W}{Mw} - \sqrt{1 + (\frac{P_T^W}{Mw})^2}\cos\phi\sin\hat{\theta}\ ,\ -\sin\phi\sin\hat{\theta}). \quad (5.13)$$

Now the transverse mass of W can be written as

$$Mt_W = \sqrt{2} \times \sqrt{\sqrt{(\vec{v_e}\bullet\vec{v_e})(\vec{v_\nu}\bullet\vec{v_\nu})} - (\vec{v_e}\bullet\vec{v_\nu})} \quad (5.14)$$

using the substitutions

$$\begin{aligned}\vec{v_e}^*\bullet\vec{v_e}^* &= \sin\theta^2 + \\ &2\,\frac{P_T^W}{Mw}\sqrt{1 + (\frac{P_T^W}{Mw})^2}\cos\phi\sin\hat{\theta} + \\ &(\frac{P_T^W}{Mw})^2(1 + \cos\phi^2\sin\hat{\theta}^2)\ ,\end{aligned} \quad (5.15)$$

$$\begin{aligned}\vec{v_\nu}^*\bullet\vec{v_\nu}^* &= \sin\hat{\theta}^2 + \\ &-\ 2\,\frac{P_T^W}{Mw}\sqrt{1 + (\frac{P_T^W}{Mw})^2}\cos\phi\sin\hat{\theta} + \\ &(\frac{P_T^W}{Mw})^2(1 + \cos\phi^2\sin\hat{\theta}^2)\ ,\end{aligned} \quad (5.16)$$

$$\begin{aligned}\vec{v_e}^*\bullet\vec{v_\nu}^* &= -\sin\hat{\theta}^2 + \\ &(\frac{P_T^W}{Mw})^2(1 - \cos\phi^2\sin\hat{\theta}^2)\end{aligned} \quad (5.17)$$

and

$$\vec{v_x}^* = \vec{v_x}\frac{1}{\frac{Mw}{2}} \tag{5.18}$$

Carrying out the substitutions and, after a little bit of algebra, the transverse mass of the W is written

$$Mt_W = \sqrt{2}\frac{Mw}{2} \times \sqrt{2\sqrt{a_0 + a_1(\frac{P_T^W}{Mw})^2 + a_2(\frac{P_T^W}{Mw})^4} - 2(-\sin\hat{\theta}^2 + (\frac{P_T^W}{Mw})^2(1 - \cos\phi^2\sin\hat{\theta}^2)} \tag{5.19}$$

,

where a_0, a_1 and a_2 are:

$$a_0 = \sin\hat{\theta}^4 \tag{5.20}$$

$$a_1 = 2\sin\hat{\theta}^2(\sin\phi^2 - \cos\phi^2\cos\hat{\theta}^2) \tag{5.21}$$

$$a_2 = (1 - \cos\phi^2\cos\hat{\theta}^2)^2 \tag{5.22}$$

This rendition of the transverse mass shows clearly that 5.4 on page 120 is a valid assumption. To show more specifically that 5.5 on page 120 is also valid it is necessary only to perform the partial differentiations. Unfortunately the expression obtained in 5.22 is too complicated to do it by brute force. Instead of differentiating 5.22 directly to obtain the explicit form of 5.4 on page 120 as function of $\cos\hat{\theta}$, an valid approximation can be achieved under simple assumptions.

To simplify the expression giving Mt^W a series expansion in powers of $\frac{P_T^W}{Mw}$ about the point $\{P_T^W = 0\}$ is generated and the first two terms are

kept. The Taylor series so constructed is

$$Mt_W(P_T^W, \phi, \cos\theta) = A_0 + A_2(\frac{P_T^W}{Mw})^2 + O\{(\frac{P_T^W}{Mw})^4\} \tag{5.23}$$

with

$$A_0 = \frac{Mw}{2} \times 2\sin\hat{\theta} \tag{5.24}$$

$$A_2 = \frac{Mw}{2} \times \cos\phi^2\left\{\sin\hat{\theta} - \frac{1}{\sin\hat{\theta}}\right\} \tag{5.25}$$

Furthermore, it is acceptable to assume that distribution 5.4 on page 120 is flat on ϕ . Integrating respect to ϕ

$$Mt_W(P_T^W, \cos\hat{\theta}) = \frac{1}{2\pi}\int_0^{2\pi} Mt_W(P_T^W, \phi, \cos\hat{\theta})d\phi \tag{5.26}$$

$$\frac{Mw}{2} \times (2 * \sin\hat{\theta} + \frac{1}{2}(\sin\hat{\theta} - \frac{1}{\sin\hat{\theta}})) \tag{5.27}$$

$$Mt_W(P_T^W, \cos\theta) = \frac{Mw}{2} \times 2\sin\hat{\theta} + \frac{Mw}{2} \times \frac{1}{2}\left\{\sin\hat{\theta} - \frac{1}{\sin\hat{\theta}}\right\}(\frac{P_T^W}{Mw})^2 \tag{5.28}$$

and from the last expression, differentiating respect to $\cos\hat{\theta}$

$$\frac{\partial}{\partial(\cos\hat{\theta})} \times Mt_W(P_T^W, \cos\theta) = + \frac{Mw}{2} \times \frac{\cos\hat{\theta}(4 + 2(\frac{P_T^W}{Mw})^2 - \cos\hat{\theta}^2(4 + (\frac{P_T^W}{Mw})^2))}{2(1 - cos\hat{\theta}^2)^{\frac{3}{2}}} \tag{5.29}$$

Inverting this, and multiplying by $\frac{\partial\sigma}{\partial(P_T^W)^2\ \partial(\cos\hat{\theta})}$ the final expression appears

$$\frac{\partial\sigma}{\partial(P_T^W)^2\partial(Mt^W)} = K^* \times (1 + \alpha_1\cos\hat{\theta} + \alpha_2\cos\hat{\theta}^2) \times \frac{2\sin\hat{\theta}^3}{\cos\hat{\theta}(4 + 2(\frac{P_T^W}{Mw})^2 - \cos\hat{\theta}^2(4 + (\frac{P_T^W}{Mw})^2))} \tag{5.30}$$

which presents the distribution of the transverse mass of the W as an explicit function of the parameters of interest.

It is fair to say that the dependence of $\frac{d\sigma}{d(Mt_W)}$ respect to α_i could be obtained directly from 5.7 on page 121 simply by substituting $\frac{\partial\sigma}{\partial(P_T^W)^2\ \partial(\cos\hat{\theta})}$ given in the first chapter. The exercise, besides providing an expression for the Mt^W distribution as function of only $\cos\hat{\theta}$ and P_T^W, shows that the α_i dependence is not destroyed when multiplied by $\frac{\partial(\cos\hat{\theta})}{\partial Mt^W}$.

5.3 Monte Carlo Analysis of Errors

In the previous chapter a study of the errors introduced in the $\frac{d\sigma}{dP_T^2\ dy\ d\cos\theta}$ was carried out and, as a consequence, the suggestion to use the transverse mass of the W to obtain the value of α_2 was made. The theoretical dependency of $\frac{d\sigma}{d(Mt_W)}$ respect to α_2 was proved in the previous section. It rests to show that there is an advantage in using this distribution instead of the original one.

At the same time that the $\cos\theta^*$ distributions were generated to study the effects of a fixed value of the mass of the W and the smearing due to the detector, the distributions for the transverse mass were also generated. In this case the total study is carried out in the laboratory frame of reference; thus, the analysis is free of the problems encountered before. Specifically, there are no "*lost events*" due to non-physical solutions to an expression (see for example 4.40 on page 100) required to boost the event from the laboratory frame to the CS frame. The errors, or distortions, introduced in

$$\frac{\partial\sigma}{\partial Mt^W}$$

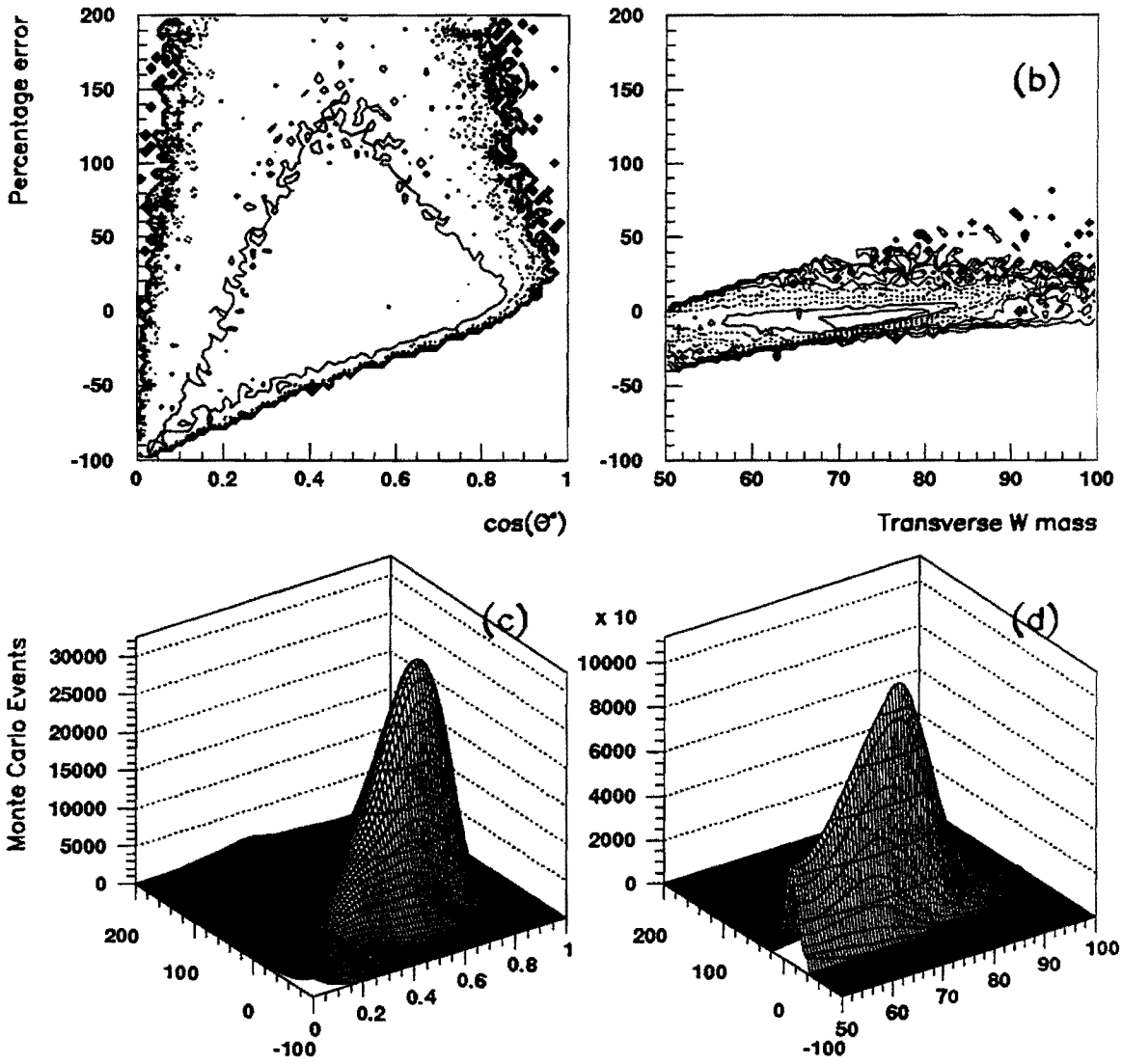

Figure 5.1: **Errors due to smearing.**

are caused solely by the interaction of the detector with the particles generated in the event. In order to see the errors introduced by the detector itself it is sufficient to compare the same MC distribution before and after the smearing process. This is equivalent to looking at the undistorted event (before smearing), and to the event as it appears to the experimentalist (after simulation of the DØ detector by smearing). The figures in 5.1 on the preceding page show these errors. The case of the $\cos\theta^*$ distribution is at the left and those for $\frac{d\sigma}{d(Mt_W)}$ are at the right. The two upper figures are contour graphs where each contour line corresponds to points with an equal number of Monte Carlo events. For these plots the vertical scale, spacing between iso-count lines, is in a logarithmic scale to better show the different behavior between the $\cos\theta^*$ and the Mt_W distributions. The plots on the bottom have lineal scales. It is easy to see that the errors introduced by the smearing effect of the detector are much smaller when the transverse mass of the boson is used.

5.4 Sensitivity Studies

Reviewing table 4.2 on page 90 of the previous chapter it seems that the value of α_2 should change from 1 to ≈ 0.03 for a $P_T^W \approx 80\ GeV$ and to ≈ -0.069 for P_T^W approaching 100 GeV. It will appear, then, that it should not be difficult to detect such a drastic change. Reality is sobering. The number of events with high P_T^W are not overabundant, as can be seen by looking at the P_T distribution of both Monte Carlo events and real data. Assuming that the statistics for high P_T are great, it is necessary to see to

what extent the $\frac{d\sigma}{d(Mt_W)}$ is sensitive to changes in the value of α_2 . Even if it is shown analytically that a given distribution is sensitive to variations of a parameter, "α_2 ", it is necessary to show that it is not masked or destroyed by other factors imprinting on the data. Three well known factors are capable of distorting the data to such an extent that the sensitivity to a parameter can be lost:

a) the mentioned lack of statistics, particularly for those events with high P_T^W for which the value of α_2 is far away from 1.

b) the smearing effects of the detector

c) the presence of background.

To minimize the effects mentioned in the second item of the list it is required to be able to model the detector's response very precisely. For the first element on the list only a wise choice of analysis-tools and obtaining more data, can help. For the third, a good understanding of the different backgrounds, as well as of their sources, coupled with discerning tools, will make a big difference.

The theme of the choice of tools, and the study of the backgrounds, will be developed later.

5.4.1 Sensitivity and Detector Smearing

The smearing effects of the detector need to be considered as the first step. Obviously, no matter how well the backgrounds are known and corrected for, or how much data is at hand, if the act of 'detecting' the data makes it

insensitive to the very effect (the α dependency) to be measured, then the work will be for nought. So, the first step is to show that it is possible to extract the effect of α_2 in $\frac{d\sigma}{d(Mt_W)}$ after the normal smearing.

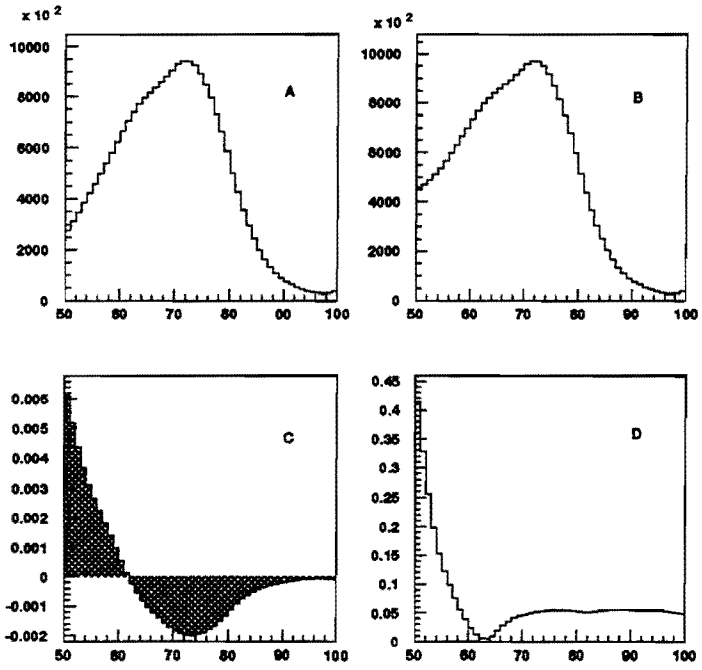

Figure 5.2: **Sensitivity studies. For all P_T^W.**

A) Transverse mass of W with $\alpha_2 = 1$. **B)** Transverse mass of W with $\alpha_2 = \mathcal{P}(\mathrm{P_T^W})$. **C)** B - A **D)** 2*(B - A)/(B + A)

Using the fast Monte Carlo 3,000,000 weighted events were generated with the standard weight

$$W_{electro-weak} = (1 \pm \cos\hat{\theta})^2$$

and, simultaneously, as many with weights α_2 dependent

$$W_{el+QCD} = (1 \pm \sqrt{\alpha_2} \times \cos\hat{\theta})^2$$

where the value of α_2 is given by the polynomial

$$\alpha_2 = 1 - 6.14E^{-4}q^2 + 9.395E^{-6}q^3 - 5.682E^{-8}q^4 + 1.451E^{-10} - 1.148E^{-13} , \tag{5.31}$$

with $q = P_T^W$, encountered in 4.1 on page 91 in the previous chapter. Note that the value of α_1 is set to $\pm 2 * \sqrt{\alpha_2}$. After smearing, the two distributions are normalized to one and the following distribution is obtained:

$$S(\alpha_i) = \frac{\mathcal{D}_{\text{el+QCD}} - \mathcal{D}_{\text{electro-weak}}}{.5(\mathcal{D}_{\text{el+QCD}} + \mathcal{D}_{\text{electro-weak}})} \tag{5.32}$$

where $\mathcal{D}$ is an abbreviation for $\partial\sigma/\partial Mt_W$ and $\int$ is a function measuring the sensitivity of the measurement to α_i . The histograms of these distributions are reproduced in figures 5.2 on the preceding page. They show that there is a change in the shape, albeit not as great as would be desired. Recalling 4.1 on page 91, the value of α_2 does not change very much for low ($\approx$ below 8. GeV) P_T^W . A better measure of the sensitivity of $\frac{d\sigma}{d(Mt_W)}$ is found when comparing the distributions for a range of the P_T^W where an appreciable change is expected. Repeating the process for the case when $P_T^W \geqq 25.0GeV$ the distributions shown on Fig. 5.3 on the facing page are obtained. Two things are noticeable:

- the differences between the two distributions are more obvious that in the previous case, and
- there is a strong change in the shapes of Fig. (A),(B) 5.2 on the page before and Fig. (2A),(2B) 5.3 on the facing page.

The second is the result of the strong dependency of $\partial\sigma/\partial Mt_W$ on the transverse momentum of the W, as it appears explicitly in the expression 5.30 on page 124 .

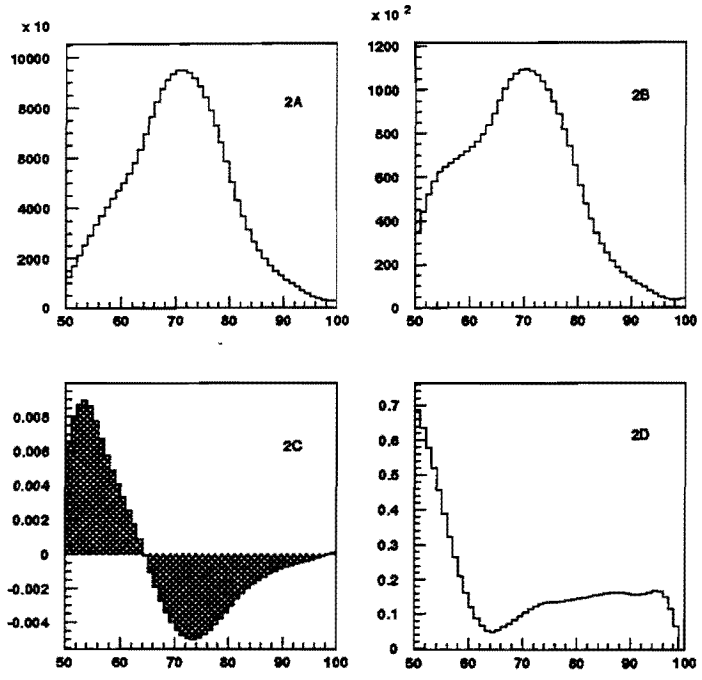

Figure 5.3: **Sensitivity studies. For** $20. \leq P_T^W \leq 200\ GeV$.

2A) Transverse mass of W with $\alpha_2 = 1$. **2B)** Transverse mass of W with $\alpha_2 = \mathcal{P}(P_T^W)$. **2C)** B - A **2D)** 2*(B - A)/(B + A)

Barring catastrophic effects, due to the modification of the shapes of the distributions by the backgrounds, Fig. (c) 5.3 suggests that it is possible to see the changes in $\partial\sigma/\partial Mt_W$ induced by the QCD effects.

5.4.2 Sensitivity and Backgrounds

An important cause of diminished sensitivity is the presence of background mixed with signal. The data obtained through the experiment is always a

mixture of signal and background, that is

$$Data = a \times Signal + b \times Background \tag{5.33}$$

or

$$Signal = \frac{Data - b \times Background}{a}$$

To extract the signal it is necessary to have a very good knowledge of the background unless b is so small that the background contribution is negligible. At this junction it is not possible to say. It is important, then, to have a rough idea of what kind of contamination of the signal will render it unsuitable to detect its dependence on α_2 . In three ways the background could interfere so much with the determination of α_2 as to make the task impossible:

◊ The percentage of background present in the data is very high. If the background is well understood and it is not strongly dependent on the parameter under consideration, the value of the parameter could be extracted. In this case, however, the errors in the parameter value could be so great that no conclusion can be reached.

◊ The background itself is strongly dependent on the parameter under study so that, even if the signals were independent of it, there is a false determination of the parameter under study.

◊ The background, although independent or weakly dependent on the parameter, has a shape that masks the behavior of the signal. If the shape of the background mimics the change in shape of the signal, and its percentage is relatively high, it will cast doubt on the determination of the parameter dependency of the signal.

P_T^W interval		a value	Percentage H BCK *
min GeV	max GeV		
0.	200	0.937338	$\approx$ 6.3
0.	4.9	0.971006	$\approx$ 2.9
4.9	7.3	0.949798	$\approx$ 5.0
7.3	17.5	0.905872	$\approx$ 9.4
17.5	200.0	0.802432	$\approx$ 19.8

Table 5.1: **Hypothetical Backgrounds**

(*) Minimum percentage of H. Background

If it is assumed that '*all* ' the differences between the '*data*' and the predicted '*signal*' by the electro-weak theory (no QCD influence) are due to the background, then it is possible to show that the shape of the background will be obtained by solving

$$\frac{Background}{[Background]} = \frac{1}{b} \times \left(\frac{Data}{[Data]} - a\,\frac{Signal}{[Signal]}\right) \qquad (5.34)$$

(where $[xx]$ is the area of the distribution xx) for **a** with the condition that $Background \geqq 0.$ for all values of Mt_W . The percentage of this assumed background is simply $100 * (1 - a)$.

The histograms reproduced in Fig. 5.4 on the following page show the shape of a hypothetical background that, assuming no α_2 dependence on the signal, will produce data that will, apparently, agree with Mirkes' theoretical calculations. Note that the percentage of contamination of the signal is

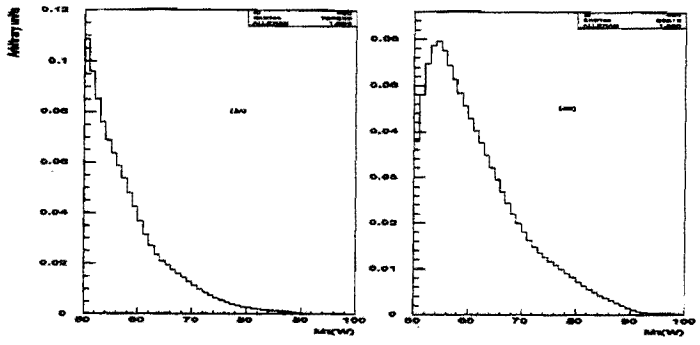

Figure 5.4: **Hypothetical Backgrounds**

3A) Hypothetical background to Mt_W for **all** P_T^W .

3B) Hypothetical background to Mt_W for $20. \leq P_T^W \leq 200\ GeV$.

within reasonable limits. The required percentages of these hypothetical backgrounds is presented in Table 5.1 on the page before.

It is important to emphasize that this is an exercise to show how relative 'innocuous' contamination can result in totally incorrect conclusions. The shapes and percentages obtained in this exercise have no relation to the real shapes and amounts of the background. A detailed analysis of the background is done in the next chapter.

Chapter 6

Analysis' Tools and Event Selection

> *Desist, therefore, from thrusting out reasoning from your mind because of its disconcerting novelty. Weigh it, rather, with discerning judgement. Then, if it seems to you true, give in. If it is false, gird yourself to oppose it. For the mind wants to discover by reasoning what exists in the infinity of space that lies out there,....*
>
> *On the Nature of the Universe*
>
> *Titus Lucretius Carus*

Within the previous pages both the justification for the present work as well as the generic tools used have been presented. The present chapter deals with the specifics of what data to use, how to select it, and what specific tools to use for the analysis of the data.

To begin, the choice of analytical tools will be presented.

6.1 Tools Selection

The interpretation of the results of any analysis cannot be done in a vacuum, rather it strongly depends on the tools used to reach it. The choice of tools should be justified by their suitability to the task, and by their logical treatment of the data. The experimentalist must choose carefully and furthermore, must have confidence in the choice he makes. The following subsections will address all these concerns, starting with the confidence issue.

6.1.1 Choice: Logical Probability

There are several things that have always made my intuition revolt against certain practices. For one, I never was able to accept the idea that an infinite magnitude will possibly have any meaning in the physical world other than an abstraction of the mathematical mind to deal with a situation where the limit of a process cannot be obtained by direct means. I felt, in some ways, like an inhabitant of a different planet until I came across the following statement by Gauss: "*I protest against the use of infinite magnitude as something accomplished, which is never permissible in mathematics. Infinity is merely a figure of speech, the true meaning being a limit.*". I have a similar problem when trying to follow the reasoning behind "orthodox" probability theory with all the paradoxes that it appears to engender. Interestingly enough, the prevailing idea that probability is a theory of *chance* denuded of logic is a late comer. The pillars of probability theory (Gauss, Laplace, etc.) look at it more as scientific inference that complies with the roles of

logic rather than the result of flipping coins. It is around the turn of the century when, under the influence of non-physicists, probability theory takes a turn moving away from the inference and logic principles and developing a series of "*recipes*" to deal with specific problems. One of the more, if not the most, influential members of the new "orthodox" approach is R. A. Fisher and his book *Statistical Methods for Research Workers* . It seems to me that many of the recipes, as appropriate as they might be to specific problems, obtain success not so much because of a sound approach, but because they drastically reduce the amount of computation required to obtain an answer. Perhaps the single thing that goes against my thinking is the difficulty, inherent in the orthodox view, of including *all* the knowledge available about a given problem in the interpretation of a given set of "*data*". For instance, why can I not include the knowledge that the value of α_2 is one (or very close to one) when the *Pt* of the W is zero (or very close to zero)? Better yet, why should one consider values for α_2 greater than one? Both premises came from accepting that the process $W \rightarrow e\nu$ follows the predictions of the accepted V-A theory of electroweak interactions.

I would like to rephrase the maxim "*Let the data speak for itself* " as "*Let* all the pertinent *data speak for itself*".

Bayes' theorem, when correctly interpreted and applied, eliminates the need for *ad hoc* recipes and anchors the concept of probability in the measurement of the degree of knowledge available regarding a given problem. It seems to be suitable for the task, but it needs to be expanded in scope. Its application should allow for inclusion of all knowledge of the problem, as well as elimination of unnecessary calculations of parameters not needed in the

interpretation of the data. Unfortunately, my knowledge of logic, statistics, inference, etc. is not as good as is required to be able to find the correct formula to include *all the pertinent* data in the analysis. Fortunately, better brains than mine have solved the problem. The way to a logical approach to probability theory, in particular as it applies to theory testing and parameter evaluation, is clearly explained by E. T. Jaynes in his work: *Probability Theory: The Logic of Science.* It is this approach to data interpretation that will be used in this thesis.

6.1.2 Logic Rules and Conventions

In this thesis a series of conventions and definitions is used regarding propositions and their relationships. Furthermore, '*probability*' is defined in the Bayesian mode. For convenience these are briefly presented below.

- ☐ A capital letter 'X' stands for a '*proposition*'.
- ☐ A barred capital letter '$\bar{X}$' stands for the negation (or opposite) of the proposition 'X'.
- ☐ Given two propositions 'A','B' then 'AB' stands for a new proposition 'C' defined as proposition 'A' *AND* proposition 'B'; i.e., 'C' is true only if 'A' and 'B' are both true.
- ☐ Given two propositions 'A','B' then 'A + B' stands for a new proposition 'C' defined as proposition 'A' *OR* proposition 'B'; i.e., 'C' is true if either 'A' or 'B' is true.

- In general, the truthfulness or falsehood of a proposition 'A' is dependent upon some assumptions or conditions described by some other proposition 'B'. This conditional is represented by '$A|B$' and reads 'A' *given*'B'.

- A real number, represented by '$g(A|B)$', is associated with the measurement of the *plausibility* of 'A' being true given 'B'.

- If '1' is associated with the certainty of the truth of '$A|B$', and '0' is associated to the certainty of the falsehood of '$A|B$', then '$g(A|B)$' is the '*probability*' of 'A' being true given 'B'. This definition of probability corresponds to the ideas developed by Laplace in his *Théorie Analytique des Probabilités.*

Using these conventions and definitions, a rigorous mathematical theory of probability and a mathematical language for inference is developed [50]. It is this approach to probability that is used in this work.

Rules of inference are presented here without demonstration of their validity.

To the well known rules of Boolean Algebra

$$A\bar{A} = 0 \tag{6.1}$$

$$A + \bar{A} = 1 \tag{6.2}$$

$$Identity \rightarrow \begin{cases} AA = A \\ A + A = A \end{cases} \tag{6.3}$$

$$Commutativity \rightarrow \begin{cases} AB & = BA \\ A + B & = B + A \end{cases} \tag{6.4}$$

$$Associativity \rightarrow \begin{cases} A + (B + C) & = (A + B) + C = A + B + C \\ A(BC) & = (AB)C = ABC \end{cases} \tag{6.5}$$

$$Distributivity \rightarrow \begin{cases} A(B + C) & = AB + AC \\ A + (BC) & = (A + B)(A + C) \end{cases} \tag{6.6}$$

$$Duality \rightarrow \begin{cases} If\ C = AB, & then\ \bar{C} = \bar{A} + \bar{B} \\ If\ C = A + B, & then\ \bar{C} = \bar{A}\bar{B} \end{cases} \tag{6.7}$$

the two following rules are added:

Product rule

$$P(AB|C) = P(A|BC)P(B|C) = P(B|AC)P(A|C) \tag{6.8}$$

Sum rule

$$P(A|B) + P(\bar{A}|B) = 1 \tag{6.9}$$

The Boolean Algebra is applied to the propositions at each side of the '|' symbol. Thus, if

$$\mathfrak{B}(\mathrm{A},\mathrm{B}) = C \tag{6.10}$$

$$\mathfrak{B}(\mathrm{X},\mathrm{Y}) = Z\ , \tag{6.11}$$

where $\mathfrak{B}$ is any Boolean expression, then

$$g(\mathfrak{B}(\mathrm{A},\mathrm{B}) \mid \mathfrak{B}(\mathrm{X},\mathrm{Y})) \;=\; \mathrm{g}(\mathrm{C}|\mathrm{Z}) \;\; . \tag{6.12}$$

From these the general sum rule

$$P(A \;+\; B|C) \;=\; P(A|C) \;+\; P(B|C) \;-\; P(AB|C) \tag{6.13}$$

is obtained.

Following Jaynes, the conventions used in this work are

- $g(A|B) \;\Rightarrow$ plausibility of A given B
- $P(A|B) \;\Rightarrow$ probability of A given B, with A and B being propositions
- $p(a|b) \;\Rightarrow$ probability with numerical values as arguments
- $p(a|B)$, $p(A|B)$ accepted loose notation for probabilities with mixed arguments.

From the product rule, assuming that propositions A,B and C are not mutually contradictory, Bayes' theorem

$$\begin{aligned} p(A|BC) \;&=\; p(A|C)\frac{p(B|AC)}{p(B|C)} \\ &=\; p(A|B)\frac{p(C|AB)}{p(C|B)} \end{aligned} \tag{6.14}$$

is obtained directly.

All other rules or relations between probabilities can be obtained by application of the preceding rules. Two very useful ones are presented below.

- Given a set $\{A_i\}$ of mutually exclusive propositions, then

$$p(\sum_{i=1}^{n} A_i|B) \;=\; \sum_{i=1}^{n} p(A_i|B) \tag{6.15}$$

and if the set is also exhaustive

$$\sum_{i=1}^{n} p(A_i|B) \;=\; 1 \tag{6.16}$$

- All parameters (prepositions) affecting the interpretation of the data need to be accounted for and included in the calculations. Nuisance parameters, that is, parameters affecting a hypotheses but whose values are of no interest, should be included in the calculations in such a way that their values do not need to be obtained. This is achieved by summing (integrating) their effects

$$\begin{aligned} p(a|D,I) \;&=\; \sum_i p(a,b_i|D,I) \\ &=\; \sum_i p(a|b_i,D,I)p(b|D,I) \end{aligned} \tag{6.17}$$

or

$$\begin{aligned} p(a|D,I) \;&=\; \int p(a,b|D,I)db \\ &=\; \int p(a|b,D,I)p(b|D,I)db \end{aligned} \tag{6.18}$$

6.2 Data collection

On April, 1992, the first run of DØ began. After approximately three months the Tevatron shut down for tuning and, shortly after that, DØ continued acquiring data for a period of 14 months. During this period (Run 1a) the total integrated luminosity was 31.1 $\text{pb}^{-1}$of which 16.7 $\pm$2.0 $\text{pb}^{-1}$was stored

on tape. The difference between the integrated luminosity delivered by the Tevatron and that stored by the DØ experiment is due to inefficiencies in the detector ($\approx$ 20%) and dead time due to the main ring veto ($\approx$ 25%) resulting in a total efficiency of about 60%. The main ring veto stops the detector from acquiring data at two times: at main ring injection time and when the beam in the main ring passes through the detector. The first veto takes place every 2.6 s (the main ring cycle time) for a period of 400 ms. The second veto lasts approximately 1.5 μs every collision or every 20 μs.

6.3 Data selection

The selection of events of interest starts with the choice of a set of triggers that allows us to store those events that will correspond more likely to the type of process under study. In our case we want events in which a W vector boson is created and which subsequently, decays in an electron e (following our convention an electron refers indistinctively to an e^+ or an e^-) and an electron-neutrino ν. The final state is thus characterized by the presence of an electron candidate and missing energy.

6.3.1 On line trigger selection

Of all the triggers available one in particular serves our purpose very well, namely the ELE_HIGH trigger. This trigger allows any event where there is at least an electron candidate with a minimum transverse energy of 20 GeV. to pass; i.e., to be written to tape. Note that ELE_HIGH, by definition, will pass events with and without transverse missing energy. The reason for

selecting this trigger is that it contains all detected Ws as well as all possible type background events, thus allowing us to deal with data and backgrounds using the same set of events. During run 1A, 111,361 events from this trigger were written on tape.

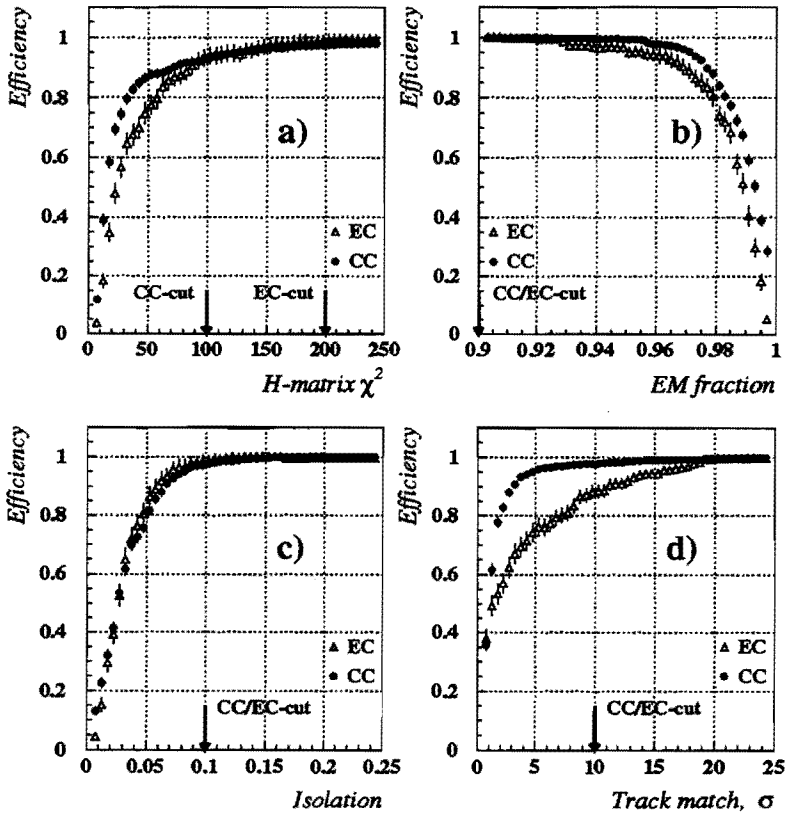

Figure 6.1: **Efficiency curves.**

- The Central Calorimeter (CC).

△ The End Caps of the Calorimeter (EC).

In order to select the most likely W candidates and reject background

events, a series of restrictions on all events selected by the ELE_HIGH, is implemented. These constitute the "Off Line Event Selection".

6.3.2 Off Line Event Selection

The ELE_HIGH trigger allows not only W events to pass, but also any event characterized by including an electron-like particle with, at least, 20. GeV. Events such as $Z \rightarrow e^+ + e^-$ or $X \rightarrow e_{like} + \textit{anything}$ are present in the ELE_HIGH set. A judicial selection of constraints imposed upon the set should allow the majority of the events corresponding to true W to pass at the same time that it blocks the passage of other types of events. In other words, it is necessary to define a series of cuts highly efficient for W and with a high rejection ratio for other processes.

Members of the DØ collaboration have paid particular attention to the problem of defining an optimal set of cuts for Ws. Furthermore, every person involved in data analysis has, by necessity, investigated different ways of dealing with the problem. As part of this work, a study of the effects of different cuts was done.

- E_{MF} electromagnetic fraction of the e-like particle
- χ^2 reflecting the shower shape
- f_{iso} isolation factor
- σ_{trk} number of tracks matching the e-like trajectory in the tracking detector

- $\frac{dE}{dx}$ energy lost per unit length by the particle in its path through the CDC and *and\or* TRC

The definition of these variables is in the chapter dealing with particle identification.

The following table presents the mentioned cuts and the corresponding efficiencies:

. . . . .	CC		EC	
CUT	**Value**	ϵ	**Value**	ϵ
χ^2	$\leq$ 100	0.949 $\pm$ 0.008	$\leq$ 200	0.953 $\pm$ 0.024
f_{iso}	$\leq$ 0.1	0.976 $\pm$ 0.006	$\leq$ 0.1	0.985 $\pm$ 0.013
σ_{trk}	$\leq$ 10	0.980 $\pm$ 0.006	$\leq$ 10	0.915 $\pm$ 0.023
All cuts		0.913 $\pm$ 0.011		0.861 $\pm$ 0.03
$\frac{dE}{dx}$		0.861 $\pm$ 0.014		0.580 $\pm$ 0.033
All cuts		0.847 $\pm$ 0.015		0.572 $\pm$ 0.032
E_{MF}	$\geq$ 0.90	0.995 $\pm$ 0.005	$\geq$ 0.90	0.995 $\pm$ 0.005
All cuts		0.842 $\pm$ 0.016		0.569 $\pm$ 0.033

Table 6.1: **Cuts cutoff values and their efficiencies.**

where the efficiency for a particular cut is given by

$$\epsilon_{cut} = \frac{\epsilon_p - \epsilon_c f_b}{1 - f_b} \quad . \tag{6.19}$$

In this expression f_b is the background fraction and ϵ_p and ϵ_c are the fraction of electrons passing the cut in the "*parent* " and "*control*" samples [46]. The errors are obtained by adding in quadrature statistical and systematic errors.

The efficiencies for the first four variables on the preceding list are presented in figure 6.1 on page 144. The vertical arrows show the values used as '*Electron Quality Cuts* '. Note that the efficiency curves for the Central Calorimeter have a faster rise, as well as a flatter plateau, than the ones for the EC. This behavior is particularly accentuated for the track matching function. This fact, coupled with the greater difficulty of modeling correctly the EC response, will steer the present analysis to be limited to events whose electron is fully contained in the CC.

To obtain the efficiencies an estimation of the total background is required. In the next chapter a study of the different backgrounds is presented in detail.

6.4 Selection Cuts

- Fiducial cuts
  - $|e_\eta| \leq 1.1$
  - $1.5 \leq |e_\eta| \leq 2.6$
- Kinematic cuts
  - $P_T^E \leq 20.$ GeV
  - $\not\!\!E_T \leq 20.$ GeV when appropriate
  - $P_T^W \leq 200.$ GeV
  - $M_T^W \geq 100.$ GeV

and

- Electron Quality cuts
  - $\chi^2 \leq 100$ or $\chi^2 \geq 150$
  - $f_iso \leq 0.4$
  - $em_{frac} \geq .9$

These cuts are not the final cuts used in the α_2 determination. These are the general cuts used to do the study on backgrounds.

Chapter 7

Backgrounds

It is clear, then, that the person who speculates begins with a great many things that are all mixed up, from which he continually sifts nine out of ten, and then eight of nine, and then [...

...]. Should he hold on to what he has accomplished, there is hope that he may come back to it and complete the process. If, however, he does not retain it, then he would be compelled to repeat the entire process of reasoning from the beginning.

The Book of Beliefs and Opinions

Saadia Gaon

7.1 Identification of Backgrounds

Contamination of the $W \rightarrow e + \nu$ sample occurs by any process that results in a single electron and missing transverse energy as seen by the detector.

These events create a background that distorts the real data and, therefore, should be taken into account in any analysis. Depending on the source, the background is divided into two types:

1. background due to physical processes which mimic a true $W \rightarrow e + \nu + X$, or created by well understood interactions resulting in a real electron and missing transverse energy that are misinterpreted by the detector as $W \rightarrow e + \nu$ decays. Because these types of background are well understood, I will refer to them as "Known Backgrounds".

2. blind areas and erroneous responses in the detector can create situations where a W-like signature is generated where no W is present. This type of background is addressed as QCD Background.

7.1.1 Known Backgrounds

Of all the possible physical backgrounds, the most important and the best understood is generated when a W decays to a $\tau + \nu$ and the tau subsequently decays to an electron and two neutrinos. This cascade process produces the same signature as the leptonic decay of the W to electron plus neutrino; i.e., an electron and missing transverse energy. Because the branching ratio of the W to tau decay is the same as that of the W to electron, the percentage of the tau background could be as high as 17.93 branching ratio of $\tau \rightarrow e + \nu + \nu$. One way to decrease the effect of this background is to impose a higher Pt requirement on the electron. This kinematic cut is effective because the electron produced from a secondary decay will be smaller than the Pt of an electron generated from a direct decay of the same

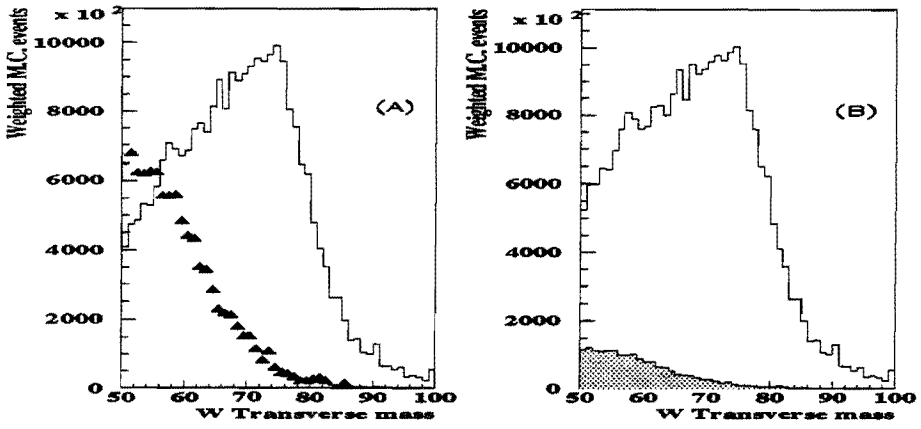

Figure 7.1: τ **background study.**

- The histograms of (A) are:
  1. Continuous line $\rightarrow$ $W \rightarrow e\nu$
  2. Filled triangles $\rightarrow$ $W \rightarrow \tau\nu \rightarrow e\nu\nu\nu$
- The histograms of (B) are:
  1. Continuous line $\rightarrow$ signal plus τ background
  2. Filled histogram τ background

W. To truly assess the impact of the tau background in the measurement of the angular distribution of the electron from $W \rightarrow e + \nu$, a series of Monte Carlo simulations was made.

Studies of the Monte Carlo distributions show that these events modify the lower end of the transverse mass spectrum and the upper end of the $\cos(\theta^*)$ distribution. These Monte Carlo studies are presented in figure 7.1.1. Part (A) of the figure gives the transverse mass of the W for the case

$$W \rightarrow \tau + \nu \rightarrow e + \nu + \nu + \nu ,$$

part (B) is the transverse mass of the W from the leptonic decay through the e

channel to which the proper amount of contamination from the tau channel has been added. The hashed part of (B) is the amount of τ background properly scaled. Two things are to be emphasized here:

- this type of background strongly modifies the shape of the distributions under study and,
- the modeling of this background is as well understood as the modeling of the signal.

Initial State		**Intermediate**		**Final State**	
Gen.	Cross Section		Branching Ratio		Branching Ratio
W		$\tau\,\nu$		$e + 3\nu$	
Z		$\tau\,\tau$	3.4	$e + n\nu + m.jets$	15.

Table 7.1: **Processes giving a W signature.**

Other events that could produce an erroneous signature corresponding to a W are far less important. Table 7.1.1 is a non-exhaustive list of known backgrounds.

Besides the abovementioned tau background, the other important source comes from Z decays when an electron passes through the detector undetected (eg. goes through the calorimeter cracks). These events will mimic a W. The background due to Z decays is expected to be quite low. Although Monte Carlo studies show that the total percentage of background from Zs is 0.7 $\pm$ 0.5%, its shape is shown in 7.2 on the facing page for completeness.

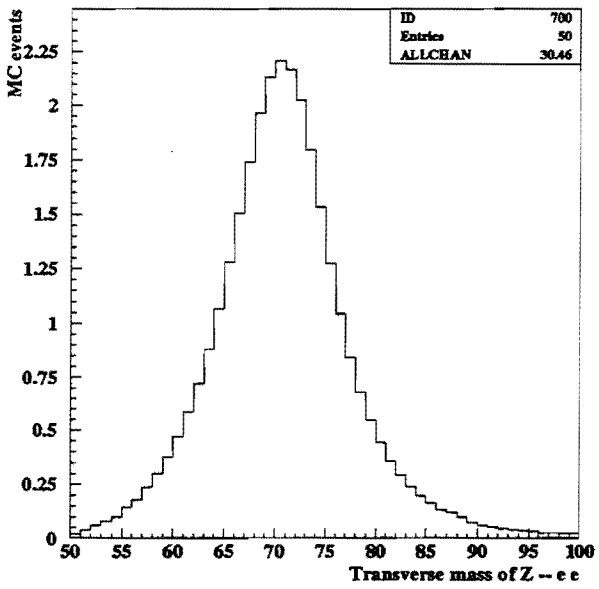

Figure 7.2: **Z $\rightarrow$ e e background study.**

This type of background affects the middle of the transverse mass spectrum of the W.

7.1.2 QCD Background

Any process whose final state does not include an electron, nor missing transverse energy, but that is interpreted as such by the detector, constitutes a source of background. We can visualize an event whose final state consists of several objects, none of which is an electron. If one or more objects is lost through cracks in the detector, or its energy is underestimated, the detector gives a missing transverse energy. If one of the remaining objects is misinterpreted as an electron, the result is an event with the same signature as $W \rightarrow e + \nu$. In a typical situation a hadronic jet formed by one or more

π^0s overlapping a soft charged particle will produce a track (by the charged particle) which points to an electromagnetic shower in the calorimeter (from the π^0s). Thus, an electron signature appears. This fake electron, combined with the apparent missing Pt, produces a signature almost impossible to distinguish from a real W leptonic decay to $e + \nu$.

The dominant source of fake electrons with apparent missing Pt is QCD multijets production, thus the name QCD Background.

Although the probability of misreading a hadronic jet as an electron, combined with the probability of losing a considerable amount of energy from the event is low, it is far from negligible. When this probability is multiplied by the total cross-section of all possible events that can give such fakes Ws, the expected amount of QCD Background is anything but small. For instance, the inclusive jet cross section of events with at least one jet with $Pt > 25\ GeV$ is more than three orders of magnitude greater than the $W \rightarrow e + \nu$ cross section. This and the fact that there is not a good model for the behavior of the detector that creates fake Ws, make the study of the QCD Background a particularly difficult task.

Once the backgrounds and their sources are identified it is necessary to know two things:

- the amount (percentage) of background expected in the signal, and

- the particular "shape" of the background.

7.2 Expectancy of Known Backgrounds

Both the percentage of the "Known Backgrounds" (KB) and their shapes are obtained directly from the Monte Carlo simulations. Because the MC simulations for the interesting data and the KB use the same analytical techniques, it is possible, and desirable, to include the effects of these backgrounds in the MC. Because the only important contribution in this category is the background due to the $W \rightarrow \tau + \nu$, the approach is straightforward. At the event generation level in the Monte Carlo, as many Ws decaying to tau as Ws decaying to electron are generated. Afterwards, the τ is forced to decay to one electron plus two neutrinos. The events generated this way are then given the appropriate weight so their total contribution is only 17.93% of the original. The resulting events have a final state form of one electron and missing energy. These events are treated, from now on, in exactly the same manner as the events originated from $W \rightarrow e + \nu$. The resulting distributions contain the data events mixed with the appropriate percentage of tau events. Thus, the distributions are already modified in the proper manner by the important Known Background.

It is straight forward to calculate the percentage of τ background from the distributions shown in Fig. 7.1.1 on page 151 . The total number of events from the $W \rightarrow e + \nu$ present in the histogram (B) of the afore-mentioned figure is 27,201,388, of which 25,462,018 are from the direct decay of the W to electrons and the rest are from Ws that decayed to τ . The percentage of

τ induced background is then

$$\begin{aligned} \% \, \tau_{BCK} &= 100 \times \frac{27201388 - 25462018}{27201388} \\ &= 6.39 \ ; \end{aligned} \tag{7.1}$$

a considerable amount. The value of this percentage is strongly dependent on the cuts made in the transverse mass distribution as can be directly inferred from the distributions shown.

7.3 Expectancy of QCD Background

The study of the QCD Background is far more complicated. Indeed, there still does not exist a good way to model all the idiosyncracies of the DØ detector that will contribute to the mislabeling of jets as electrons. Nor is there a detailed geometrical description of the detector that takes into account all the possible blind spots. Even if such a perfect geometrical description of the detector were available, the amount of computer power required to run QCD background studies with sufficient statistics is totally prohibitive. The study of this type of contamination of the data is done using preferential analysis techniques of the data itself. Because of the importance of the background for the analysis presented here, it is necessary to have a good knowledge of the way its parameterization is obtained.

7.3.1 Expected Amount of QCD Background

Several techniques used to obtain an estimation of the expected percentage of QCD Background have been developed by people in the DØ collaboration. Of

those, two are presented here. The first is accepted across the collaboration, but it fails in some instances as the study of the procedure will show. The second was developed by the author in the scope of the work presented here and will be described after the study of the shape of the QCD background is done.

Let us consider two facts: the known behavior of the DØ detector, specifically of the calorimeter, and the typical process involved in the generation of a W and its consequent leptonic decay. The expected signature of the W is the presence of a fair amount of missing transverse energy. On the other hand, the behavior of the calorimeter assures that the amount of missing transverse energy created by an imperfect balance of the energies present in one event is small. These two facts justify making the following assumption:

Events with very low $\not\!\!E_T$ have a high probability of being QCD events.

Using this assumption, the calculation of the percentage of QCD Background expected to contaminate the W sample process is as follows:

- Select an inclusive sample of events that have a W. A suitable sample is one obtained using the ELE_HIGH trigger. This trigger selects events which have at least one electron with a $P_T \geq 20$ GeV. Thus, all possible Ws, plus any event whose final state has at least one electron with the prescribed P_T are included in the sample.

- Impose a set of general fiducial cuts to define the regions of the detector of interest. In this case two sets are used:

  - $|\eta| \leq 1.1$ a conservative cut imposed on the primary electron of the event to assure that it is "central"; i.e., it is fully contained in

the central part of the calorimeter (CC).

- $1.5 \leq |\eta \leq 3.1$ to select events whose primary electron is fully contained within the end-caps of the calorimeter (ECS and ECN).

■ Good electron sample.

Select the most likely W events by imposing a set of tight constraints on the quality of the electrons. These tight cuts are:

- $\chi^2 \leq 100$; the electromagnetic object tagged as an electron has a χ^2 corresponding to a high probability for a real electron.
- EM Fraction ≥ 0.90 ; the higher the EMF of jet the more likely that it is a real electron.
- $ISO \leq .15$; attempt to eliminate π^0s from the sample.
- $1 \geq TRACKs \leq 5$; in theory an isolated electron will have a single track in the central (or forward) tracking detectors.

■ Bad electron sample.

Impose a series of cuts so that the likelihood of an object passing the cuts and being a true electron is very low. These anti-electron cuts are:

- $\chi^2 > 150$
- EM Fraction < 0.90
- $TRACKs > 5$

Note that no ISOlation or $\frac{dx}{dE}$ is imposed.

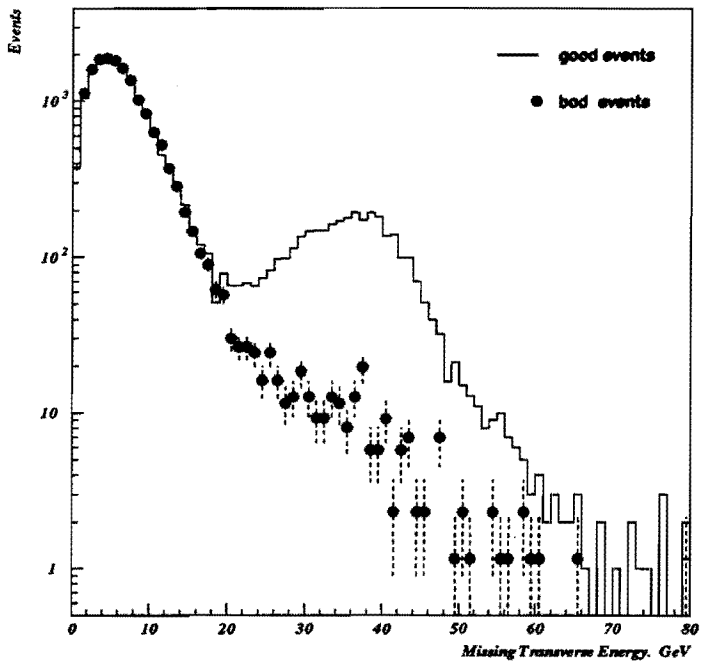

Figure 7.3: **Normalization of "Good" and "Bad" distributions.**
$\not\!\!P_T$ distributions for (a) "GOOD" events and (c) "BAD" events selected from the ELE_HIGH L1 trigger

- Select from the $\not\!\!P_T$ distributions of good and bad electrons those events with $1. \leq \not\!\!P_T \leq 11.$ GeV, and normalize the bad distribution so the total counts in the prescribed set of $\not\!\!P_T$ is equal to the number of good events in the same $\not\!\!P_T$ range. Figure 7.3 shows the $\not\!\!P_T$ spectra of "good" and "bad" electrons after normalization. It is clear that the spectrum of good electrons clearly preserves the Jacobian peak due to the Ws as expected. On the other hand, in the spectrum generated by the fake electrons the corresponding peak is almost non-existent.

- Once the normalization factor is obtained the next step is to impose

on both spectra of interest, in our case the M_T^W, the same kinematic cuts that are used to define the W sample:

- Electron ..... $P_T \geq 25$ GeV
- Missing transverse energy $\not{P}_T \geq 25$ GeV

The percentage P_{QCD} of expected QCD Background is then obtained using the expression

$$P_{QCD} = 100 \frac{\int_{v1}^{v2} BAD(v) \times N_F \, d(v)}{\int_{v1}^{v2} (GOOD(v) + BAD(v) \times N_F) \, d(v)}. \tag{7.2}$$

where N_F is the normalizing factor above described, GOOD(v) and BAD(v) are the corresponding spectra for the parameter v and v_1, v_2 are the lower and upper boundaries defining the interval of the parameter used.

Normally, after these calculations, the process ends. However, for this analysis it is necessary to go one step further.

- Because this study of the M_T^W spectra is done for different ranges of the P_T^W, the same applies to the QCD Background. The percentage of QCD interference P_{QCD}^{qr} is obtained by

$$P_{QCD}^{qr} = 100 \frac{\int_{mt1}^{mt2} BAD^{qr}(M_T^W) \times N_F \, d(M_T^W)}{\int_{mt1}^{mt2} (GOOD^{qr}(M_T^W) + BAD^{qr}(M_T^W) \times N_F) \, d(M_T^W)} \tag{7.3}$$

Where **qr** represents the P_T^W range.

The method used to obtain the percentage of expected QCD background has been developed further to accomodate the needs of the present work. The results of this analysis are presented in Table 7.2 .

	Central Region			
P_T^W range	Good Events	Bad Events	Norm. Factor	% QCD BCK
ALL	11714	167983	0.0697332	$3.8 \pm .1$
0.0 to 4.3	0	0	n/a	n/a
4.3 to 7.9	0	1	n/a	n/a
7.9 to 17.5	5	164	0.0304878	$1.8 \pm .4$
17.5 to 30.0	9524	134197	0.0709703	$7.2 \pm .62$

Table 7.2: **Estimated QCD Background**

Note that the percentage of QCD background cannot be calculated for the cases where the upper value of the P_t^W, used in the definition of the P_t^W range, is below 7.9 GeV. This problem arises because, with the cuts used to define 'good' and 'bad', there are no events with a $\not\!\!P_t$ below 10 GeV . This is clearly shown in figure 7.4 on the following page. A way to get around the problem is to change the cuts used to define the 'Good' and 'Bad' samples as is done to obtain table 7.3 on page 163. But this approach does not assure that the numbers obtained are a good representation of the real situation. A far better approach is to make the assumption that the percentage of QCD background is a monotonic function of the P_t^W .

The scatter plots presented in figure 7.4 on the following page show that for $P_t^W \geq 10.0$ GeV there is one or more 'good' and 'bad' events whose $\not\!\!P_t$ is below 10 GeV . Selecting a suitable P_t^W range it is possible to find the expected percentage of QCD background for this range as long as its lower

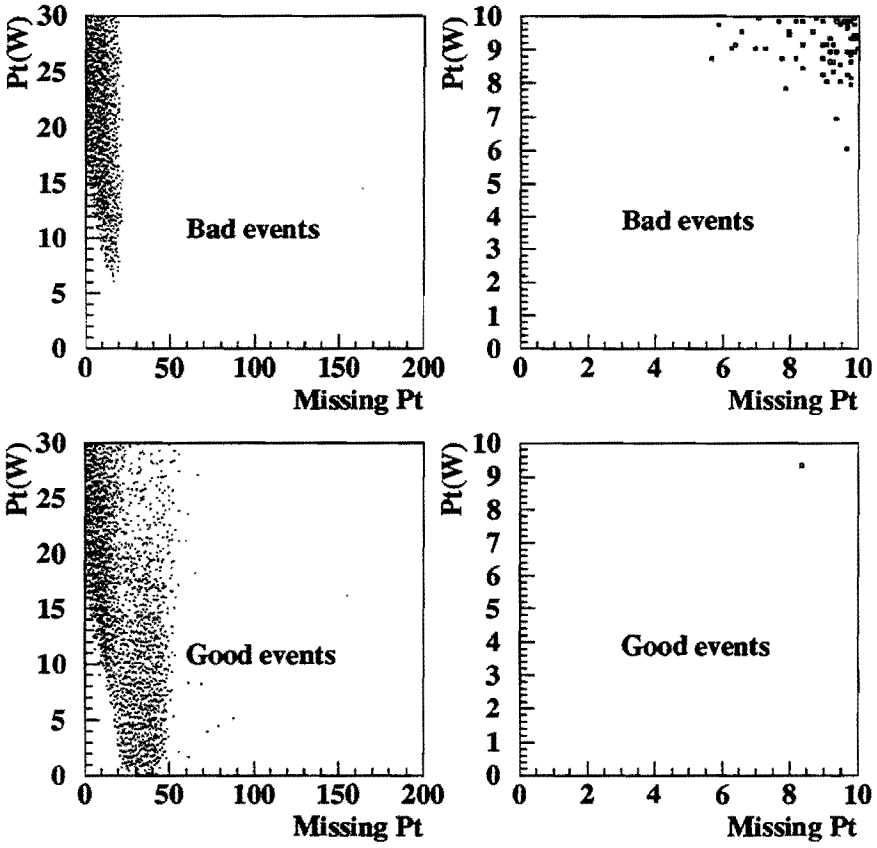

Figure 7.4: **Bad and Good Events.**

The plots on the right side are zooming in the lower left corner of the plots on the left.

limit of the P_t^W is $\geq$ 10.0 GeV. The following ranges are used:

$$[\Re_i, ...] = [\{5.0, 16.0\}, \{6, 17\}, \ ... \ \{19.0, 30.0\}] \ . \tag{7.4}$$

For each range the expected QCD background, its error and the weighted P_t^W average is calculated. The 15 points [P_t^W, % BCK] are fitted to a function of the type $\exp(a_0 + a_1 * x)$ and this function is used to extrapolate the expected values of the QCD background for low values of P_t^W. The errors

	Central Region				End Caps Region			
P_T^W range	Good Events	Bad Events	Norm. Factor	% QCD BCK	Good Events	Bad Events	Norm. Factor	% QCD BCK
ALL	30361	268962	0.112882	$4.7 \pm .1$	13623	102958	0.132316	$9.07 \pm .9$
0.0 to 4.3	27	76	0.355263	6.5 ± 1.8	14	59	0.237288	4.3 ± 1.3
4.3 to 7.9	107	516	0.207364	4.1 ± 0.6	81	478	0.169456	7.8 ± 1.4
7.9 to 17.5	7600	50180	0.151455	$4.9 \pm .4$	4944	31513	0.156888	9.5 ± 1.6
17.5 to 200.0	22627	218190	0.103703	$15.0 \pm .62$	8584	70908	0.121058	22.5 ± 4.5

Table 7.3: **Estimated QCD Background with loose cuts.**

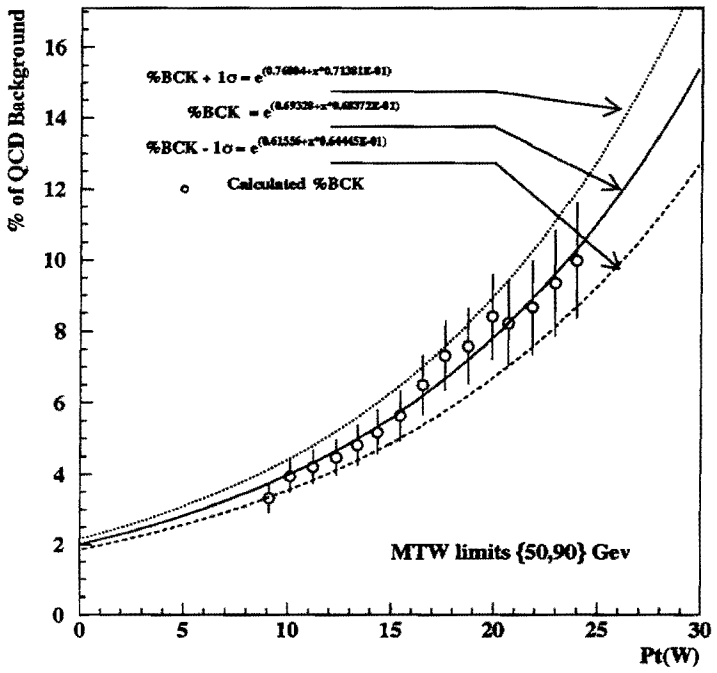

Figure 7.5: **Percentage of QCD Background as function of P_t^W .**

The $\pm 1\sigma$ lines are obtained by fitting the $\%QCD\ BCK\ \pm 1\sigma$ respectively.

are obtained in similar fashion by fitting the points [P_t^W, % BCK $-$ err] and [P_t^W, % BCK $+$ err]. The results of this procedure, in the case where the transverse mass of the W is constrained to between 50.0 GeV and 90.0 GeV , are presented in figure 7.5 on the page before this one. The exponential functions for the central values of the calculated % BCK , as well as those for the % BCK $\pm 1\sigma$, are shown. This exercise is repeated for different

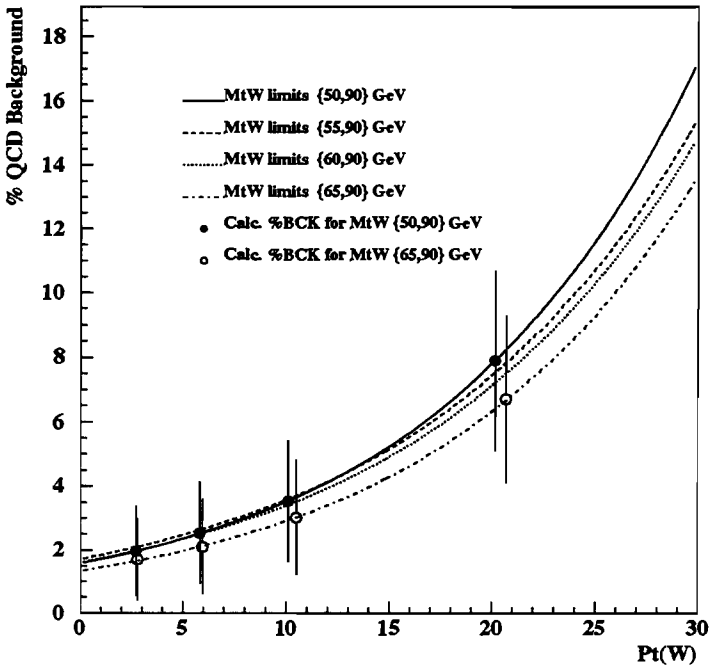

Figure 7.6: QCD Background as function of P_t^W .

The four lines correspond to the central values for four limits of the Mt(W).

The full and open circles show the expected percentage of QCD background.

limits imposed on the transverse mass of the W . By fixing the upper limit of M_T^W at 90.0 GeV , four different lower limits are used to create the following

M_T^W ranges:

$$\{\ 50.0,\ 90.0\}\ ,\ \{\ 55.0,\ 90.0\}\ ,\ \{\ 60.0,\ 90.0\}\ ,\ \{\ 65.0,\ 90.0\}\ .$$

With these results at hand, a new partition of the data in four P_t^W ranges, with an approximately equal number of events in each, is generated, the corresponding weighted P_t^W average is calculated and the expected percentage of QCD background is obtained using the functions previously obtained. A comparison of the results for the four M_T^W ranges is presented in figure 7.6 on the facing page . Numerical results for the two extreme cases are shown in table 7.4.

Transverse Mass Intervale $50.0 \leq M_T^W \leq 90.0$ GeV					**Transverse Mass Intervale** $65.0 \leq M_T^W \leq 90.0$ GeV				
P_T^W			Number	Percent.	P_T^W			Number	Percent.
Min.	Max.	Aver.	events	QCD BCK	Min.	Max.	Aver.	events	QCD BCK
0.00	4.30	2.72	740	1.97 ± 1.4	0.00	4.40	2.78	530	1.67 ± 1.3
4.30	7.50	5.84	746	2.53 ± 1.6	4.40	7.60	5.98	527	2.13 ± 1.5
7.50	13.35	10.10	741	3.54 ± 1.9	7.60	14.05	10.49	529	3.02 ± 1.7
13.35	30.00	20.17	722	7.89 ± 2.8	14.05	30.00	20.70	522	6.66 ± 2.6

Table 7.4: **Calculated QCD Backgrounds.**
Only the study for the CC is presented here.

The small differences in the P_T^W ranges and averages for the two cases presented are due to the small changes in the P_T^W spectrum imposed by the constraints in the transverse mass of the W.

In general, the study of the effects of the QCD Background ends once the percentage of contamination is obtained. In our case it is not enough to

have an understanding of the amount of background mixed with the signal. A knowledge, as good as possible, of the shape of these backgrounds is also needed. Hence, one more study is required.

7.3.2 Shape of QCD Background

There are no well-established techniques to determine the shape of the QCD Background. This is particularly true when these shapes are needed for small ranges of data as in this case. The task at hand is, thus, two fold:

- to develop a sound method of generating distributions that mimic the QCD Background
- and to apply said method to the problem at hand.

Several methods have been tried. Two of them are used, one way or another, in this work and their descriptions follow. The first method was developed by other members of the DØ collaboration.

7.3.2.1 Direct Method

This is an extension of the method used to obtain the percentage of QCD Background expected as described in the previous section. The same people responsible for the procedure to quantify the QCD contamination deserve credit here. In the last step of the procedure, to obtain the percentages of the QCD Background, histograms corresponding to the BAD electrons for the different transverse momenta of the W were obtained. These histograms, by definition, correspond to the QCD Background distributions to be expected in each P_T^W range used. Unfortunately, the statistics as shown in Fig 7.7 on the facing page are so poor that little information about the shapes of

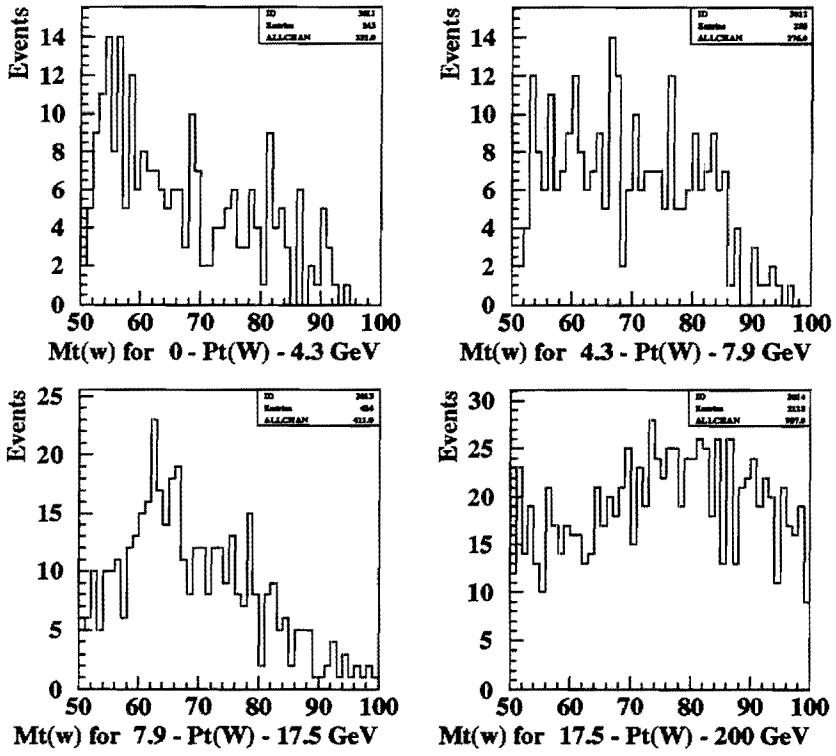

Figure 7.7: **QCD background study.**

these distributions can be inferred. This method can be applied, with some degree of confidence, only to the case where *all* the data is used in a single histogram; i.e., no separation into different P_T^W ranges is made. In this case the statistics are sufficient to show some general trends. In particular, a comparison between the upper and lower histograms of figure 7.8 on the next page indicates that the QCD background is an exponential decaying function of the transverse mass (upper part of the figure) modified by the turn-on functions of the cuts applied (lower part of the figure). These functions were presented in the previous chapter in figures 6.1 on page 144. Comparing the

histograms obtained for the Central Calorimeter and the End Caps, again using figure 7.8, it is clear that the situation is worse for the case of the End Caps. Not only are the statistics lower, but the percentage of background is greater and there is more incertitude in the case of the End Caps. This is one more reason to try to carry the studies using the information from events whose electron is whole contained in the CC.

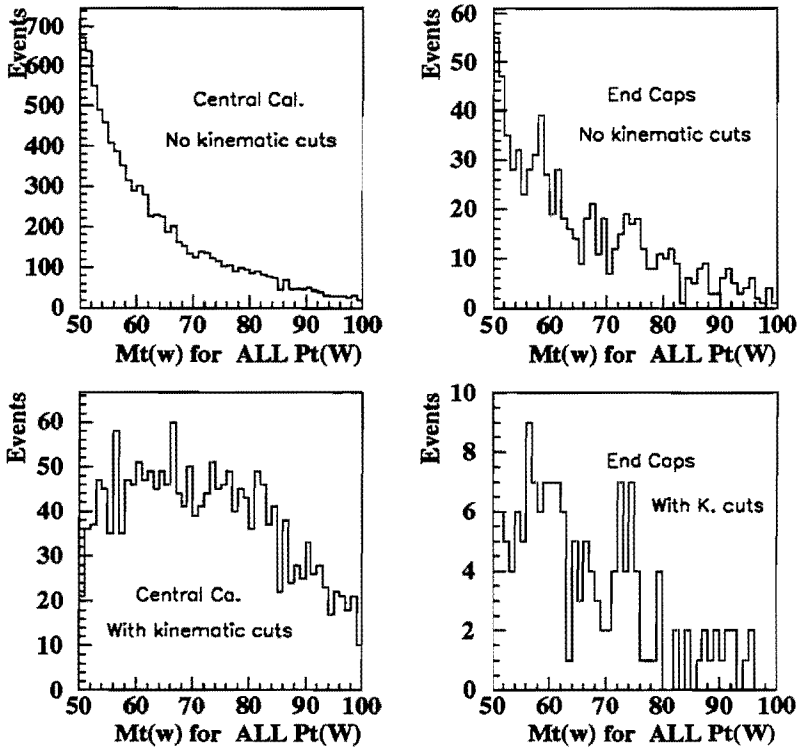

Figure 7.8: **CC and EC QCD background shapes.**

Although this method is not suitable for the purpose of this study, the overall QCD Background distribution obtained can be used as a way to compare results from other approaches.

It must be mentioned that the shortcomings of this technique rest in the lack of statistics. With sufficient statistics, it should provide a good way to obtain background shapes.

7.3.2.2 Simulating Bad events from QCD events

As part of the studies done by the DØ collaboration, a fair amount of QCD events were obtained with a special trigger. The trigger selects events with at least one jet with $P_T \geq 7$ GeV and no leptons. Some events have missing transverse momentum.

Because these are typical QCD events, and the QCD Background is primarily due to these types of events, a logical approach is to use them to mimic the QCD Background. The way to do this is to duplicate, as faithfully as possible, the process by which a QCD event is misinterpreted by the detector as a W event. As stated before, the source of *fake electrons* is a case of mislabeling a hadronic jet as an electron. Following this line of thought, it is possible to generate fake electrons simply by taking one of the jets of the QCD event and treating it as an electron. This fake electron, combined with the $\not\!\!P_T$ of the event, will result in an event with the signature of a $W \rightarrow e + \nu$ event. Unfortunately the statistics so obtained are still rather poor because there are no sufficient events with $\not\!\!P_T \geq 25$ GeV as required for the QCD Background.

The procedure developed to generate QCD Background using QCD events is as follows:

- Select the jet in the event with maximum Electro Magnetic Fraction and tag it as an electron.

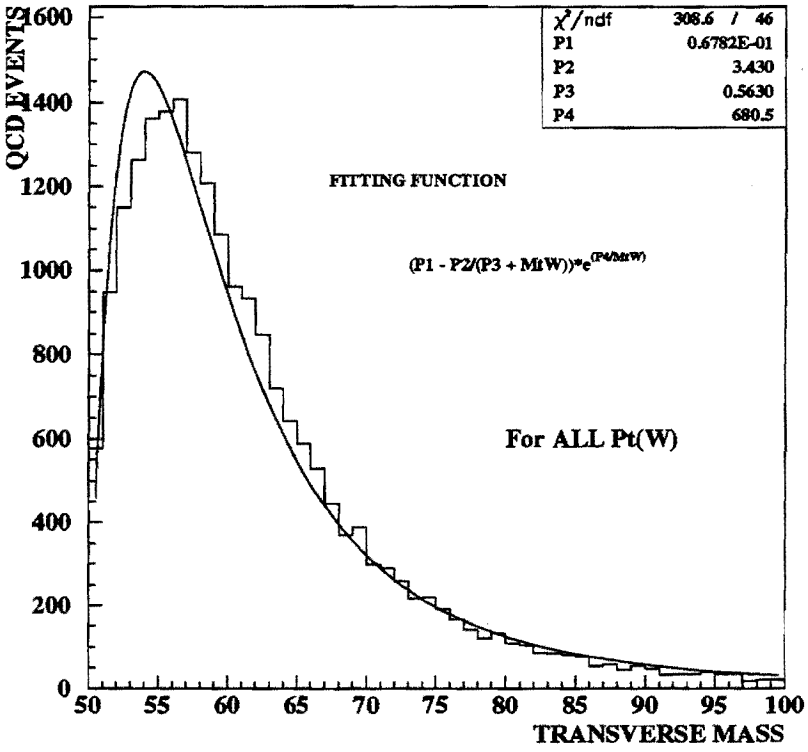

Figure 7.9: Transverse Mass Distribution of QCD Events.

All QCD events with $\not{p}_T$ treated as if they were W events. A Fitted function is overlaid.

- Calculate the energy of the selected jet as an electron. Then recalculate the $\not{P}_T$ of the event.
- Rescale all the momenta of the event so the energy of the modified event is the same as the original event.
- Treat the resulting event as a 'fake' W event. Calculate its transverse mass as well as the P_T of the fake W.
- Collect the events according to their P_T^W and fit the resulting distributions to a function F(TM_W).
- As an internal consistency check, compare the distribution for *all* P_T^W so obtained with the one obtained by the "Direct Method".

Following these steps, the 22,693 QCD events that passed the 'global' and 'kinematic' cuts imposed on the data were studied. Applying the same partitions as the ones used in the calculation of the percentage of QCD background shown on the left of table 7.4 on page 165, the four transverse mass distributions presented in 7.10 on the following page are obtained. Each of them is fitted to a function of the transverse mass. The function used is

$$BCK_{QCD}(MtW) = (P_1 - \frac{P_2}{P_3 + MtW}) * e^{\frac{P_4}{MtW}} . \qquad (7.5)$$

The function has two terms. The first term reflects the turn-on functions, while the second term describes an exponential decay. These are in agreement with what is expected from theoretical considerations. A look at the four distributions shown in figure 7.10 on the next page shows a good agreement between the actual data and the fitting functions. The same type of function

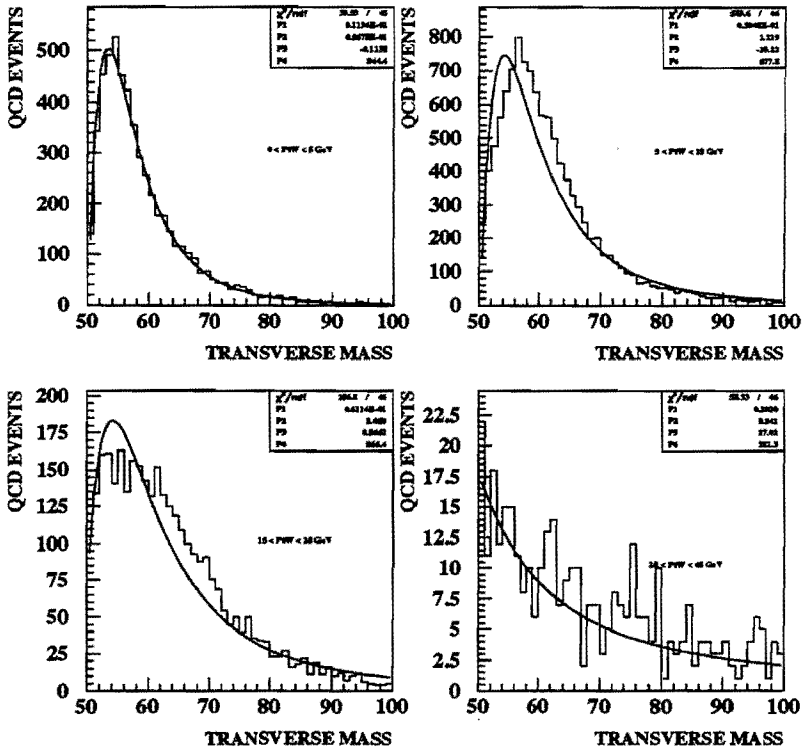

Figure 7.10: QCD Background using QCD Events.

All QCD events with $\not\!\!P_T$ treated as if they were W events. A Fitted function is overlaid.

is applied to the case where no P_t^W partitions are considered. This case is shown in figure 7.9 on page 170.

Chapter 8

Analysis

Of all that is written I love only what a man has written with his blood.

"Also Sprach Zarathustra" *F. Nietzsche*

8.1 Introduction

With all the tools at hand it is now possible to analyse the data (*all the data*) to see if it agrees with the theory. It is a good idea to enumerate some of the things we know before trying to make sense of the data. These are part of the 'prior' knowledge that is applied in the interpretation of the data. It is important to remember that there is no such thing as a probability (or plausability) in a vacuum. Any statement that starts with ' x *has a probability* p(x)' must continue with ' *given* y '. The correct expression for the probability of x is $p(x|y)$ where y consists of all the prior knowledge involved in obtaining the probability of x . In this sense, all probabilities

must be interpreted as conditional probabilities.

8.2 Determination of Priors

To assign priors to the different sets (types) of knowledge is not an arbitrary process. The determination of the prior probabilities representing the prior information* is done by logic analysis of that information. The inferences used should be (are) objective to the extent that different people holding the same prior information will assign the same relative prior probabilities to it.

Below is a non-exhaustive list of priors pertaining to the analysis at hand and their representations.

- All knowledge implied in the acceptance of the Standard Model will be represented by 'I' and will always be assumed present even if the 'I' is not written in the expressions. Its prior is 1.

- The V-A theory of weak interactions and its expansion in the SM will be represented by 'V'. Its prior is one.

- The value of α_2 for very low P_T^W is 1.0 with a prior equal to one.

$$P(\alpha_2(P_T^W) \equiv 1.|I, V, P_T^W \approx 0.) = 1. \tag{8.1}$$

  For all practical purposes, unless otherwise noted, $P_T^W < 4.3$ is considered ≈ 0 .

*Prior information does not necessarily imply '*before*' the data is obtained. To read an excellent explanation of the real meaning of '*prior information*' and '*prior probability*' we refer the reader to the work "Probability Theory: The Logic of Science" by E.T. Jaynes

■ The conditional probability of $\alpha_2(P_T^W)$ for all P_T^W greater than 4.3 GeV is considered to be unknown, both in value and in form. The only knowledge available is that $\alpha_2(P_T^W)$ is bounded. The upper bound is well described in the previous prior as 1.0. If $< \alpha_2 >$ is the predicted value of α_2 for a given P_T^W , then

$$a = 4* < \alpha_2 > - 3 ,$$

where $< \alpha_2 >$ is assigned to the lower bound of α_2 . The prior, reflecting this minimal knowledge, will be a bounded flat distribution. The prior becomes

$$P(\alpha_2(P_T^W)|I) = \begin{cases} 0 & \text{for } \alpha_2 > 1 , \\ 1/n & \text{for } 1. \geq \alpha_2 \geq a, \\ 0 & \text{for } \alpha_2 < a. \end{cases} \tag{8.2}$$

■ The QCD background shape is assumed to be independent of the P_T^W . It will be represented by a function $\mathfrak{F}(P_T^W)$. The prior for the coefficients of the function is defined by [49].

$$P(\bar{v}|I) \propto \int \cdots \int_{\overline{v_a}}^{\overline{v_b}} \exp\{-\tfrac{1}{2}(\bar{v} - \bar{\mu})^T [C]^{-1} (\bar{v} - \bar{\mu})\} d(\bar{v}) \tag{8.3}$$

where $\bar{v}$ is an n-dimensional vector representing the coefficients and $\bar{\mu}$ is the vector containing the expected values of these coefficients; i.e., the values obtained by fitting the QCD background to the $\mathfrak{F}(P_T^W)$. $\overline{v_a}$ and $\overline{v_b}$ are the lower and upper bounds of the coefficients used in the integration. [C] is the covariance matrix of the $\bar{v}'s$. The assumption

made here is that the probability function $f(v|I..)$ is Gaussian. The lower and upper limits of integration are defined as

$$limit \Rightarrow \begin{cases} \overline{v_a} = \mu - a * \sigma_v & \text{lower limit,} \\ \overline{v_b} = \mu + a * \sigma_v & \text{upper limit.} \end{cases} \tag{8.4}$$

In this expression σ_v is the error assigned by the fitting process to the coefficient v , and a is a number used to assure that the integration does not lose meaning. For this it is sufficient that the volume of the multivariated Gaussian falling outside the limits of integration be orders of magnitude smaller than the volume inside. Monte Carlo studies show that for cases where the number of variables is 5 or more a value of a = 3 is sufficient

- The prior for the percentage of QCD background ($P(p_{QCD}|I)$) will be assumed to follow a Gaussian distribution with $\widehat{p_{QCD}}$ equal to the values found in the previous chapter and shown on table 7.2 on page 161. The value of σ_p will be the error shown on the same table. The percentage value is considered to be a variable independent of the parameters describing the background. This prior is thus defined as

$$P(p_{QCD}|I) \propto \int_{pa}^{pb} e^{-\frac{1}{2}\left(\frac{p-\hat{p}}{\sigma}\right)^2} dp \tag{8.5}$$

with the limits of integration defined in a way similar to the preceding case.

- The τ background is assumed to be well defined and known. It is incorporated into the Monte Carlo generated distributions.

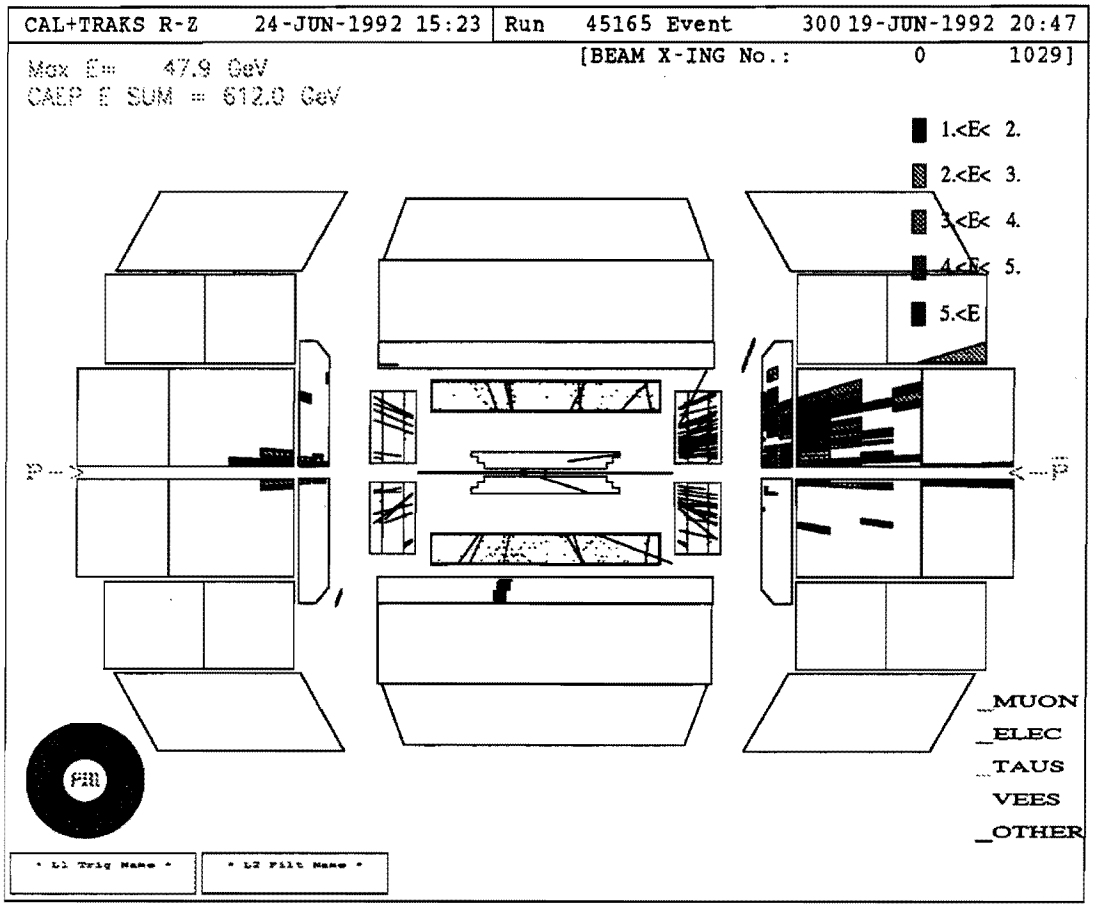

Figure 8.1: **Reconstruction of a W event in the RZ plane.**

8.3 Constraints imposed on the data

From the studies done about backgrounds, their sources and their effects on the transverse mass distribution of the W boson, it is now possible to redefine the constraints imposed on the data to be used in the final analysis.

Following are the final cuts used to define the 'data'.

- **Fiducial cuts** Considering that the knowledge of the response of the DØ detector is better for its central region, and that the estimated QCD background is worse in the End Caps, the data used is limited by geometrical boundaries. Only events whose electron is fully contained within the boundaries of the Central Calorimeter are used. The cut to select such events is

  - $|\eta_e| \leq 1.1$

- **Kinematic cuts** To the two constraints imposed over the leptons

  - $P_T^e \geq 25.\ GeV$

  - $\not{P}_T \geq 25.\ GeV$

  assure that the efficiencies for them are ≈ 1 .

  The cut

  - $P_T^W \leq 30.GeV$

  is needed because of the limitations of the Monte Carlo used to simulate the process $w \rightarrow l + l$.

  A further constraint on the data is made to diminish the effect of the backgrounds. Recalling that both backgrounds, from the τs and from QCD , strongly affect the lower end of the distribution of the transverse mass of the W, the following cuts are made

  - $55.GeV^2 \geq Mt^W \geq 90.GeV^2$.

The upper cut on the transverse mass is justified by the fact that the Mt^W distribution falls rapidly after its peak. The distribution for the QCD background, on the other hand, has a very slowly falling exponential form.

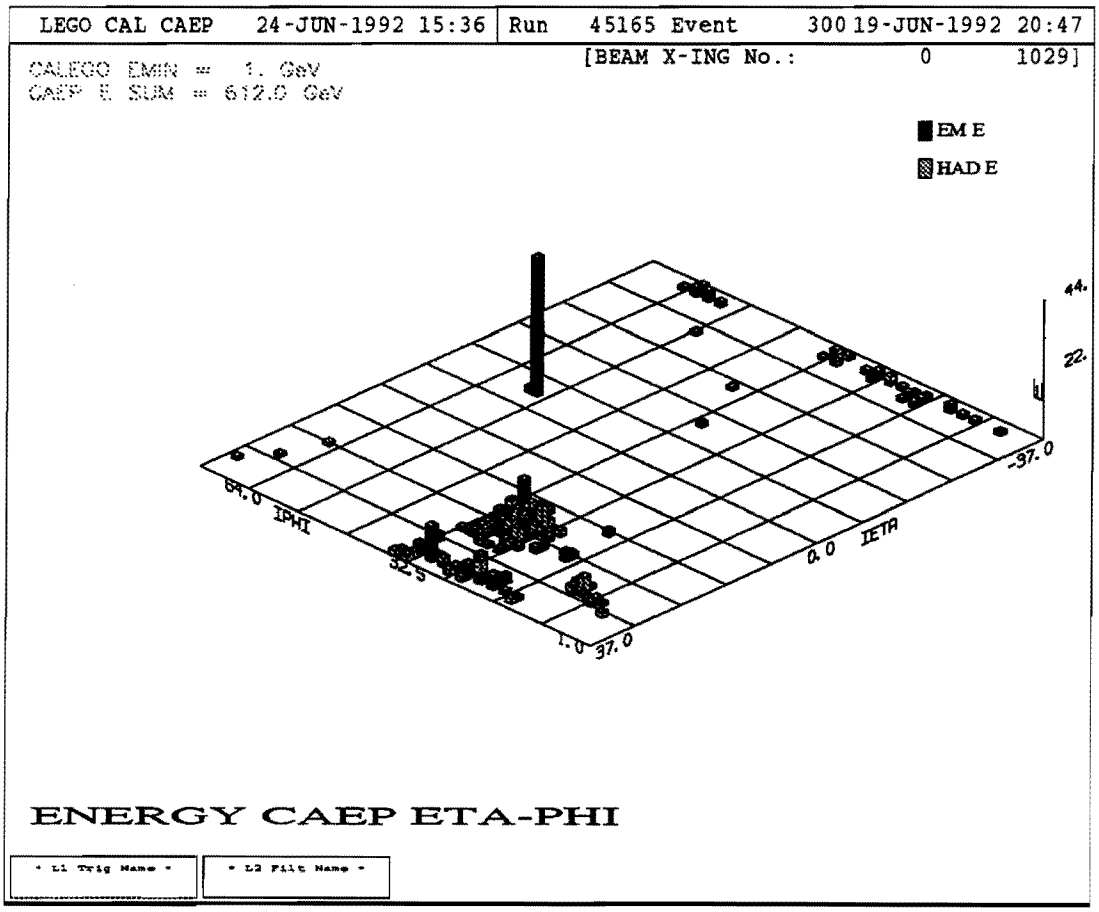

Figure 8.2: **Reconstruction of the Energies in a W event.**

- **Electron Quality cuts** Only events whose electron pass these cuts
  - $\chi^2 \leq 100$
  - $f_{iso} \leq 0.1$
  - $\sigma_{trk} \leq 5$
  - $em_{frac} \geq .9$
  - at least there is a track pointing to the vertex

  are used in the analysis.

The cuts listed above are to ensure a well-balanced compromise between the amount of signal and the amount of background present in the data used for the analysis. The idea is to maximize the $\frac{Signal}{Noise}$ ratio without unduly undermining the statistics.

Note that these cuts are more conservative than the ones presented in chapter seven. This is necessary because previously the cuts were used to assure that only possible W events were considered. Once an understanding of the effects of the backgrounds present was achieved, some decisions could be made about how to minimize their contamination of the data.

Figure 8.1 on page 177 and figure 8.2 on the preceding page are reconstructions of a typical W event. They are presented here to show how important it is to have a good set of cuts to select events. These two figures and figure 3.1 on page 79 give an idea of the difficulty encountered in trying to reconstruct an event in the presence of hadronic 'chatarra'[†].

[†]I use the Spanish expression ' chatarra ' to indicate a set of non interesting objects that could mask the presence of something valuable; ie. data. Neither ' noise ' nor '

8.4 Partitioning the Data

The work at hand can be described as :

> *"find which value of $\alpha_2(P_T^W)$ for each P_T^W has the highest posterior probability ".*

Presented this way, both the values of α_2 and P_T^W are continuous variables. To make the analysis more manageable, the analysis is redefined as:

> *"find the value of $\alpha_2(P_T^W)$, within a discrete set of values, that has the highest posterior probability for events whose P_T^W lies within well-established boundaries ".*

The first task to tackle is to define the boundaries between the different sets of P_T^W . Three main considerations drive the decision:

1. The amount of data belonging to each set should be roughly the same.

2. The first set should cover events where the P_T^W is so low that it could be assumed that $\alpha_2 \approx 1.$.

3. There should be enough events with P_T^W above a value ($10.GeV^2$) so that the difference between the predicted value of α_2 and 1. is detectable.

A good compromise is achieved by dividing the sample into four sets which

garbage ' seems to carry the information that the Spanish term does

are defined as follows:

$$P_T^W \Rightarrow \begin{cases} [\ 0.0\ ,\ 3.69) & \text{first set,} \\ [\ 3.69\ ,\ 6.2775) & \text{second set,} \\ [\ 6.2775\ ,\ 10.455) & \text{third set,} \\ [10.455\ ,\ 30.) & \text{fourth set} \end{cases} \tag{8.6}$$

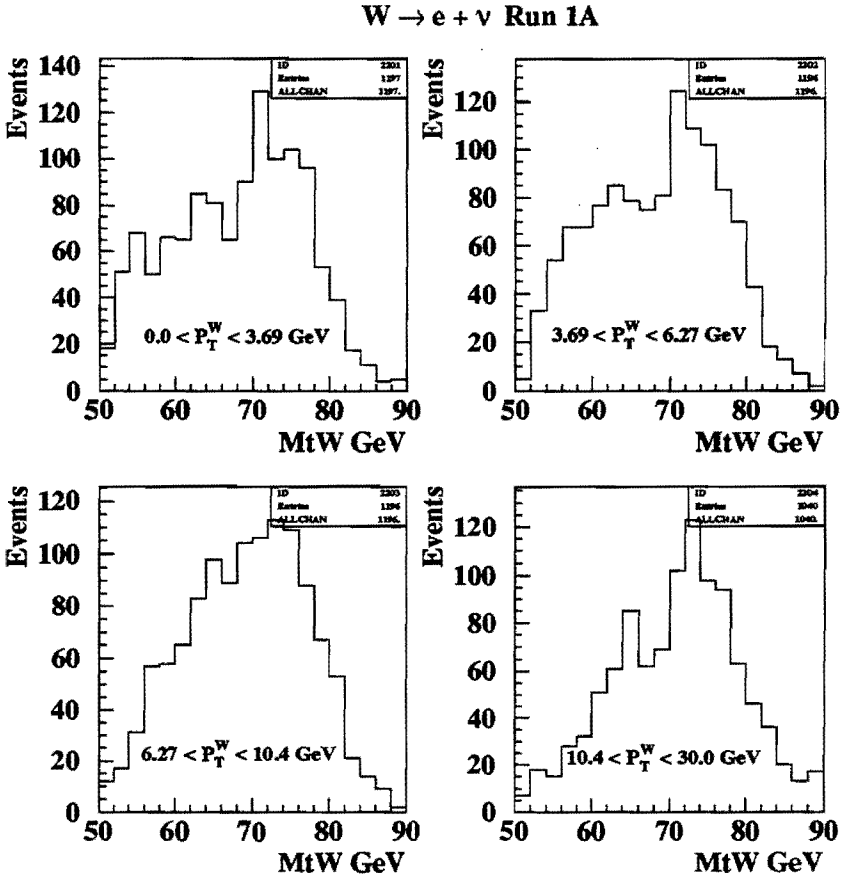

Figure 8.3: Data. Transverse mass distributions.

Figure 8.3 shows the transverse mass distributions of the data for the four

intervals of the P_T of the W.

Once the sets are established, the next step is to calculate the expected value $\hat{\alpha}_2$ for each interval. This is straight forward. Using the expression 4.4 on page 91, arrived at in chapter 5, and the Monte Carlo used to generate the W boson, a weighted average of $\hat{\alpha}_2$ for each interval can be obtained. These results, as well as other parameters of interest, are tabulated in 8.1.

P_T^W		Weighted	α_2	Prior	Number of
min	max	aver. P_T^W		function	events
0.0000	3.6900	2.331	0.997	n/a	1197
3.6900	6.2775	4.935	0.986	flat	1196
6.2775	10.4550	8.055	0.965	flat	1196
10.4550	30.0000	16.660	0.869	flat	1040

Table 8.1: **P_T^W intervals for α_2 calculations**

8.5 Analytical Expression for $p(\alpha_2|Data)$

With all the preliminary work done, the calculation of the posterior probabilities for the values of α_2 can now proceed.

The only parameter of interest is $p(\alpha_2 \,|D, I)$, while all other parameters are treated as nuisance parameters. By directly applying the rules of logical inference presented in chapter 7, it is easy to avoid the calculation of the latter. The process for each set of data as defined in the previous section is

the same. The expression

$$p(\alpha_2|D,I) \;=\; \int\cdots\int p(\alpha_2,\rho_{QCD},a0,a1,...,an,MC|D,I)d\widehat{par}\;, \tag{8.7}$$

directly provides the answer. The nuisance parameters are :

- $\star$ ρ_{QCD} is the percentage of QCD background
- $\star$ $(a0,a1,...,an)$ are the coefficients of the function

  $$\mathfrak{F}(a_o,...,a_n,MtW)$$

  describing the QCD background
- $\star$ MC is the Monte Carlo generated distribution of the transverse mass of the W where the 'Known Background'

D is the data, I represents 'all' prior knowledge, and $\widehat{par}$ is a vector representing all the nuisance parameters. To make the logical transformations that follows easier, we will represent all the nuisance parameters with 'Q' and, at the end of the logical manipulations, we will restore Q to its meaning. With this, equation 8.7 is written

$$p(\alpha_2|D,I) \;=\; \int\cdots\int p(\alpha_2,Q|D,I)dQ\;\;. \tag{8.8}$$

The integrand can be transformed using Bayes theorem as

$$p(\alpha_2,Q|D,I) \;=\; \frac{p(\alpha_2,Q|I)p(D|\alpha_2,Q,I)}{p(D|I)} \tag{8.9}$$

and, applying the product rule

$$p(\alpha_2, Q|I) \;=\; p(\alpha_2|Q, I)p(Q|I) \;\; . \tag{8.10}$$

The first term of the right hand side of this equation is the probability for α_2 given 'Q' and 'I'. But α_2 is independent of 'Q'; stated differently, 'Q' does not provide any information about α . Thus, equation 8.10 can be written

$$p(\alpha_2, Q|I) \;=\; p(\alpha_2|I)p(Q|I) \;\; . \tag{8.11}$$

Making the proper substitutions, and noticing that $p(\alpha_2|I)$ is independent of 'Q', equation 8.8 becomes

$$p(\alpha_2|D, I) \;=\; p(\alpha_2|I) \int \cdots \int p(Q|I) * \frac{p(D|\alpha_2, Q, I)}{p(D|I)} * dQ \;\; . \tag{8.12}$$

But the fraction under the integral sign is no more than the '*likelihood function*' for the data given α_2 ,Q and I. Expression 8.12 takes the form

$$p(\alpha_2|D, I) \;=\; p(\alpha_2|I) \int \cdots \int p(Q|I) * \mathcal{L}(\mathrm{D}; \alpha_2, \mathrm{Q}, \mathrm{I}) * dQ \tag{8.13}$$

and after normalization, in a more specific way,

$$p(\alpha_2|D, I)_k \;=\; \frac{p(\alpha_2|I)_k \int \cdots \int p(Q|I) * \mathcal{L}(\mathrm{D}; \alpha_2, \mathrm{Q}, \mathrm{I})_\mathrm{k} * \mathrm{dQ}}{\sum_{k=1}^{n} p(\alpha_2|I)_k \int \cdots \int p(Q|I) * \mathcal{L}(\mathrm{D}; \alpha_2, \mathrm{Q}, \mathrm{I})_\mathrm{k} * \mathrm{dQ}} \tag{8.14}$$

the condition

$$\sum_{for\ n\ \alpha s} p(\alpha_2|D, I) \;= 1.0 \tag{8.15}$$

is met. Rigorously speaking, the sum should be extended over all possible values of α_2 . However, if the choice for the lower limit of α_2 is correct,

the error introduced is negligible. The final analytical expression for the posterior probability of α_2 , given the data D and the prior I, is

$$p(\alpha_2|D,I)_k = \frac{p(\alpha_2|I)_k * \int \cdots \int p(\rho_{QCD}, a0, a1, ..., an, MC|I)...}{\sum_{k=1}^{n} p(\alpha_2|I)_k * \int \cdots \int p(\rho_{QCD}, a0, a1, ..., an, MC|I)...}$$
$$\frac{...\mathcal{L}(\mathrm{D};\alpha_2,\rho_{\mathrm{QCD}},\mathrm{a0},\mathrm{a1},...,\mathrm{an},\rho_\tau,\mathrm{MC},\mathrm{I})_\mathrm{k} * \mathrm{d}\rho_{\mathrm{QCD}},\mathrm{a0},\mathrm{a1},...,\mathrm{an},\mathrm{MC}}{...\mathcal{L}(\mathrm{D};\alpha_2,\rho_{\mathrm{QCD}},\mathrm{a0},\mathrm{a1},...,\mathrm{an},\mathrm{MC},\mathrm{I})_\mathrm{k} * \mathrm{d}\rho_{\mathrm{QCD}},\mathrm{a0},\mathrm{a1},...,\mathrm{an},\mathrm{MC}}. \quad (8.16)$$

8.6 The Likelihood Function

The previous section concluded with the analytical expression for the posterior, or conditional, probability that one particular value of α_2 will be correct given the data and all pertinent prior knowledge of the problem. The specific value being tested is an element of the finite set described in the section dealing with the priors. The effectiveness of the method seems clear. What remains to be done is to define properly the likelihood function to be used. The likelihood function is defined as [51]

$$\mathcal{L}(\mathrm{a_1},\mathrm{a_2},...,\mathrm{a_n}) = \prod_{\mathrm{i=1}}^{\mathrm{N}} \mathrm{P_i} \quad (8.17)$$

where P_i is a normalized probability function in the orthodox meaning,

$$P_i = P(x_i; a_1, a_2, ..., a_n) \quad (8.18)$$

evaluated at the observed value x_i .

Note that no specific type of 'statistics' is used in the definition. Any type of functional description of the 'probability' of observing x_i will suffice as long as it is well behaved and normalizable. Of course, the choice must be driven by logic and the conditions of the problem. After all, the likelihood

function only has meaning '*within the context of the assumed model*[150] '. The transverse mass distributions for the data, shown in figure 8.3 on page 182, clearly indicate that the number of events observed within a narrow interval of Mt^W are, in instances, very low. This precludes the application of Gaussian distributions to their contents, a better description is obtained using Poisson distributions. This choice made, the likelihood function to use is

$$\mathcal{L}(\mathrm{D}|\alpha_2, \rho_{\mathrm{QCD}}, \mathrm{a0}, \mathrm{a1}, ..., \mathrm{an}, \mathrm{I}) \;=\; \frac{\mu^{\mathrm{x_i}}}{\mathrm{x_i!}} * \mathrm{e}^{-\mu} \qquad (8.19)$$

where the variables x *and* μ are defined in function of the data, the Monte Carlo theoretical distributions and the nuisance parameters. These are:

- x_i is the number of events observed in the interval Mt^W_{i-1}, Mt^W_i . Obviously this is an integer.

- μ is the 'expected' number of events for the same interval, its value given by

$$\mu_i \;=\; MC_i \;+\; \rho_{QCD} * \mathfrak{F}(Mt^W_i) \qquad (8.20)$$

  where i defines the interval, $\mathfrak{F}(Mt^W_i)$ is the function describing the QCD background, MC is the Monte Carlo that includes the signal and the Known Background and Mt^W_i is the center value of the W's transverse mass in the interval i.

Fitting the general form of the QCD background found in the previous chapter, a polynomial of 8-order is required to obtain a good fit. Figure 8.4 on the next page shows the QDC background and its polynomial fit. The 9x9 covariant matrix, not shown, is obtained in the process of fitting the QCD data to the polynomial on P^W_T .

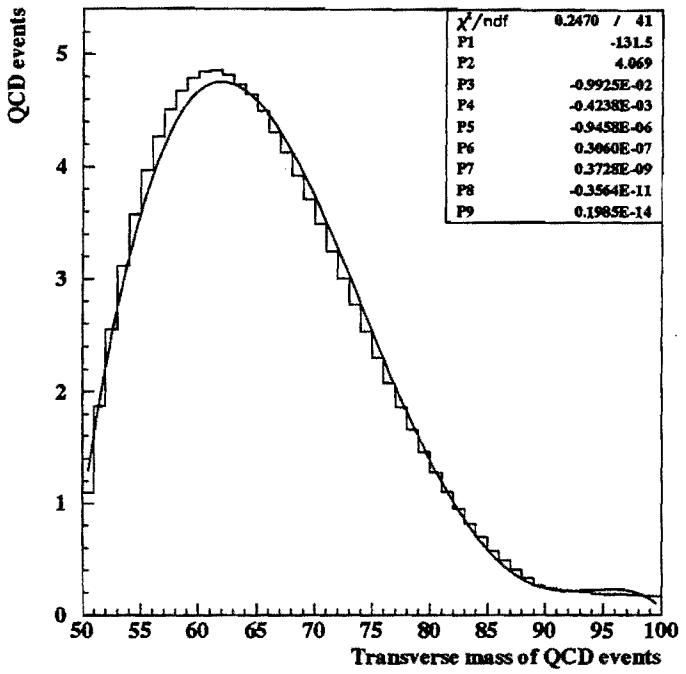

Figure 8.4: Polynomial fitting of QCD BCK.

Conversely, the expression 7.5 on page 171 could be used as such or in a simplified form as

$$BCK_{QCD}(MtW) = P_1(1 - \frac{A_2}{P_3 + MtW + Offset}) * e^{\frac{P_4}{MtW + Offset}} \tag{8.21}$$

where $A_2 = P_2/P_1$, and '*Offset*' is a new nuisance parameter introduced to allow the peak of $\mathfrak{F}(Mt_i^W)$ to move along the MtW axis.

8.7 Results

The way the problem has been treated gives, to our thinking, a higher level of accuracy to the solutions that otherwise might be obtained ignoring the prior knowledge. This is very important considering the present knowledge of the QCD background.

We proceed as follows.

- The analysis proper starts with a reevaluation of the sensitivity of the measurements to α_2 . Taking the most favorable case, two MtW distributions were generated: the first for events with $10.455 \leq P_T^W \leq 30.0\ GeV$ and α_2 value of 1., the second distribution for the same events with α_2 value of .8 . These Monte Carlo generated distributions include the proper background from τ and Z contributions. To them the QCD background is added using the expression 8.21 and the percentage value of 3.35 is reached applying

$$\%BCK_{QCD} = e^{(.69328 + .068372 * P_T^W)} ; \qquad (8.22)$$

formula obtained in the chapter dealing with backgrounds. The result is shown in figure 8.5 on the next page. The two top histograms are the ones described in the text above. The lower-left is the difference between them after normalizing both to 1. The lower-right is the percentage of change between the first and second distributions. The maximum change that one expects to find is less than $\pm 3\%$. This is far less than the values given by the theoretical sensitivity calculations made in chapter 5.

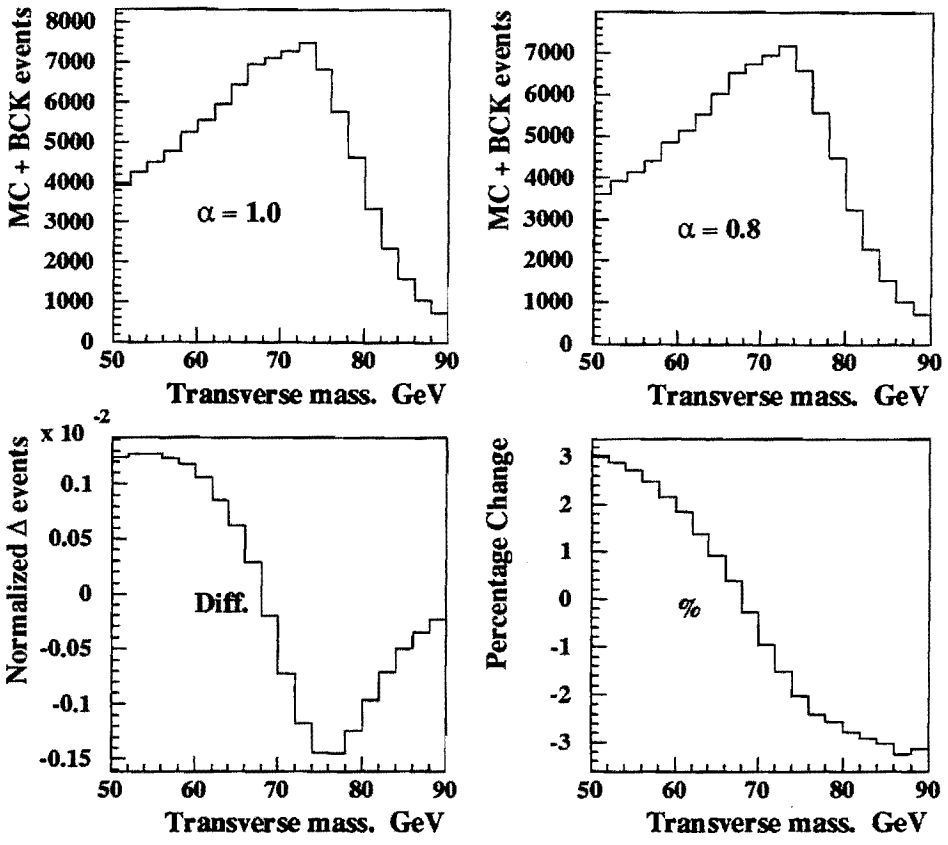

Figure 8.5: **Expected sensitivity .**

■ Generate a set of 10 MC for each P_T^W range defined in the previous table. In each P_T^W range the MC are for values of

$$\alpha_2 \rightarrow 1.00,\ 0.96,\ 0.92,\ 0.88,\ 0.84,\ 0.80,\ .76,\ 0.72,\ 0.68,\ 0.64 \quad .$$

The fact that no values above 1.0 are used reflects the prior knowledge that for the case of $\alpha_2 = 1.0$ the W is fully polarized; therefore, no value above 1.0 is possible. The minimum value used (0.64) is such

that it is reasonably far from the lower expected value of 0.86.

- Calculate the 'posterior' probability of each α_2 in each P_T^W range using expression 8.16 on page 186 and the priors defined in §§8.2. For the two most interesting cases very low P_T^W and relatively high P_T^W, the starting values for the percentage of QCD background and the Offset are

  - Low range;

    $$0.0 \leq P_T^W \leq 3.69\ GeV$$
    $$< \%\ BCK_{QCD} > = 1.2$$
    $$\sigma_{\%BCK} = 2.$$
    $$< \%\ Offset > = 0.0GeV$$
    $$\sigma_{Offset} = 0.5GeV$$

  - High range;

    $$10.455 \leq P_T^W \leq 30.0\ GeV$$
    $$< \%\ BCK_{QCD} > = 3.35$$
    $$\sigma_{\%BCK} = 3.$$
    $$< \%\ Offset > = 0.0GeV$$
    $$\sigma_{Offset} = 1.0GeV$$

- The function used to describe the QCD background (an exponential decay with a turn-on) is the same for both cases. The values of the parameters are the ones obtained earlier.

The program used to do the calculations gives, after 60,000 iterations, the results presented in table 8.2 on the next page.

		Posterior Probability for α_2									
α_2 *values*		1.00	0.96	0.92	0.88	0.84	0.80	0.76	0.72	0.68	0.64
Range											
0.0	3.69	0.170	0.160	0.134	0.110	0.110	0.099	0.073	0.066	0.045	0.030
10.455	30.0	0.110	0.122	0.137	0.138	0.120	0.111	0.098	0.087	0.080	0.070

Table 8.2: **Posterior for α_2 and two P_T^W ranges.**

Note that the sum of all posteriors, in each range, do not equal 1.0; this is due to round-off errors.

Table 8.2 makes it obvious that it is not possible to arrive at strong conclusions. To see this more clearly, the values obtained are fitted to the sum of two Gaussian distributions and the results plotted. These plots are shown in figures 8.6 on the next page and 8.7 on page 195.

To make the $F(\alpha_2 \mid I)$ a good representation of the Posterior Probability, it is necessary only to normalize it so that its integral within the allowed limits is one. Therefore,

$$f(\alpha_2 \mid DATA, I) = \frac{1}{N} F(\alpha_2 \mid I) \tag{8.23}$$

with

$$N = \int_{-\infty}^{1} F(\alpha_2 \mid I) \ . \tag{8.24}$$

Once the normalization is done, the confident intervals are easy to obtain by finding the upper limit of integration so that

$$\frac{1}{N}\int_{-\infty}^{a} F(\alpha_2 \mid I) = .050 \tag{8.25}$$

$$\frac{1}{N}\int_{-\infty}^{b} F(\alpha_2 \mid I) = .317 \tag{8.26}$$

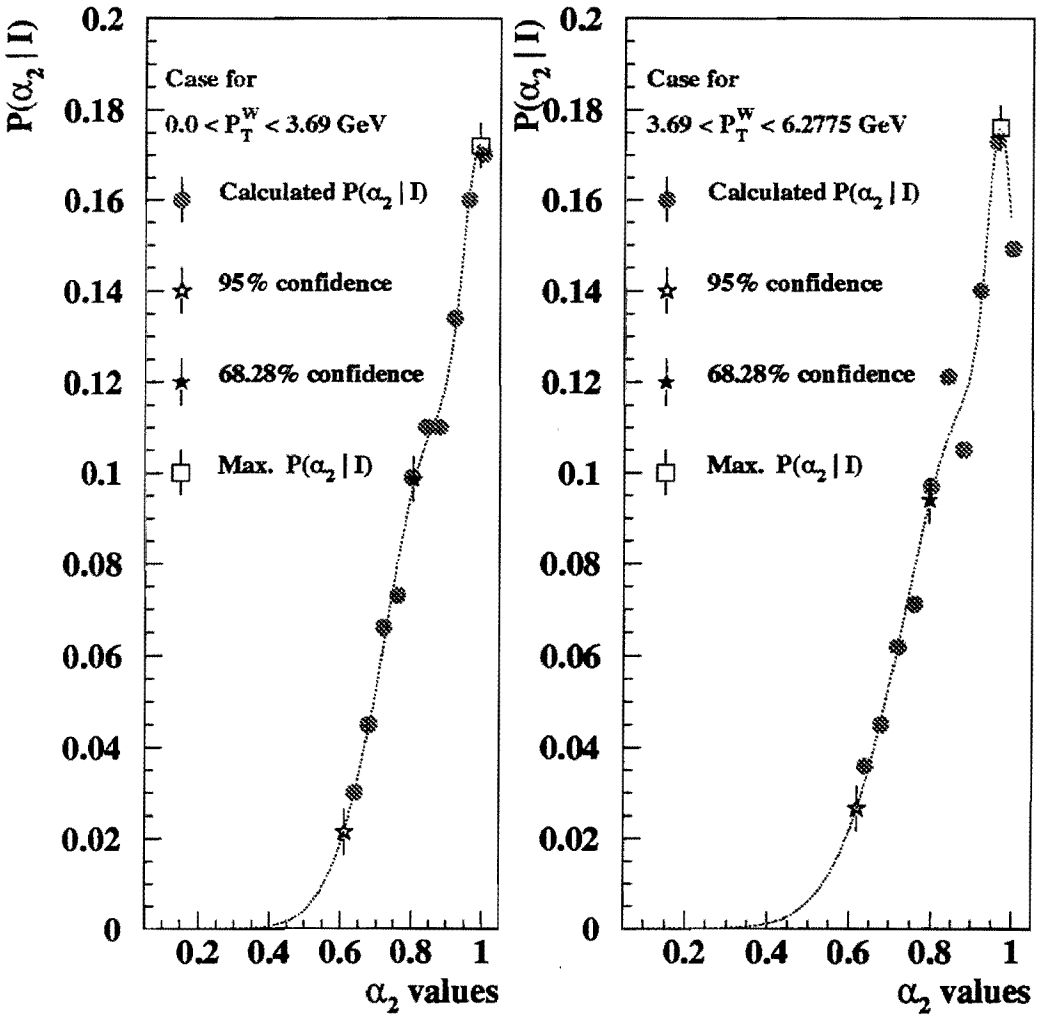

Figure 8.6: **Posterior Functions for α_2. First two P_T^W ranges.** The $F(\alpha_2 \mid I)$ values are not normalized yet.

for the 95% and 68.28% confidence of the lower limit of α_2 . Note that in this case, the upper limit of α_2 is always 1.0. The value of α_2 , with the highest posterior probability, is also easy to obtain from equation 8.23. The

values obtained after some calculations are presented in table 8.3.

		α_2 values for ...			
$P(\alpha_2 \ , \ D, I)$		68.28% c.l.	Optimal	Max.	Theo.
P_T^W Range					
0.0	3.69	0.804	0.991	1.0	.997
3.69	6.277	0.797	0.968	1.0	.986
6.277	10.455	0.779	o.964	1.0	.965
10.455	30.0	0.706	0.909	1.0	.869

Table 8.3: α_2 values of interest.

It is important to remember how the different values of α_2 are obtained to properly interpret the confidence levels quoted. Recalling expression 8.16 on page 186 it is obvious that $f(\alpha_2 \mid DATA, I)$ will be more or less sharp depending of several factors. A list of these factors and the way they contribute to the sharpness of $f(\alpha_2 \mid DATA, I)$ is presented below.

- The number of data events available enters directly through the ' likelihood function '. As more events are available the likelihood function becomes sharper. The flatness introduced by the availability of a small number of events reflects a 'statistical error' introduced in the knowledge of the value of α_2 .

- How well the percentage of QCD background is known, represented by $\sigma_{\%BCK}$, affects $f(\alpha_2 \mid DATA, I)$ through the prior $p(\%BCK|I)$ and the likelihood function. As the knowledge about it increases, the value given to $\sigma_{\%BCK}$ decreases, producing a sharper $f(\alpha_2 \mid DATA, I)$. If $\%BCK$ is perfectly, well known its prior will be a δ function. Thus

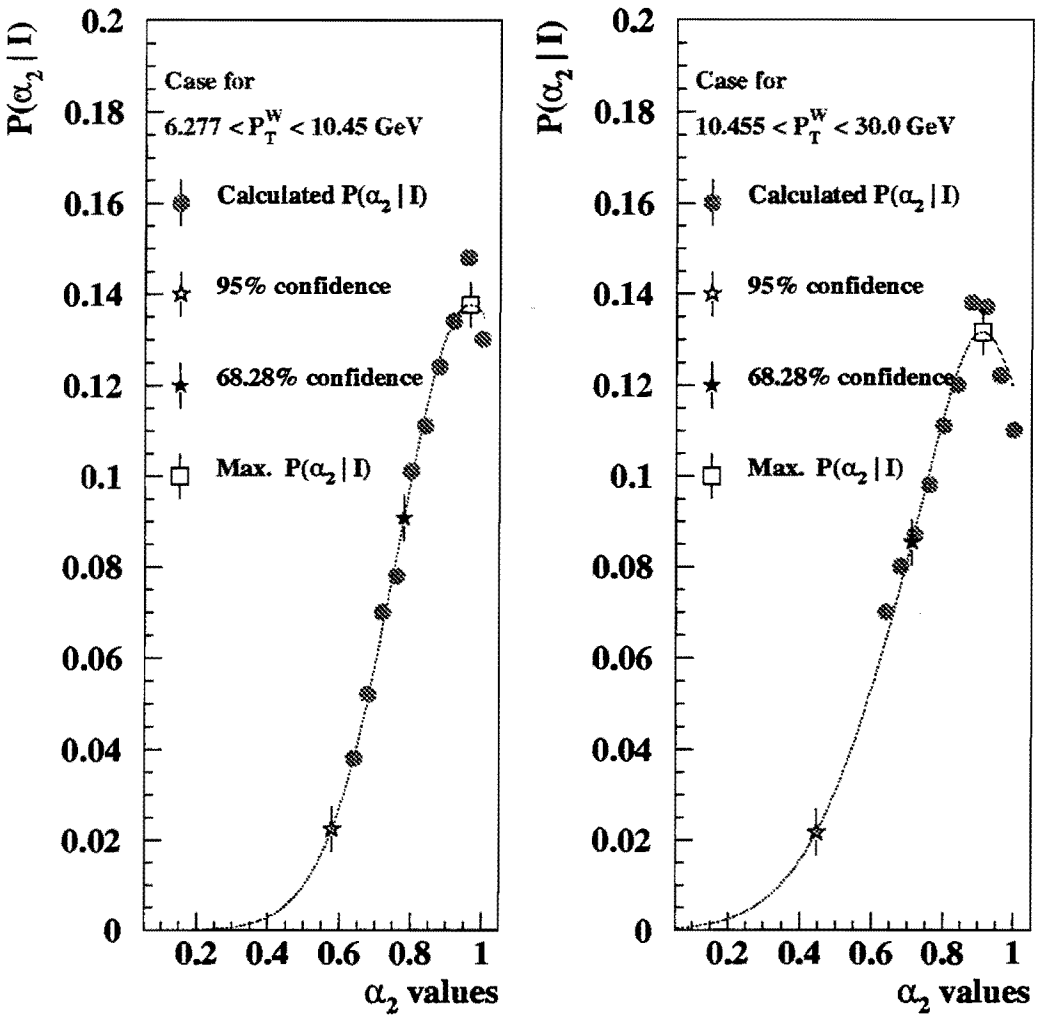

Figure 8.7: **Posterior Functions for α_2. Last two P_T^W ranges**

it will no longer be a nuisance parameter. Our lack of knowledge is a function of the procedure followed to obtain it as well as a function of the number of events used in the procedure. It follows that the flatness of $f(\alpha_2 \mid DATA, I)$ due to the lack of knowledge of this parameter

represents a statistical error as well as a systematic error. To illustrate the situation let us consider two extreme cases. If the procedure to obtain the value of the percentage of background were well defined and unique, but the number of points to obtain a fit were few everybody would agree that the errors introduced by the fitting would be ' statistical errors'. Conversely, if the amount of data available were unlimited but the procedure one among several to chose from, then the same errors will be interpreted as 'systematic errors'. When both situations are present the errors are a mixture of 'statistical' and 'systematic' errors.

- The knowledge of the shape of the QCD background is reflected by covariance matrix [C] and errors assigned to each parameter obtained in the process of fitting the transverse mass distribution of QCD events. As in the previous case, a mixture of statistical error and systematic error is present in the flatness of $f(\alpha_2 \mid DATA, I)$ created by the imperfect knowledge of these parameters.

- The 'offset' parameter was introduced because, even though the shape of the QCD background is assumed independent of P_T^W , the position of the peak is known to change with P_T^W . The contribution of the offset parameter to the flatness of $f(\alpha_2 \mid DATA, I)$ can be considered as a systematic error contribution.

From the description of the contributions of the different parameters, or more rigorously the contribution of our knowledge about them, a proper interpretation of table 8.3 results. Mainly,

"given our knowledge of the problem we can say:

- **the most probable value of α_2 for events with P_T^W between 0.0 GeV and 3.69 GeV is .991 and with a confidence level of 68.28 % (95 %) this value is between 1.0 and 0.804 (1.0 and 0.612)**

  ****

  ****

  ****

- **the most probable value of α_2 for events with P_T^W between 10.455 GeV and 30.0 GeV is .90 and with a confidence level of 68.28 % (95 %) this value is between 1.0 and 0.707 (1.0 and 0.62) . "**

Chapter 9

Conclusion

"Tell us!"
"All right," said Deep Thought. "The Answer to the Great Question..."
"Yes...!"
"Of Life, the Universe and Everything..." said Deep Thought.
"Yes...!"
"Is..." said Deep Thought, and paused.
"Yes...!"
"Is..."
"Yes...!...?"
"Forty-two",said Deep Thought, with infinite majesty and calm.

The Hitchhiker's Guide to the Galaxy
D. Adams

9.1 Conclusions

The goal of this work is to study the behavior of the angular distribution of the electron from the decay of the W boson in a specific rest-frame of the W, the Colllins-Soper frame. More specifically, the parameter α_2 from the

expression

$$\frac{d\sigma}{d(P_T^W)^2\, d\cos\theta^*} = k(1 + \alpha_1 \cos\theta^* + \alpha_2(\cos\theta^*)^2) \ ,$$

corresponding to the distribution of $\cos\theta^*$ in the Collins-Soper frame, was measured. The experimental value of α_2 was compared with the predictions made by E. Mirkes [11] who included the radiative QCD perturbations in the weak-interaction $B_{boson} \rightarrow lepton + lepton$. This experimental value was extracted for the first time using knowledge about how the radiative QCD perturbations will modify the predictions given by the Electro-Weak process only.

The work was done in a novel manner in several aspects.

⋆ The analysis was performed in the laboratory frame in an indirect way by observing how the distribution of the transverse mass of the W boson behaved. The most direct way to analyse the data is to boost the event to a frame of reference where the boson is at rest. The decision to do the analysis in the laboratory frame of reference is justified because

- ⋆⋆ working in the Collins-Soper frame introduces unwarranted errors due to the lack of knowledge about the z component of the momentum of the neutrino.
- ⋆⋆ For the same reason, events are lost.
- ⋆⋆ Our knowledge of how QCD background affects the transverse mass distribution is far better than how it affects the $\cos\theta^*$ distribution.

A detailed study of the impact of these factors in the analysis was presented in chapter 5. This is followed by Monte Carlo studies showing

that the transverse mass of the W is sufficiently sensitive to changes in the value of α_2 to allow the extraction of the value of α_2 .

⋆ Probability theory, as an inference engine, has been used throughout the analysis. This makes the analysis more robust than if solely orthodox statistical methodologies were used. Furthermore, it allows the logical inclusion of 'prior' knowledge in the analysis. To our knowledge this is the first time for such application of logical statistical inference in a thesis in the realm of high energy physics.

⋆ New ways to deal with the so called QCD background need to be explored. A method, anchored in the understanding of the behavior of the calorimeter and of the composition of jets, was developed and applied.

⋆ A new method to obtain the expected percentage of QCD background for low values of the P_T^W was developed and applied.

The results presented here constitute the first measurement of α_2 as a function of the transverse momentum of the W. As such, they show for the first time the effects of radiative QCD in the kinematics of the W decay, a weak interaction process. Based on very limited statistics, the conclusions are far from strong. Figure 9.1 shows the experimental values of α_2 compared to their theoretical predictions.

The solid curve is a polynomial fitting of the theoretical values.

The best estimate values for α_2 are shown as stars.

The error bars correspond to a confidence level of 68.28 % .

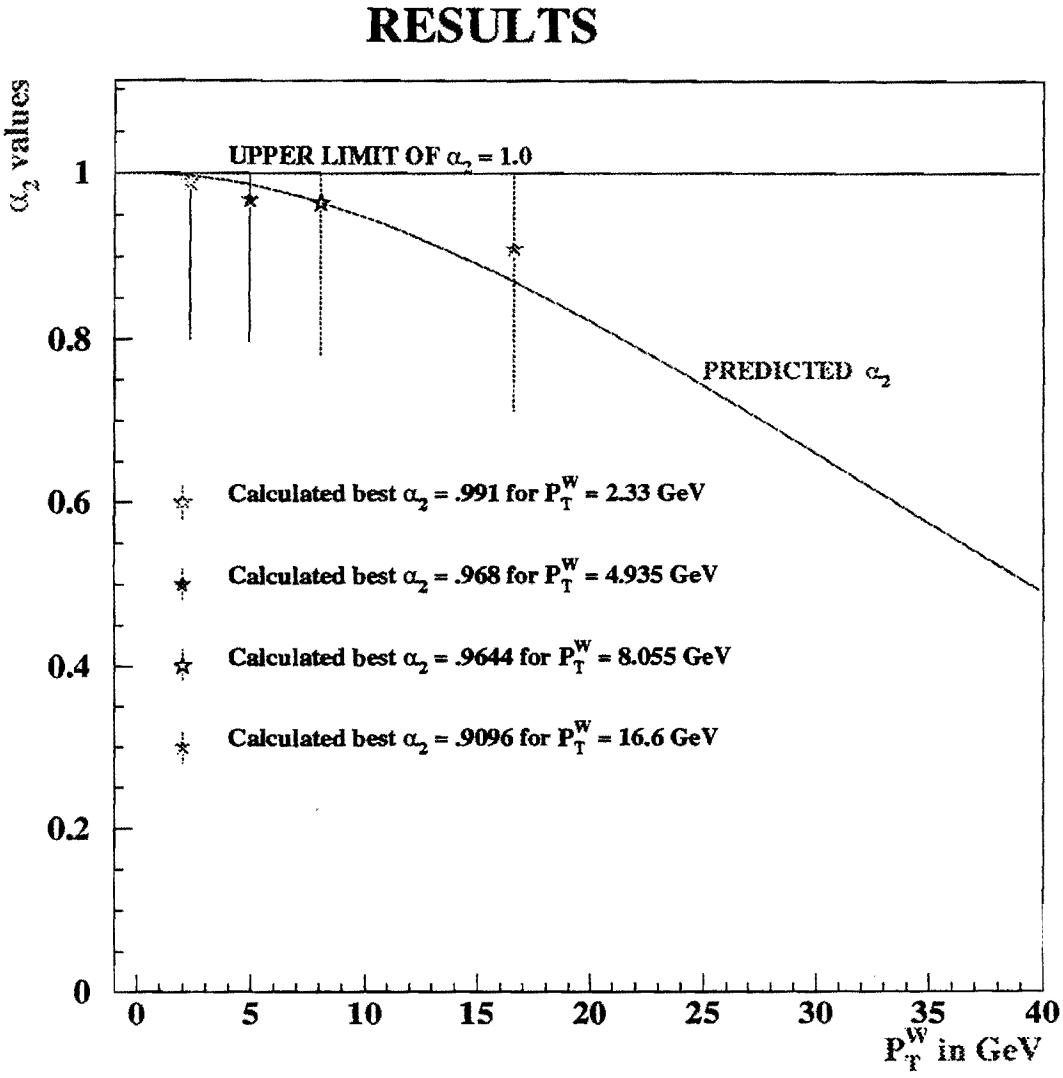

Figure 9.1: **Comparison between theoretical predictions and experimental data.**

Looking only at the central values, a good agreement appears to exist between experiment and theory. Unfortunately, when the confidence intervals are taken into account, very little more than a weak statement such as

■ ■ *The data shows behavior predicted by the theory, namely that the value of* α_2 *decrease as the* P_T^W *increases.* ■ ■

can be made.

A better summation of the results would be that the experimental values of α_2 agree, within errors, with QCD and the V-A weak interactions theory.

The methodology applied is sound, and with better statistics a good determination of the value of α_2 can be made.

9.2 Suggestions

This analysis uses the data obtained in the first run (Run 1A) of DØ where the total luminosity was $14.9 \pm 1.8\ pb^{-1}$. The luminosity achieved during the second run (Run 1B) was much higher: $80 \pm 8\ pb^{-1}$. The combined runs should have enough W events to warrant the repetition of the measurement of α_2 . Also, the number of Zs, although one order of magnitude less, are appropriate to measure α_2 from the angular distribution of e in the process $Z \rightarrow ee$.

A stronger suggestion is to repeat the analysis once the upgrade to the DØ detector is acquiring data. The ability to define the charge of the particles detected will make possible the measurement of α_1 as well. A greatly improved tracking system will allow for far more precise measurements and, thus, we could measuere β_1, β_2 as well.

■ ■ **There are good times ahead!**

Bibliography

[1] G. Arnison *et. al.*(UA1 collaboration), *Phys. Lett.***B 122**103, (1983)

[2] R. Ansari *et. al.*(UA2 collaboration), *Phys. Lett.***B 122** 476, (1983)

[3] R. Ansari *et. al.*(UA2 collaboration), *Phys. Lett.***B 129** 130, (1983)

[4] G. Arnison *et. al.*(UA1 collaboration), *Phys. Lett.***B 147**241, (1984)

[5] P. Aurenche and J. Lindfors, *Nucl. Phys.***B 185**,274, (1981)

[6] P. Aurenche and J. Lindfors, *Nucl. Phys.***B 185**,301, (1981)

[7] N. Arteaga-Romero, A. Nicolaïdis and J. Silva, *Phys. Rev. Lett.'* **52**, 172, (1984)

[8] C. Albajar *et. al.*(UA1 collaboration), *Z, Phys.* **C 4415**, (1989)

[9] R. Ansari *et. al.*(UA2 collaboration), *Phys. Lett.***B 186** 440, (1987)

[10] E. Locci, *Proc. 8th European Symp. on Nucleon-Antinucleon Interactions,* Thessaloniki, (1986)

[11] E. Mirkes, *Nuclear Physics,***B 387** 3 (1992)

[12] H. Weyl, *Space-Time-Mater,* Published in german in 1921

[13] P.A.M. Dirac, *Proc. R. Soc. London* ,**A114**243, (1927)

[14] R.P. Feyman, *Physical Review*, **76**,769, (1949)

[15] J. Schwinger, *Physical Review Letters,***8** , 214, (1949)

[16] H. Fukuda, Y. Miyamoto, S. Tomonaga, *Progress in Theoretical Physics,***4** , 121, (1949)

[17] R.L. Mills, C.N. Yang,*Phys. Rev.,***96**, 191, (1954)

[18] M. Gell-Mann, *Phys. Lett.,***8**, 214, (1964)

[19] G. Zweig, *Developments in the Quark Theory of Hadrons, Vol. I:1964-1978,* published 1980

[20] J. Goldstone,*Nuovo Cim.* ,**19**,154, (1961)

[21] P. W. Higgs, Phys. Lett. **12**, 132, (1964)

[22] need to find reference

[23] S.L. Glashow, J. Iliopoulos, L. Maiani, *Phys. Rev.* **D 2**,1285, (1970)

[24] As quoted by C. Quigg in *Gauge Theories of the Strong, Weak, and Electromagnetic Interactions, p.267*

*[25] H. Fritzsch, M. Gell-Mann, Proceedings of the XVI International Conference on High Energy Physics,*Fermilab, September 1972, p. 135

[26] J.C. Collins, D.E. Soper, *Phys. Rev.* **D 16**,2219, (1977)

[27] DØ collaboration, "The DØ Detector", FERMILAB-PUB-93/179, submited to *Nucl. Instr. and Meth.*

[28] DØ collaboration, "Design Report: The DØ Experiment at Fermilab Antiproton-Proton Collider", (unpublished, 1984)

[29] P. Franzini, Perspectives in Electroweak Interactions, Procedings of the XXth Recontre de Moriond, Les Arcs, France, p. 185 (1985)

[30] M.A. Abolins, Proceedings of the First Aspen Winter Physics Conference, Annals of the New York Academy of Sciences, **461**,p.63 (1986)

[31] P.D. Grannis, Results and Perspectives in Particle Physics, Proceedings of Les Rencontres de Physique de la Valle d'Aoste, La Thuile, Italy, p. 253 (1987)

[32] R. Madaras, Proceedings of the Division of Particles and Fields Conference, Batavia,Il.,(Nov. 1992)

[33] A.R. Clark *et al.*,Nucl. Instr. and Methods in Phys. Res. **A315**, 193, (1992)

[34] W.W.M. Allison and P.R.S. Wright,"The physics of charged particle identification...", *Experimental Techniques in High Energy Physics; Frontiers in Physics,* 371 (1987)

[35] D. Pizzuto, *DØ Central Tracking Chamber Performance Studies,*Ph.D. thesis, SUNY at Stony Brook, (1991) (unpublished)

[36] S. Rajagopalan, *The dE/dx capabilities of the DØ Tracking System,* Ph.D.thesis, Northwestern University, (1992) (unpublished)

[37] J. Bantly, *The DØ detector Forward Drift Chamber Performance and Physics Capability in the 1990 FNAL Testbeam Run, (1992) (unpublished)*

[38] W. Guryn, Procedings of the Second International Conf. on Calorimetry in High Energy Physics, Capri, Italy, Oct. 14-18 1991

[39] M.A. Abolins, et al., IEEE Transactions on Nuclear Science **V 36**, 384, (1989)

[40] M. Settles and J. Linnemann, "P_t and Vertex Uncertainties", *DØ Note* **632.** Feb. 1988 (unpublished)

[41] N. Hadley, DØ Note **904** , (1989) (unpublished)

[42] M. Paterno, " A Montecarlo Study of the DØ Calorimeter Missing E_T Resolution',*DØ Note* **1374** , (1992) (unpublished)

[43] M. Paterno, " A Study of the DØ Calorimeter $\not\!\!E_T$ Resolution Using Low E_T Jet Triggers ',*DØ Note* **1782** ,(1993) (unpublished)

[44] R. Engelmann *et al*, Nucl. Instr. and Methods **A216** ,45 (1983).

[45] M. Narain (for the DØ collaboration),*Electron Identification in the DØ detector* , FERMILAB-Conf-93/054-E, (1993) (unpublished).

[46] S. Chopra, U. Heintz and M. Narain,*Comparison of Electron ID efficiencies in Run 1A and Run 1b.*DØ Note **2351,** (1994) (unpublished)

[47] M. Demarteau, J.Sculli and K. Streets, *Measurement of the W-mass* DØ note **2929, (1996)**

[48] **I. Adam,** *Underlying event correction to the electron energy in $W \rightarrow e\nu$ decays at DØ,* DØ note **XXXX.**

[49] *Review of Particle Properties. Phys. Rev.* **D501272** (1994)

[50] E.T. Jaynes, *Probability Theory: The Logic of Science,* WWW, fragmentary edition of July 1995

[51] P.R. Bevington, D.K. Robinson, *Data Reduction and Error Analysis for The Physical Sciencies,* McGraw-Hill, (1992)